Light Delivery in Turbid Media

by

Thomas Haylock

A thesis
presented to the University of Waterloo
in fulfillment of the
thesis requirement for the degree of
Master of Applied Science
in
Systems Design Engineering

Waterloo, Ontario, Canada, 2011

I hereby declare that I am the sole author of this thesis. This is a true copy of the thesis, including any required final revisions, as accepted by my examiners.

I understand that my thesis may be made electronically available to the public.

Abstract

Light delivery and sample handling systems are essential for any high performance imaging application. The custom design for two such devices with medical imaging applications are presented. The first device, a galvanometer-stage combination, is for general use optical coherence tomography and can be configured to scan over a large range of sample sizes and types. The second device, constructed in parallel, a rotation-linear stage combination, has been carefully designed for a specific imaging task: assessing tumour margins. The design of the two devices is driven by operational requirements and although requirements vary greatly from application to application, there are several common parameters that must be considered for every system. In this thesis, parameters like total scan time, scan resolution, sampling rate, and sample type flexibility are analysed and are some of the primary factors that influence the viability of a system for further development. This work's contribution to medical imaging research is the design of two light delivery systems and an analysis process that can be applied to future iterations of scan systems.

The devices are shown to be flexible enough for use in test-bed systems, while providing the necessary functionality to meet the needs of medical histology and pathology. Controlling the light delivery and sample positioning of an imaging device adds important functionality to a scan system and is not a trivial task when high spatial-resolution scan spacing is required. The careful design of an imaging system to meet the unique requirements of the application enables better information and better resulting decision making. Advanced imagery provides new insights and perspectives to everyday scenes. It is these new perspectives that allow for re-evaluation and examination of problems with a fresh eye.

Acknowledgements

Medical imaging systems are a multi-person effort and I have worked with many people on the various projects that sit on our optics table. First, I would like to thank my supervisor, Arsen Hajian, who has been the driving force behind my work. He brought together a team of people to create wondrous devices and continues to spend as much time as needed, even late in the evening, to offer wisdom and advice to me.

I wish to thank Andrew Cenko and Jeff Meade for their tireless efforts developing many of the systems that I have interfaced with over the past two years and for answering my endless questions along the way. My degree has also been filled with fruitful discussions of projects and coursework with Farnoud Kazemzadeh, Lev Chifman, and Peter Christensen.

The exciting projects you will soon read about would not have been possible without the help and input of our partner organisations, Tornado Medical Systems, Arjae Spectral Enterprises, and the Thunder Bay Regional Research Institute. In addition, I wish to thank Kevin Schill of Electromate Industrial Sales for his discussions about optimising our hardware.

Finally I wish to recognise my family for their support over so many years. This Masters thesis is the culmination of two years of learning new fields, turning lab-mates into friends, and becoming the Waterloo Engineer I am today.

Dedication

This thesis is dedicated to my parents and family. They have been a part of the many milestones I have already faced and will always be there for the milestones to come. This is dedicated to those individuals in my life that push me to succeed and keep a smile on my face.

Table of Contents

List of Tables

List of Figures

Chapter 1

Introduction

Remotely-obtained images provide new insight and perspective to everyday scenes. It is these new perspectives that allow for common objects to be re-evaluated and examined with a fresh eye. When better information is available for decision making, more responsible reactions are possible. Important questions like, "is the product defect free?", or, "has the tumour been removed?", can be answered when an imaging system is carefully designed to incorporate the unique requirements of the application. This careful design process is important in any imaging market: biomedical, defence, remote sensing, or quality control, for example.

1.1 Problem area

Controlling the light delivery and sample positioning of an imaging device adds important functionality to a scan system. By moving a light beam across a target, multiple dimensions of data are obtainable and form images covering larger areas. Positioning the light beam on a target becomes a non-trivial challenge when the size of the features is small or fine spacing between scan samples is desired. Whether the target is hundreds of km away, as in satellite remote sensing, or tens of cm away, as in medical imaging, the target's features and configuration must drive the design of the positioning system.

In all remote imaging applications there are penalties associated with capturing distorted or incorrect imagery. The penalties are often computational and lead to increases in image reconstruction time and may even require rescanning a location. If the sampling rate and resolution are not properly tuned, abnormal features may be missed and consequences could be life threatening.

This thesis presents light delivery devices suitable for high performance medical imaging applications. The first device, a galvanometer-stage combination is for general use optical coherence tomography (OCT) and can be configured to scan over a large range of sample sizes and types. The second device, a rotation-linear stage combination, has been carefully designed for a specific imaging application: assessing tumour margins. The two forthcoming devices show that light delivery and sample handling requirements vary greatly from application to application, but there are several key parameters that must be considered for every system. Parameters like total scan time, scan resolution, sampling rate, and sample type flexibility are all driven by the design of the light delivery system and are some of the primary factors that influence commercial viability of the imaging system. Completing a scan as quickly as possible while retaining precise position control is a key goal for all application areas. More efficient scan routines improve system throughput, allowing the option for greater image duplication, additional collection locations, the scanning of additional samples, and better imaging of moving subjects. Although there are no patentable devices described in the coming pages, the design and optimisation processes described, as well as the procedures for evaluating component capabilities, are worthwhile.

1.2 Applications areas

The components for scan systems are widely used in imaging, material processing, and industrial manufacturing. The market is large enough to support the existence of a wide variety of components and the distribution of many manufacturers. Galvanometers are moving mirrors that can be used to manipulate the direction of light travel. They are used in laser marking, material processing, drug development research, fibre optic telecommunications switching, and biomedical imaging. Linear and rotational stages find use in many of the same applications as galvanometers, but are also prevalent in industrial manufacturing. Stages can be fabricated to a large variety of specifications and are suitable for nearly any application requiring the movement of materials. Scan systems synchronising galvanometers, stages, and other electronic sensors are found in laser marking, quality assurance, remote sensing, and medical imaging applications.

1.3 Medical imaging

Medical imaging aims to determine a patient's well-being, evaluate anatomy, or to explore spatial relationships that yield insight into health. Before patients can be treated, diagnosis

must be made. An increasingly important element of diagnosis is imaging. The pursuit of improved light delivery and sample handling systems is a worthy area of research because it has a major affect on the nature of output imagery and on the throughput of an imaging system. Without a scan system, images would be limited to whatever input the sensor can receive from a single location. Currently, there are long lead times for medical image acquisition and this leads to patient stress and risk that disease may progress further [19]. The light delivery system has a real effect on the pace of imaging and when optimised, can help reduce the total scan time and time between scans.

Here, optical imaging modalities are examined, but medical imaging is not limited to only the optical regime. Magnetic resonance imaging (MRI) and ultrasound imaging are examples of technology that enable patient examination without using optical wavelength radiation. OCT is an imaging modality that first made an appearance in the early 1990's [18] and has since has matured through several generations of development. The modern spectral domain OCT systems (SD-OCT) capture an entire depth scan in one sensor integration by combining a Michelson interferometer with a spectrometer. OCT has μm resolution capabilities and is bounded by confocal microscopy and ultrasound imaging in terms of resolution [13]. However, OCT has better depth penetration than confocal microscopy and so finds application in areas where tissue layers and histology are important. The technology has found a foothold in ophthalmology because it can visualise retinal layers and can be used in-vivo with no tissue damage. In fact, OCT has matured to the point where clinical use is occurring and the medical profession is benefitting from improved diagnosis [10].

A particular application of OCT is the assessment of tumour margins. Procedures like breast conserving surgery (BCS) have defined the successful removal of a tumour as a tumour excision with some thickness of healthy tissue on all surfaces of the excised cancerous tissue. The depth capabilities and possibility for real time image visualisation make OCT a candidate for intra-operative use in assessing margin thickness. The high resolution capabilities of OCT may reduce the necessary thickness of margins over time and reduce the amount of tissue that needs to be removed. The ultimate factor in the patient's cosmetic appearance is the amount of tissue excised [16]. Previously, full mastectomy was the preferred treatment, but BCS with radiation therapy has shown to result in survival rates as high as mastectomy. In addition, BCS provides better patient acceptance since the overall cosmetic change is reduced [29]. A key requirement yet to be overcome by potential intra-operative solutions is limited scan coverage; a prime requirement of an imaging system's light delivery and sample handling components and one that is met here.

1.4 Outline

This thesis is organised in four further chapters. Chapter 2 presents background information that may help to orient readers less familiar with the gamut of fields involved in light delivery, i.e., electronics, control systems, optics, and imaging. Chapter 3 presents a light delivery system that supports a generic test-bed OCT system, while Chapter 4 presents a particular application of OCT, margin assessment of excised tumours. A system for manipulating large samples is described and is necessary in order to perform full margin assessment. The optical, electronic, and control system analysis are performed for the test-bed OCT system and for margin assessment system in Chapters 3 and 4 respectively. Conclusions are presented in Chapter 5. As medical imaging becomes more pervasive in society, it is important to study how the requirements of the particular application drive component selection and integration.

Chapter 2

Background

Light delivery and sample handling systems include optics, electronics, and mechanical components and subsystems. Each element must work closely with the others to obtain the high accuracy required by such systems. The optics must remain stable, the electronics must be synchronised, and the mechanical components must be machined with precision. It is only when all elements are functioning together that light can be manipulated with the accuracy required for high resolution medical imaging. Good engineering design and analysis leads to effective medical imaging systems that will improve diagnosis. Improved diagnosis will lead to more appropriate treatments and increased quality of life.

2.1 Light propagation

Turbid media is any diffuse material like tissue or the atmosphere. It exhibits scattering and absorption of light as photons propagate through. Light may reflect from, refract through, absorb into, or scatter amongst the media particles, as illustrated in Figure 2.1. The optical axis is an imaginary line drawn through an optical system. Generally, angles used to describe light propagation are measured between the light ray and the optical axis.

2.1.1 Reflection

There are two sites of reflection as light hits a scan sample: at the sample surface, and at features, as illustrated in Figure 2.1, (A). Surface reflection is modelled as specular

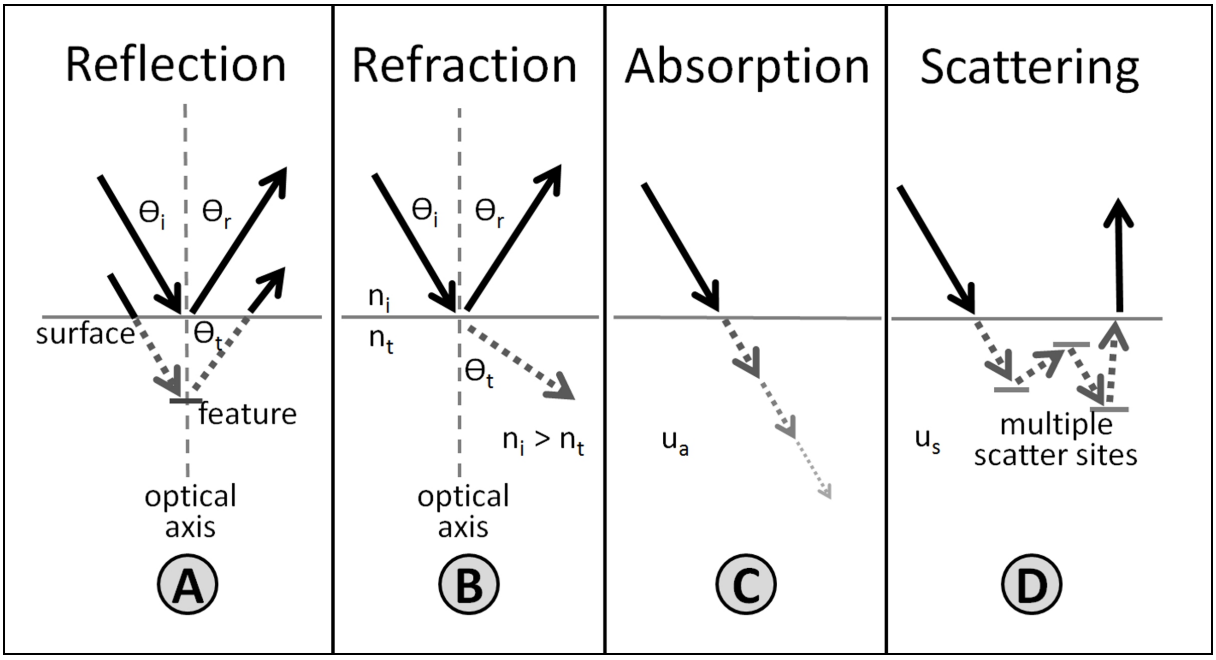

Figure 2.1: Light reflects, refracts, absorbs, and scatters in tissue.

reflection where a particular amount of the incident beam is reflected at the same angle as the incident beam. Reflection at a feature of interest is generally simulated as a Fresnel effect since a scan feature is generated by a mismatch of indices of refraction. In Fresnel reflection, a portion of light is reflected and a portion is transmitted through the medium.

2.1.2 Refraction

If two materials with different indices of refraction are joined, a light beam will refract as it moves from the first to the second material, as illustrated in Figure 2.1, (B). It is this index mismatch between the top layer and the bottom layer of a sample that causes refraction to occur. In cases where the top layer has a higher index of refraction than the bottom layer, refraction effects bend the transmission beam away from the optical axis and if the bottom layer has a higher index than the top layer, the light is bent towards the optical axis. Light refracts according to Snell's Law [24],

$$n_1 sin\theta_1 = n_2 sin\theta_2 \tag{2.1}$$

where n_1 and n_2 are the indices of refraction of the two materials, θ_1 is the angle of incidence, and θ_2 is angle of the refracted beam. If the angle of incidence is larger than a critical angle, the transmitted beam is bent so much that it aligns with the interface between the layers, i.e., the transmission angle is 90 ° from the normal. Above this critical angle, all light is internally reflected, rather than transmitted to the new medium.

2.1.3 Absorption

As a packet of photons travels through a medium, some of the photons are absorbed by the medium itself, as illustrated in Figure 2.1, (C). Light intensity is decreased during each layer interaction and the number of photons in a light packet decreases accordingly. A coefficient of absorption, u_a, is often provided for synthetic samples and can help to predict the intensity of light that will return through the system. The u_a value is also dependent on which wavelengths of light are used. For example, melanin and haemoglobin in tissue are absorptive to the near-infrared frequencies used in OCT [13]. The amount of light absorbed tends to be much smaller than the amount of light that is scattered.

2.1.4 Scattering

Scattering is an effect that causes photons to deviate from a straight line path, as illustrated in Figure 2.1. In similar fashion to absorption, scattering is modelled by a coefficient, u_s. After the effects of absorption, remaining photons in a packet of light are subject to scattering. It is important to note that the scattering coefficient is one to two orders of magnitude larger than the absorption coefficient for optical frequencies in tissue.

If the result of scattering was solely a decrease in the packet weight, this would be the end of the discussion. However, after each interaction, scattering changes the propagation direction of the remaining photons. Backscattering occurs when the scatter event changes the travel direction of the photon and the photon reverses back towards the light source. Multiple scattering is a situation where the light packet is exposed to more than one scattering event and the propagation direction changes multiple times. Multiple scattering is a more realistic representation of light interaction within turbid media, but is not well understood. Resolution and contrast are reduced in the presence of multiple scattering and with higher instance of multiple scattering, imaging depth decreases [41].

Often, the absorption and scattering coefficients are combined into one coefficient, μ_t with units cm^{-1}. The intensity of light is attenuated by μ_t according to Beer's Law [11],

$$I = I_0 exp(-\mu_t d) \tag{2.2}$$

where I is the final intensity, I_0 is the initial light intensity, and d is the distance the light has propagated.

2.1.5 Noise sources

There are two primary phenomena present in broadband, low coherence imaging that decrease imaging efficiency. Photon noise is random shot noise that results in intensity fluctuations. Photon noise could be stray light from some other source, or a piece of dust entering the field of view. The effects of photon noise are transient and occur at a single point in time. As such, a time averaged approach where multiple images are captured of the same location and averaged reduces this noise. The more images that are collected, the lower noise is expected to be [20]. Photon noise can be described using Poisson statistics and the signal to noise ratio is proportional to $\sqrt{n}$, where n is the number of photon events.

Speckle is a property of light that has to do with the microscopic nature of the light interacting with the surface of a material. It is not time dependent and will not be removed via multiple images of the same location. Speckle is manifested in a field of increasing and decreasing surface intensity and distorts the resulting feature information.

2.1.6 Phantoms

A phantom is a scanning sample used because it has some similarity to the expected target to be scanned. Phantoms are used in early stage development of an imaging system prior to clinical trials. A phantom has a known scattering coefficient, absorption coefficient, and structures. The known structures are compared against results to confirm that the imaging system is providing correct results. Depending on the complexity required, there are several options for OCT phantoms. Everyday objects provide good starting points, e.g., an onion is a good choice since it has repeated, known structure. Phantoms with characterised u_s and u_a values should be used during later stages to evaluate the efficacy of the light delivery system.

2.1.7 Full Width at Half Maximum

Full width at half maximum (FWHM) is a measure of the width of a signal. A Gaussian shaped signal theoretically has a long tail that goes on forever. Practically, there is a threshold where beyond which, the intensity is low enough to have minimal effect and it

can be ignored. In 2D images of a Gaussian optical spot, the FWHM is calculated by first vertically binning the pixels. Once the maximum is found from that line of pixels, a threshold is set at half that maximum intensity and the width is calculated between the rising and falling edges, as illustrated in Figure 2.2.

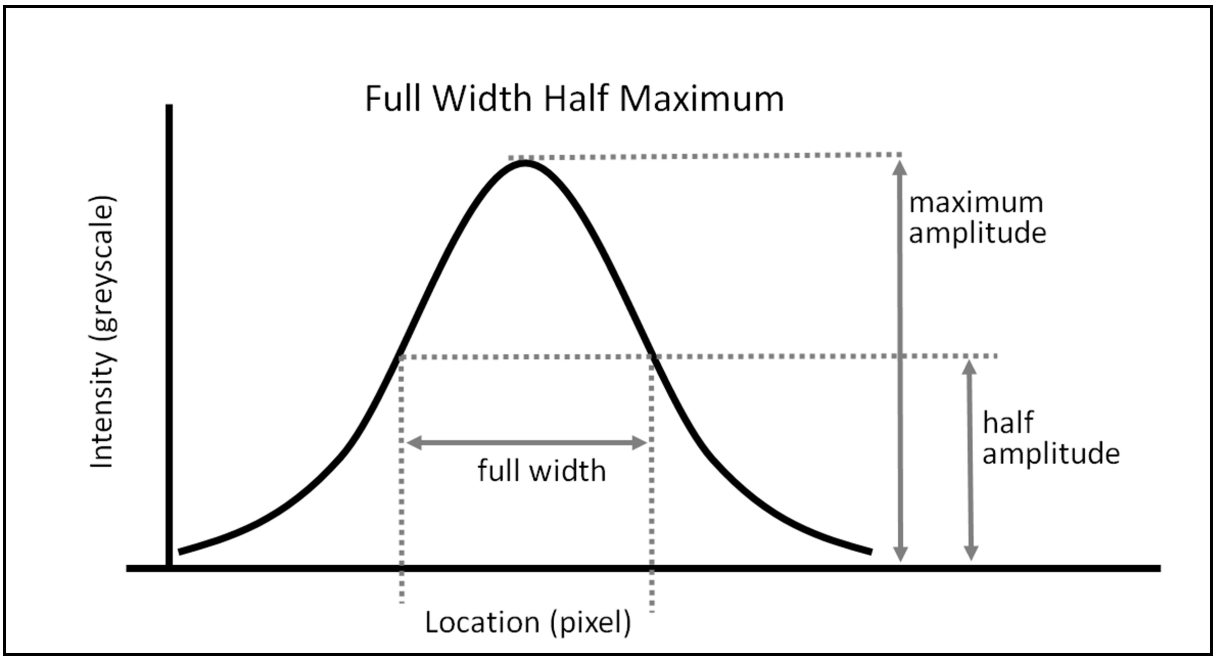

Figure 2.2: The full width at half maximum is calculated as a measure of the broadness of a signal.

2.1.8 Spatial resolution

If the incoming beam is focused to the smallest spot possible and there are no other limiting aberrations, a diffraction limited system is present. Diffraction limited systems are limited by the inherent characteristics of light and not by the configuration of the electro-mechanics that control beam positioning. A diffraction-limited spot-size is the diameter of the central Airy disc of the diffraction pattern generated by light focusing through a circular lens. The spot-size is calculated,

$$d = 2.44\lambda F \tag{2.3}$$

where d is the diameter of the spot, λ is the centre wavelength of the broadband source, and the F is the f-number (ratio of the focal length to beam diameter). The diffraction pattern created by light focusing through a circular lens is called the Airy pattern and is a series of concentric rings. On profile, this is a sinc function. The spot size in equation (2.3) is the width of the first dark ring in the Airy pattern. The Raleigh Criterion is closely related to this and is a measure of how well spots and therefore, imaged features, may be differentiated. The Raleigh Criterion states that the smallest distance between two spots that can be differentiated is,

$$\Delta L = 1.22\lambda F \tag{2.4}$$

where ΔL is the spatial resolution, λ is the centre wavelength of the broadband source, and the F is the f-number. It should be noted that the Rayleigh Criterion is an arbitrary definition and a general rule of thumb. It states that it is possible to resolve two features when the centre of an optical spot's Airy disc overlaps another spot's first dark ring in its diffraction pattern [24].

Spatial resolution is further complicated when the incident beam position is manipulated and the sampling rate comes into play. When the optics produce a diffraction limited spot, but the distance between samples is larger than the Rayleigh Criterion, the sampling distance is then the determining factor in the overall spatial resolution of the system.

If there are too few sampled locations (under-sampling) for a feature of interest, pixelation occurs and the feature will not be clear. Oversampling occurs if there are more samples than necessary and performance will be inefficient since it will take longer than necessary to complete scans. The Sampling Theorem (or, Nyquist-Shannon Sampling Theorem) states that a continuous signal can be accurately reproduced if the frequency components of the signal are less than half that of the sampling rate [35]. In imaging terms, this refers to the size of features that can be imaged correctly. For Nyquist-rate imaging, the smallest movements necessary are the half the Rayleigh Criterion. Using movements smaller than half the Rayleigh Criterion give negligible resolution gains.

2.1.9 Depth of focus

Depth of focus is the area above and below the focal plane over which it can be said the beam waist is near enough to the diffraction limited size that ideal imaging can be performed. The beam does not reach an infinitely small spot, but rather is limited to the diffraction spot size, as illustrated in figure 2.3. Above the focal plane, the beam is still converging, while after the focal plane, the beam is diverging. The depth of focus (DOF)

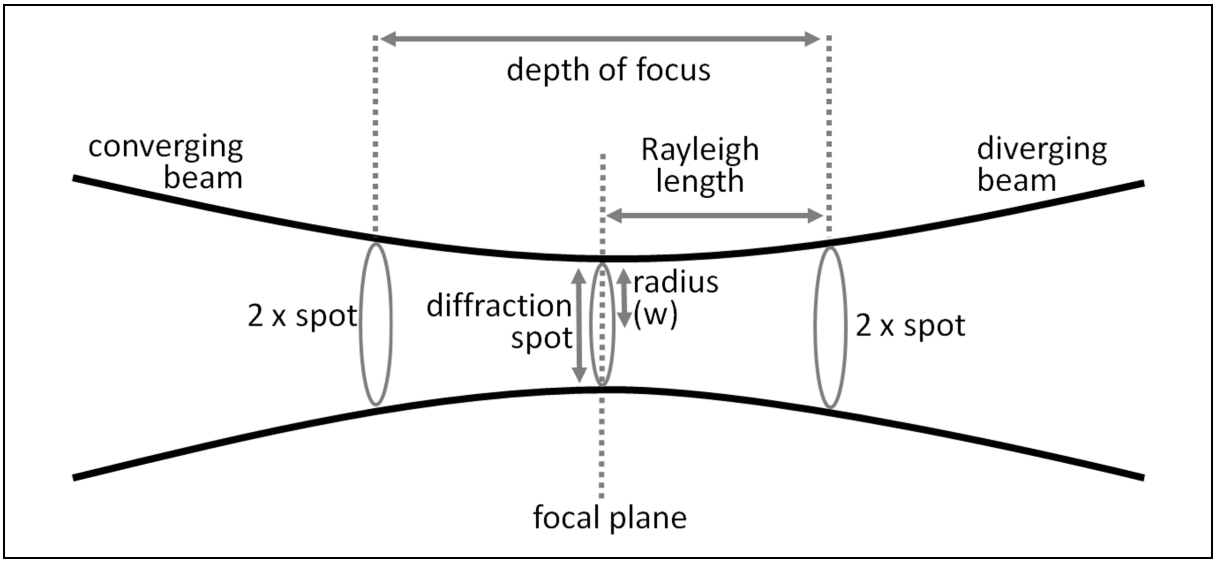

Figure 2.3: The depth of focus is the area over which imaging is in focus and the waist size has grown by only a small factor.

is defined as,

$$DOF = \frac{\pi(w)^2}{2\lambda} \tag{2.5}$$

where ω is the radius of the minimum waist size (i.e., the beam radius), and λ is the centre wavelength of the light source. A threshold must be determined for how much waist broadening is acceptable for the imaging application. This threshold is classically defined as the Rayleigh Range and is twice the diffraction limited spot size. The depth of focus is measured over the space before and after the focal plane and so is given as twice the Rayleigh Range. For the waist radius,

$$w = 1.22\lambda F, \tag{2.6}$$

the depth of focus is,

$$DOF = 1.22^2\pi\lambda F^2 \tag{2.7}$$

where F is the f-number, and λ is the centre wavelength of the light source. If the system has the capability to image beyond this depth of focus, the spot size grows and as the spots begin to overlap each other, there will be less differentiation. Blurring will occur and there will be less specificity in the images. However, generation of images will still be possible

and may yield useful results. Typically, the entire penetration depth will not be within the depth of focus, but will still yield useful information.

There is a general trade-off between lateral resolution and depth of focus. The lateral resolution is governed by the Rayleigh Criterion for a given wavelength of light and diameter of lens; the focal length is the variable quantity. A low f-number yields a low depth of focus system, but will have high lateral resolution. The use of a high f-number will degrade the lateral resolution, but increase the depth of focus. Design parameters dictate that the spatial resolution should be as small as possible, but the depth of focus should be as large as possible. There are times when better depth is more desirable than better spatial resolution capabilities. If high penetration depth with modest resolutions is acceptable, as in the case of cancerous tissue margin detection, a higher f-number lens is important. When imaging cellular histology, however, where high resolution is important, a low f-number focusing lens is a key to success.

2.1.10 Paraxial ray tracing

Paraxial ray tracing follows the path of light rays through an optical system. Paraxial ray tracing assumes the rays are close to the optical axis and nearly parallel to it. As such, the angle of incidence is limited to the regime where the small angle approximations, $sin\theta = \theta$ and $tan\theta = \theta$, are valid. The schematic for developing the ray tracing equations for a single lens is illustrated in Figure 2.4. Paraxial ray tracing can be used to find the relationship between the incident beam angle and lateral displacement of the beam in the focal plane. The resultant paraxial ray tracing equations [1, 23] are,

$$x = x_0 + t\theta_0 \tag{2.8}$$

and

$$\theta = \theta_0 - x_0/F_L \tag{2.9}$$

where x is the distance between the optical axis and the beam spot on the focal plane, x_0 is the distance between the optical axis and the origin of the incident ray, t is the distance between the lens and the sample. In equation (2.9), θ_0 is the angle between the incident ray and the optical axis, θ is the angle of the refracted ray, and F_L is the focal length. By substituting equation (2.8) into (2.9) and placing the sample at the lens focus ($t = F_L$), the system is described by,

$$x = F_L\theta_0 \tag{2.10}$$

where θ_0 is the angle between the optical axis and the incident beam (in radians), F_L is the focal length, and x is the distance from the optical axis to the location of the beam on the focal plane.

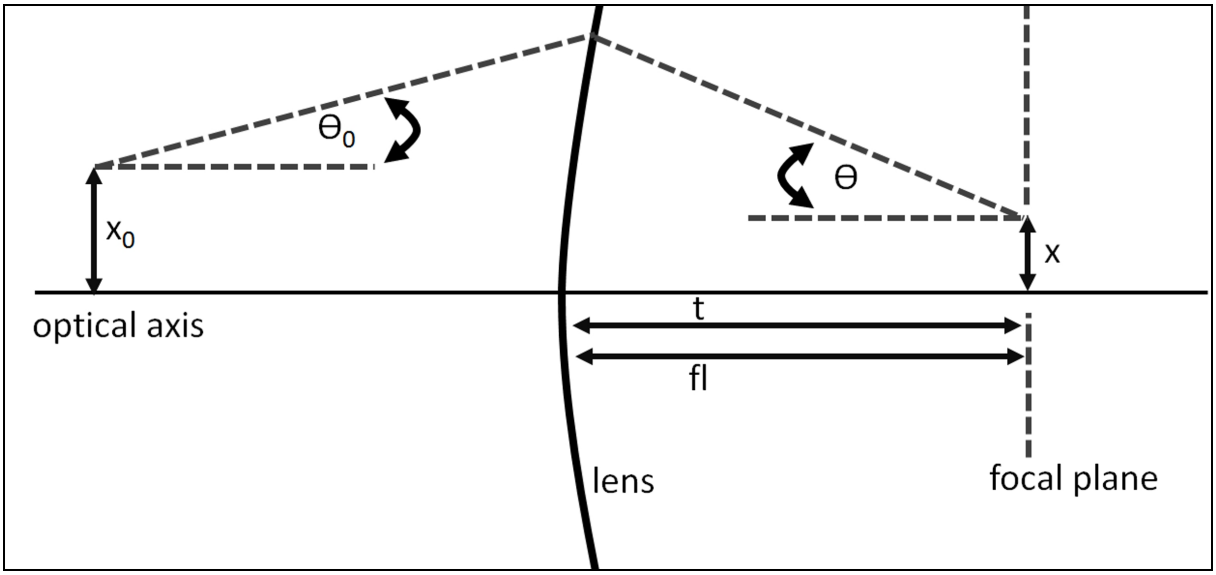

Figure 2.4: The ray tracing equations can be developed for propagation through one lens.

2.2 Electronics background

Today, imaging systems integrate optics with electronics to enable high performance imaging applications. The various components are synchronised with a microcontroller using digital transistor-transistor-logic (TTL) voltage signals (high or low) and analogue voltage signals (continuous). Additionally, custom integration cables provide the communications necessary for the microcontroller to manipulate the positions of motors and other actuators.

2.2.1 Position noise

When determining the specifications for electronic components, it is often the case where movements must be within a threshold, e.g., less than 1 μm. This is the resolution of the system, but does not tell the whole story; just as important is the position noise. Position noise is the certainty to which a mechanical element can be held to the commanded position. Position noise can be given as a root-mean squared (RMS) error quantity or a peak-to-peak error. Position uncertainty is caused by sources like backlash, when the moving component oscillates after motion; friction, when the motion is restricted from moving as far as commanded; and stiction, where additional energy is necessary to get the element

to break free from rest. Also important is the minimum step-size which is governed by the resolution of the position sensor, typically an encoder.

2.2.2 Stepper and servo motors

The most common actuators for motion control are stepper motors, servo motors, and piezo-based systems. Servo motors have the capability to be more accurate than stepper motors, and piezo systems have the capability to be more accurate than servo systems.

Stepper motors include a cylindrical rotor surrounded by ferromagnetic teeth. The rotor is surrounded by poles and based on the pulsing of current through the poles, rotational movements are generated via attraction between the poles and the teeth. Pulsing current in a specific order generates rotation and one discrete rotational element is called a step. The typical step size for a stepper motor is 1.8 ° rotation, providing 200 unique and repeatable locations per 360 ° rotation. Since the pole activation sequence must be in a specific order to generate motion, a microcontroller must be used to run a stepper motor. Some microcontrollers also support microstepping operations. The poles are activated as usual, but rather than supplying the full current, micro-steps split the current between the present pole and the next pole. By varying current between the poles, additional locations may be obtained. Microstepping is thereby limited by the resolution that the controller can generate current and the friction and stiction inside the motor that may prevent small steps from occurring. If the micro-step does not generate enough magnetic force to overcome motor stiction, the rotor will not turn. Generally, single step microstepping should be avoided, especially if commanded from rest. Current must be applied at all times to a stepper motor, so the rotor will hold it's position unless commanded to move. [24]

Stepper motors are used in various configurations to transfer rotational movement into linear translation, such as worm gears, lead-screws, or ball-screw mechanisms. Stepper motors offer unbeatable cost to performance ratio for open loop applications, but are not suitable for all situations. Steppers are ideal for simple motion profiles where low speed and high torque are important. Stepper motors use the system friction to their advantage and limit overshoot. Steppers are actuated by indicating the size of step (the number of microstep sequences to move through) and the direction of travel [39].

A servo is an actuation mechanism that uses closed-loop feedback to provide control over the position of the shaft. Servos come in a variety of form factors from hobby-type radio controlled (RC) servo motors, to linear shaft motors. They are actuated in a variety of forms specific to the type of motor. Common control schemes are pulse-width modulation, where the peaks and valleys of a square wave are manipulated with relation to

the desired movement; and analogue voltage control, where the motor is sent to a position proportional to the amplitude of the input voltage. Servo based solutions are ideal for situations requiring high speed, high acceleration, and high precision.

Piezoelectric motors use the theories of the piezo-effect to generate movement. When a voltage is applied across a piezo crystal, it expands. By coupling many of the crystals together, there is appreciable expansion that can be used to move a carriage. Total piezo expansion is typically small, e.g., 200 um, and can be harnessed to provide small step sizes, e.g., 1 nm. Piezoelectric drives suffer from drift, hysteresis, and do not perform as efficiently when pulling a carriage versus pushing the carriage. [24]

2.2.3 Galvanometers

Galvanometers are motor-mirror combinations that operate over a fixed angular excursion with ratings like +/- 20 ° mechanical. Galvanometers have fast step response times compared to other mechanisms of manipulating a light beam or sample. A complete galvanometer system includes the galvanometer, the mirror, and the servo driver that commands the mirror to a known position with closed loop control. The galvanometer itself is more than just a motor; while galvanometers do feature the standard coil and magnet of a motor, the body also includes an internal position detector. The position detector provides the necessary position information for high accuracy performance [8].

Galvanometer drivers are classified into two categories: Class 0 or Class 1. Class 1 systems are Proportional Integral Derivative (PID) feedback systems and offer better positional accuracy than Class 0 systems. Class 0 drivers offer higher speed than class 1 drivers, but the additional speed comes at a cost of accuracy. Class 0 drivers do not include the error integrator found in Class 1 systems. This additional feedback in Class 0 drivers affects the final positioning of the mirror and slows the process to ensure the position is accurate. The mirror thickness, profile, and material are important considerations for overall performance. Each of these affects the mirror's inertia and the ultimate range of operation. Many imaging systems use two galvanometers to enable two-axis positioning. In two-axis galvanometer systems, the second mirror must be larger than the first mirror since it must accommodate the full aperture at an angle and also the displacement of the beam caused by the first mirror [8].

2.2.4 Stages

Stages provide translation, be it rotational or linear, and restrict movement to specified paths. A carriage moves along a rail and may be supplemented by various ball bearing mechanisms to enhance smoothness and linearity, while reducing friction. Stepper based stages move along a dovetail rail with a cap-screw or ball-screw mechanism sliding along. Many high-precision servo based stages use cross-roller bearings. They are ideal for situations requiring high stability, heavy loads, off-axis loads, and long term precision [25]. Cross-roller bearings use cylindrical balls, rather than round and include perpendicular orientations across alternating cylinders [24]. As a result, cross-roller bearings have a high contact area between the mounting plate and the bearing, which allows for higher pre-loading capability and higher resulting payload mass capabilities. With ball based mechanisms, the changing contact point as the ball rolls during movement induces parasitic oscillation and is a major source of the position noise. [27]

For imaging applications, the important specifications for selecting stages are the encoder resolution, the stroke (travel length), and repeatability. The encoder resolution is not the only characteristic that must be considered with respect to position accuracy. This resolution rating may be less than or more than the obtainable position accuracy. However, the minimum step size is related to the encoder resolution. Generally, the stage may not be moved less than one encoder count, but in many cases, it is possible to move the stage carriage only one encoder count. Specifications also quote the step response times, but the step response is quite sensitive to the particular loading and applied motion profile and should be tested within operational parameters.

2.2.5 Step response

To test a stage or galvanometer, a step pattern may be applied. By moving the actuator forward and backward in position, the behaviour of the system can be characterised. The commanded motion profile takes the form of a square wave input. The position output also has a typical shape, as illustrated in Figure 2.5. The rise time is the period from the start of motion to the arrival to the commanded position. The settling time is defined as the time from the start of motion until the motion has stopped oscillating within a threshold of the desired value. The peak time is the period from the start of motion until the maximum value is reached. Finally, overshoot is the amplitude of the signal at the peak time less the commanded position; it indicates the degree to which the system moves beyond the desired location and is often given as a percent [12].

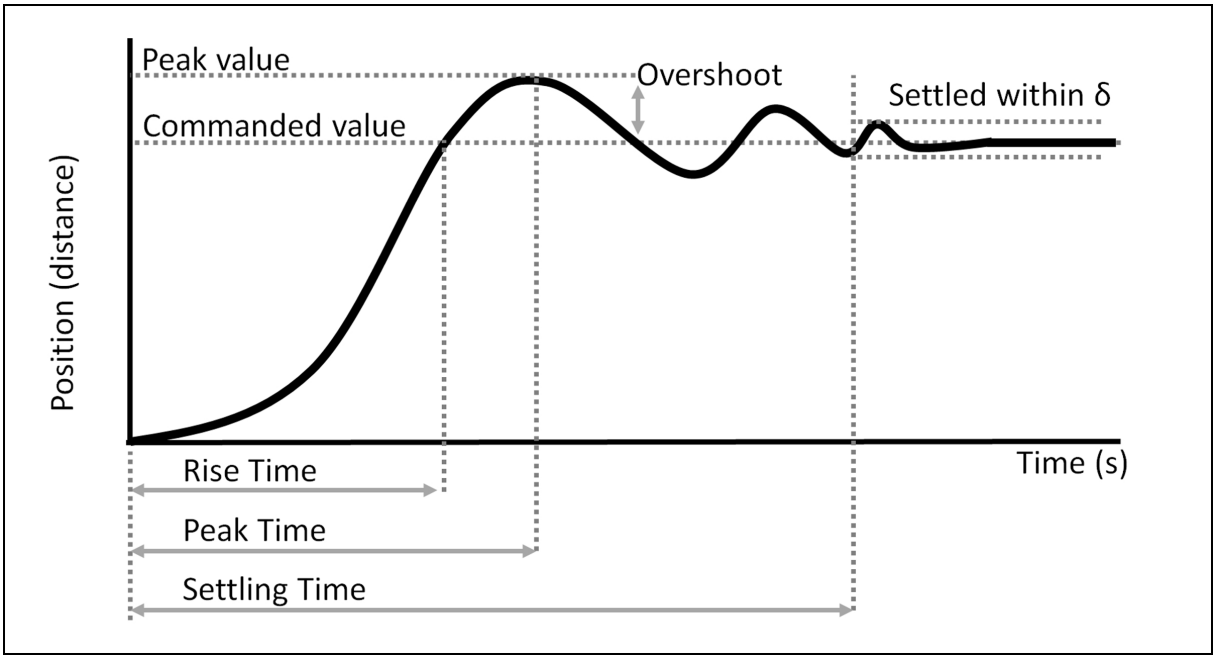

Figure 2.5: There is a typical shape for the motion response to a stepped input (adapted from [12]).

The step response can only be measured if there is a position sensor on the actuator. The speed and degree to which errors are corrected in a closed loop system can be manipulated by tuning the gain values for the control loop. In the common PID controller, there are three gain values that can be changed: K_P, K_D, and K_I. The K_P and K_D gains have the largest effects on motion and K_I is used to fine tune the performance. The common PID controller is described by,

$$G(s) = K_P + \frac{K_I}{s} + K_D s \tag{2.11}$$

where G is the filter output and K_P, K_I, and K_D are the tuning parameters.

During a step command, the motor is sent from one position to the stepped position instantly. The motor will obviously take time to move and there is less fatigue on the motor if the rising edge is sent as a sloped line rather than a jump; this is called slew limiting. Slew limitation is often incorporated into a galvanometer driver and modifies the input command to a command that is smoother for the system to execute. Rather than depend on the slew limitation, it is better to code the movements to occur in the amount

of time available. This reduces current in a motor's coils and the resulting heat generated. Current and the amount of heat that can be dissipated often limit the system speed in galvanometers. This is only a major consideration for large movements, like the scan-back from the end position to the start position of a scan. There is evidence that scanning in only one direction and limiting speeds during the scan-back can yield faster total scan speeds [3]. This is primarily a concern if the application nears the maximum galvanometer oscillation speed.

2.2.6 Scan patterns

There are different terminologies used to distinguish scan movement directions. In satellite based imaging where the craft itself is traversing the Earth's surface (or, the Earth is moving beneath the craft), along-track is used to identify the direction that is the same as the craft is moving. Across-track is used to identify sweeping movements that are perpendicular to the along-track motion. In medical imaging, it is more common to denote the across-track direction as lateral or transverse. In OCT, an across-track scan is known as a B-Scan. A depth profile taken at a single position is known as an A-Scan.

There are two main styles of scanning: raster scanning continuously, and step and hold scanning. For raster scan applications the beam is moved across a sample and does not pause for sensor integration. This type of scan mechanism is used in laser marking and some laser microscopy applications. A step and hold architecture is used when the sample and light beam need to be held still during sensor integration. This is especially important when integration times are long, or multiple images are taken of one location.

To cover a 2D surface, there are many scan patterns that can be used. In order to minimize blurred pixels for medical imaging, a step-and-hold pattern is desired. Potential actuation waveforms are illustrated in Figure 2.6 along with the resulting ground swaths produced. These illustrations show ground swaths generated by two-axis control and the same patterns can be generated whether the axis are controlled via two-galvanometers, two-stages, or a galvanometer-stage combination [17]. In each of the patterns of Figure 2.6, the actuation signal is shown along with several numbered points. The numbered points correspond to the locations where the scan beam is incident with the sample. Using a synchronisation scheme where an image is taken at regularly spaced intervals is a simpler architecture to implement than a position based imaging timing, but does restrict the scan pattern to linear movements; sinusoidal movements generate uneven spacing.

The first result (A) shows the ground swath generated by a triangular waveform input. A triangular wave causes the imaging to track linearly across the scan area. This waveform

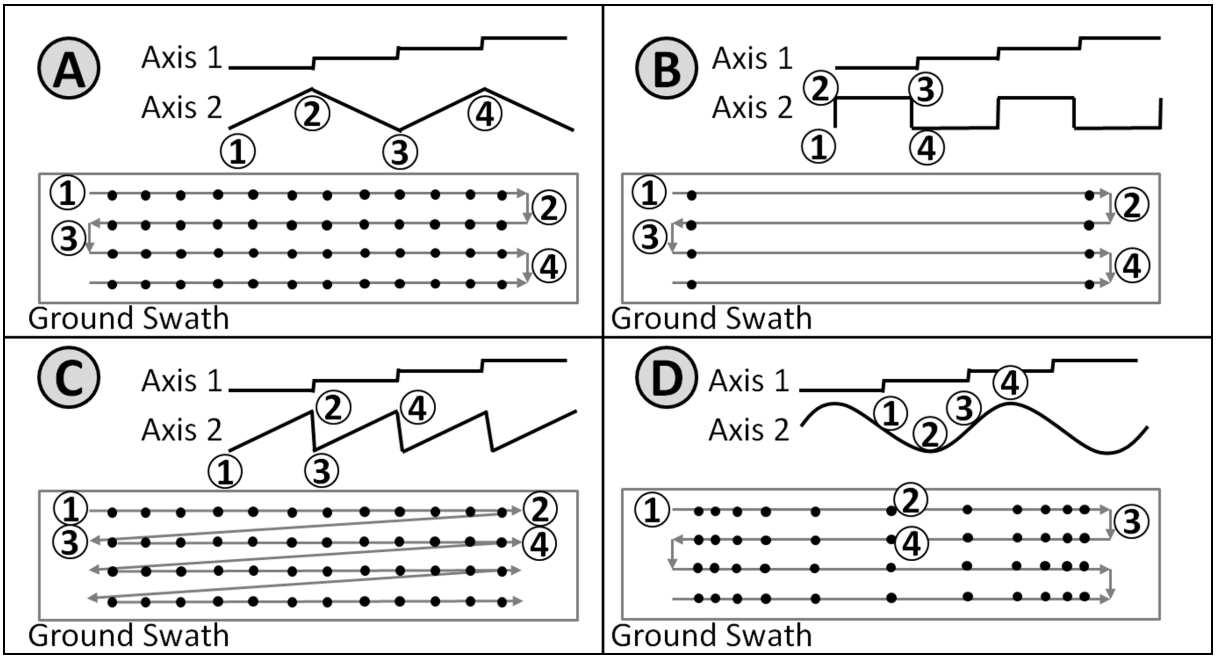

Figure 2.6: Various scan patterns can be produced with two axis control (adapted from [32, 34]).

acquires imagery in forward and backward across-track directions to make efficient use of movements across the sample. Each period of the triangular wave represents one full scan forward and backward. After each across-track is complete, the actuator is given a signal to move forward in order to generate an adjacent across-track scan. Other research [42] used triangular waveforms successfully, but caution should be taken because sharp directional changes that may lead to longer settling times.

A square wave (B) sends an impulse for the imaging location to jump to the opposite side of the sample. The ground swath starts at one end of the across-track scan and as quickly as possible jumps to the other side. With the scan location changing so quickly, there would be limited time to generate images across-track and so images are only taken at the extents.

The sawtooth waveform (C) is a combination of a triangle wave and a square wave. This waveform scans at a constant across-track direction and instead of scanning in reverse towards the initial position, the scanner is commanded to jump back to the starting position. If implemented as a steep slope, rather than a sharp falling edge, better performance

may be possible, as described in the preceding Step Response section.

Finally, a sinusoidal waveform (D) is undesirable since the distance between sample locations changes with the changing slope of the waveform. A benefit of sinusoidal scanning is the smoothness during direction changes, which leads to reduced settling time.

2.3 Applications

2.3.1 Optical coherence tomography

Optical coherence tomography (OCT) is a three-dimensional imaging modality with μm level resolution. Medical OCT systems image internal micro-structure in biological tissues by measuring backscattered light [13]. OCT imaging includes many advantageous characteristics: high resolution, non-invasive, non-contact, use in fibre-optics (e.g., in an endoscope), high speed, non-harmful radiation, and inexpensive compared to other imaging systems (e.g., MRI). The basic configuration of a spectral domain OCT (SD-OCT) system is illustrated in Figure 2.7. OCT splits an incident beam into a reference arm and a sample arm. The interference between the sample arm and the reference arm allows for structural information to be determined from the resulting interferogram. For interference to occur, the path-length of the sample and reference interferometer arms must be the same. Thus, if the sample arm path-length changes, there must be an associated change in the reference arm path-length.

Each wavelength of light interacts with the sample's structures and the deeper the structure, the larger the phase delay for the particular frequency. By passing the return beam through a diffraction grating, the interfering beam splits to constituent wavelengths and can be read by the sensor in a single exposure. The combined set of broadband phase delays form a sinusoid for each structure. The sinusoids can then be reconstructed to yield a depth profile. Light that scatters once within the layers of the sample and is back reflected into the system provides useful information, while light that scatters multiple times adds to the system noise. The multiply scattered light will travel a longer optical path and show up as an inaccurate reflection location. Scattering generally limits depth penetration of OCT to less than 2 mm [9]. A scan of a single location with an SD-OCT system produces the depth profile, an A-scan, while a collection of A-scans in the across-track direction makes up a B-scan.

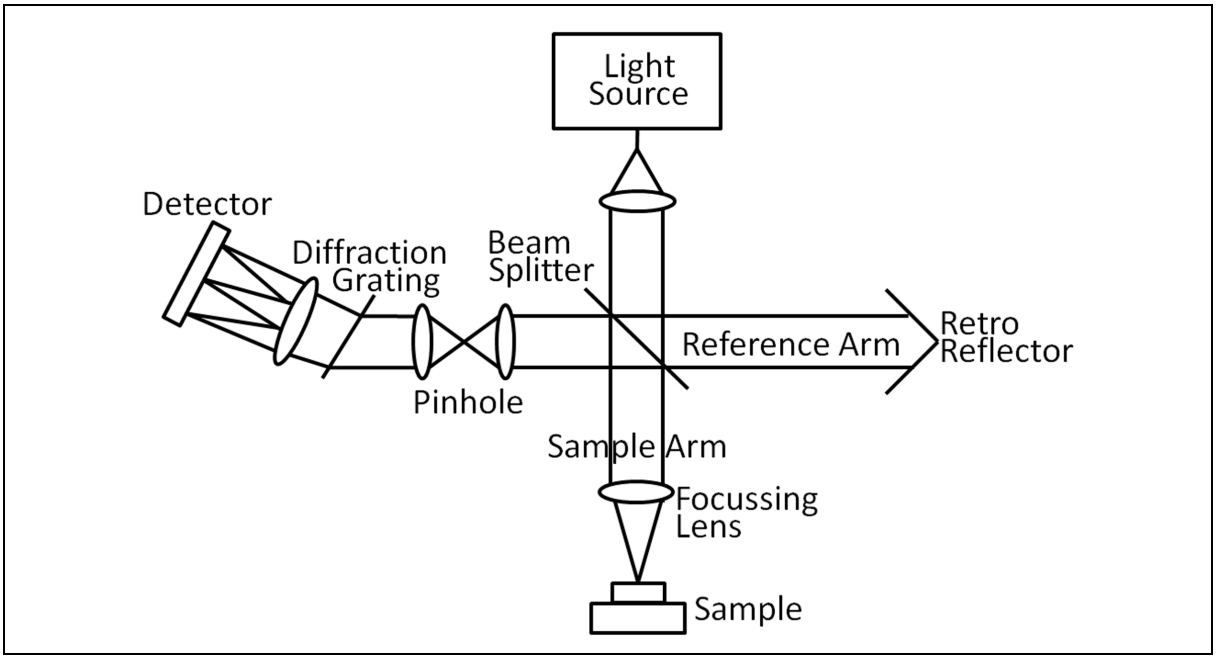

Figure 2.7: The architecture of an optical coherence tomography imaging system includes a Michelson Interferometer and a spectrometer.

2.3.2 Margin assessment

One of the many applications for OCT is assessment of surgical margins during tumour excision. The predominant way of determining if a tumour has been wholly removed is to examine the removed tissue and identify if a layer of healthy tissue surrounds the tumorous tissue. There is no consensus among radiation oncologists about what constitutes a clear margin. Generally, 1 mm or 2 mm [6] of healthy tissue excision around a tumour is accepted as a clear margin. There is a growing trend to move to smaller margins and many specialists state that if no cancerous tissue is present at the surface of the excised tissue, the margin is negative [2, 26]. The tissue is examined after the operation and if a positive margin exists, re-excision is necessary. Re-excision may also occur as a safety factor if there exists a margin, but the tumour is close to the surface.

A procedure where margin assessment is conducted is breast conserving surgery (BCS) where a tumour is removed and as much of the healthy breast tissue is left behind as possible. Re-excision is necessary in as many as 54 % of BCS cases [2] and in a study of

local recurrence rates, 8.4 % of BCS patients suffered recurrence when a 2 mm threshold was defined as the clear margin [6]. Re-excision adds cost in the form of additional operating room and physician time, but also in the form of another invasive surgery for the patient.

The gold standard for identifying the presence of a margin is pathological examination under a microscope [7, 26, 28]. A paraffin embedded sample is examined post-operatively in slices 3 mm thick. A 5 μm section is taken from the 3 mm slice for examination [6] and as such, this process faces sampling rate issues. Microscopic evaluation does not probe depth and so is limited to obtaining data from thin sections with the hope that the thin sections are representative of the remainder of the tissue. The excised tissue is removed in a process called Mohs micrographic surgery [4] where the tissue is oriented by inking each margin with a different colour so that it can be matched to the removal site.

Pappo et al. indicate spatial resolution as low as 0.15 mm as sufficient for examining excised tumours, but other work [7] notes that mm sample spacing may be sufficient for margin detection. OCT has been used successfully in detecting margins, but the clear limitation is an effective sample handling system for increasing scan coverage and solving the sampling rate issue. There are many other techniques for assessing margins including touch prep cytology [7], Raman Spectroscopy [16], and frozen section analysis [7, 28], but none has yet proven to be a standard intraoperative procedure for margin assessment.

2.4 State of the art

Scan systems are used in a variety of fields, e.g., laser marking, medical imaging, remote sensing, and manufacturing quality assurance. One of the most mature fields is remote sensing from satellite platforms. There are several standard remote sensing architectures that have been developed since the space age began in the late 1950's. The three most common satellite imaging architectures are illustrated in Figure 2.8. There are many similarities between satellite scanning and medical imaging [17]. The types of components in scan system hardware are often the same regardless of application and differ only when there are unique requirements for the environment. For example, space based scanners may require low-power operation, or medical scanners may need to be able to operate in magnetic fields, like if near an MRI facility, and this may drive the design. The hardware configuration, scan patterns, and light interaction effects are all very similar and perform the same types of multi-spectral scans despite occurring over vastly different distances.

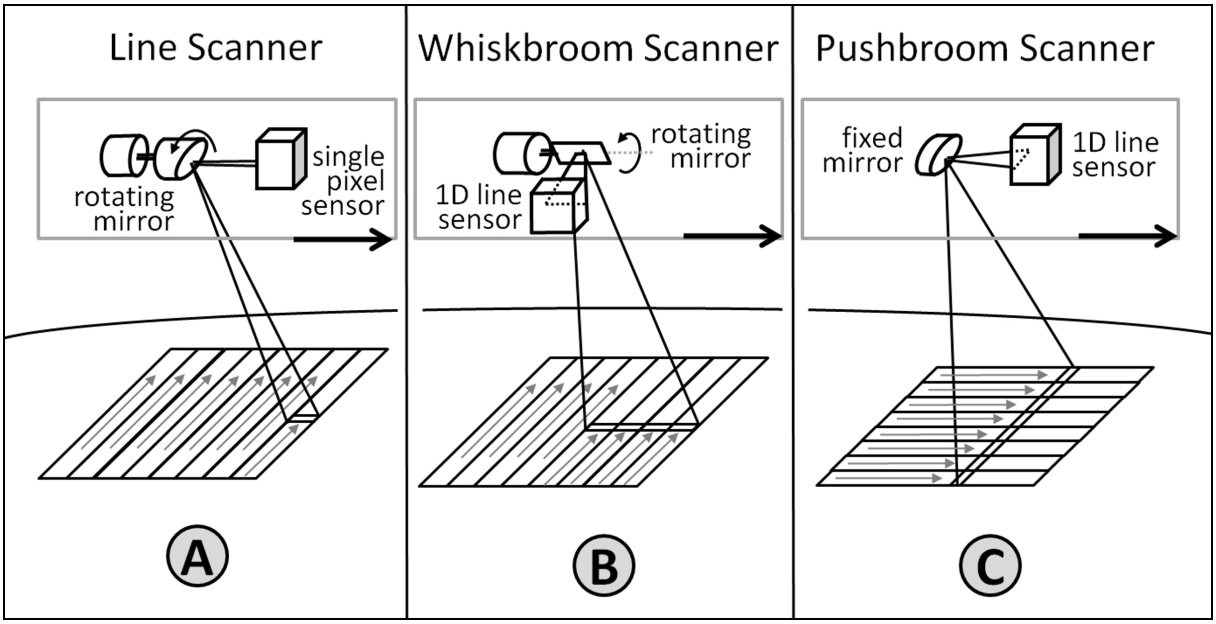

Figure 2.8: Line-scan, whiskbroom, and pushbroom imaging systems are used commonly in remote sensing applications. Remote sensing is a relatively mature field of study that makes effective use of scan systems (adapted from [32, 34]).

2.4.1 Line scanners

Line scanners [34] feature a rotating mirror, as illustrated in Figure 2.8, (A). Earth radiation enters the satellite, reflects against the scanning mirror and is sent to a sensor. The across-track image is created one pixel at a time, line by line. The along-track procession occurs as the satellite moves through its orbit. Since there is movement in both the along-track and across-track directions, the dwell time is low and noise is prevalent. The advantages to using line scanners include simple optics, large fields of view, and inherent registration for multispectral scans. Multispectral scans diffract the incoming beam into the constituent wavelengths and each frequency is focussed to one pixel in a linear array. The major disadvantage of line scanning is the wasted scan time when the mirror faces away from the Earth.

2.4.2 Whiskbroom scanners

Whiskbroom satellites [21, 33] are passive systems in which the scanner sweeps across-track and receives a line of information for each pixel in a line detector, as illustrated in Figure 2.8, (B). Since several lines of data may be received simultaneously, it takes the spacecraft less time to achieve the same coverage as a line scanner. Movement in both the along and across-track directions necessitate short sensor integration. Recent whiskbroom scanners [34] use a rotating mirror with reflective coating on both sides to increase usable scan time. Early generation whiskbroom scanners collected data in only one across-track direction; n lines during each scan using n detectors. Each successive mirror sweep was timed so that each set of n lines were adjacent to the previous n, thereby providing continuous coverage. The advantages of whiskbroom scanning include faster speeds, higher sampling density, large ground swaths, and maturity in technology. Notable drawbacks are increased complexity reconstructing and registering data, and decreased reliability due to additional moving parts.

2.4.3 Pushbroom scanners

Pushbroom scanners [31, 33] take advantage of increasingly large sensor sizes. These instruments acquire one across-track swath of data simultaneously for every position in the along-track direction, as illustrated in Figure 2.8, (C). As a result of moving in solely the along-track direction, the sensor is able to dwell longer for each pixel providing increased integration time. The advantages of a pushbroom scanner are simple optical configuration, reduced revisit time, inherent registration, low wear and power consumption, and easy installation aboard aircraft. The disadvantages of pushbroom scanners include the necessity for large detectors, narrow fields of view, and large datasets produced simultaneously which need to be stored and transmitted. Multispectral pushbroom scanning is enabled by placing a diffraction grating before a 2D detector. One dimension of the detector is used to provide the line of scan data, while the other dimension receives the spectrum. Registration of various channels is inherent since the spectra pixels are tied to spatial location.

2.4.4 Medical imaging scanners

There are several configurations of light delivery systems available for medical imaging devices. Most often, systems use two galvanometers to perform 2D beam positioning [30]. The high speed operation of galvanometers allows these systems to change the beam

position quickly, yet maintain accurate location positioning. However, the systems are limited in the size of sample they can accommodate. When larger galvanometer scan angles are used, the system inertia limits the scan frequency to lower rates. Additionally, if focusing the beam with a single lens, the farther from off-axis the beam is transmitted, the more aberrations will be present.

A galvanometer-translation stage system has been used in confocal microscopy applications (BPI). It uses the galvanometer to produce across-track motion, while the stage moves the imaging line along-track. The beam is focussed beneath the galvanometer via an f-theta lens. The f-theta lens allows for clear scanning over large scan angles that would normally be subject to significant spherical aberrations. The image is collected one pixel at a time with a single pixel detector.

Techniques analogous to whiskbroom scanning are rarely seen outside of research labs in OCT due to the complexity and cost associated with multiple beams. A four beam approach [36] was successful in yielding 10 μm longitudinal scanning resolution and improved throughput versus a single beam design, but is a highly complex system featuring four interferometers and four sensors. Another multi-beam scanner design [38] uses three interferometers, but places the spectra side-by-side on a single sensor in order to image all three A-scans on one sensor simultaneously.

There are also micro-electromechanical system (MEMS) driven mirror devices. A MEMS scanner [42] using torsion hinges can replace a full size galvanometer for directing a beam in OCT. However, at only 2.5 mm x 2 mm, the size of the mirror surface is a limitation. These systems are more appropriate for fibre optic based systems or those will small beam diameters. Their performance does rival larger systems and has the capability for 45 $^\circ$ oscillations.

Chapter 3

Trapeze

A sample handling and light delivery system was designed for use in three-dimensional OCT. The device is an electromechanical system consisting of electronic components, optics, and mechanical hardware. Termed "trapeze," the system is designed to be a flexible component of a test-bed OCT system. Key functional requirements of the trapeze are:

1. Flexibility in sample size
2. Three-dimensional imaging: trapeze provides two dimensions, while OCT inherently provides the third
3. Accommodation of a variety of beam sizes and intake heights
4. Easy alignment
5. Flexibility in scan sampling rate and pattern
6. Ability to control angular range in order to limit off axis aberrations

The OCT system, as a test-bed for experiments and new hardware components, would have no constant size of phantom or sample. As such, flexibility and accommodation for a variety of samples are key requirements. For scanning to retain high resolution and occur in a reasonable amount of time, as necessitated by a clinical use, sample sizes are limited to several cm^2 in area. The trapeze provides the sample arm of the OCT interferometer and light is injected into the trapeze following the beam splitter, as illustrated in Figure 3.1.

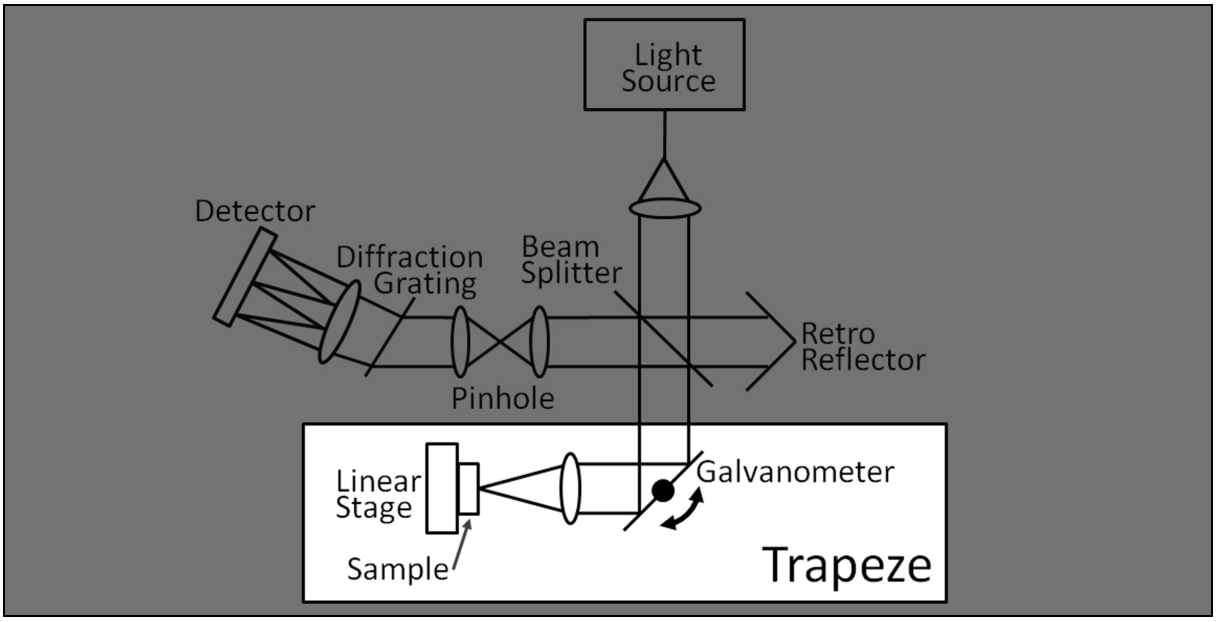

Figure 3.1: The trapeze is the sample arm of the OCT interferometer. 50% of the broadband light enters the trapeze and travels to the sample.

3.1 Hardware configuration

Two trapeze iterations were designed and constructed for light delivery in OCT. The first iteration of the Trapeze was based upon a Thor Labs galvanometer (THG) and was designed to use entirely off-the-shelf, low lead-time components. The second iteration was based around a Nutfield Technologies galvanometer (NTG) and integrates design improvements from the initial use of the Thor Labs system. The Nutfield based solution uses custom mounts in combination with off-the-shelf components.

3.1.1 First Iteration

The trapeze is based around a galvanometer and linear stage combination to provide control over where the beam and sample interact. A pair of optical posts provides a mounting platform for the majority of trapeze components. The posts are easily coupled with many off-the-shelf components and provide flexibility in mounting height since the mounts can slide up and down. The Thor Labs based trapeze includes five major component sets,

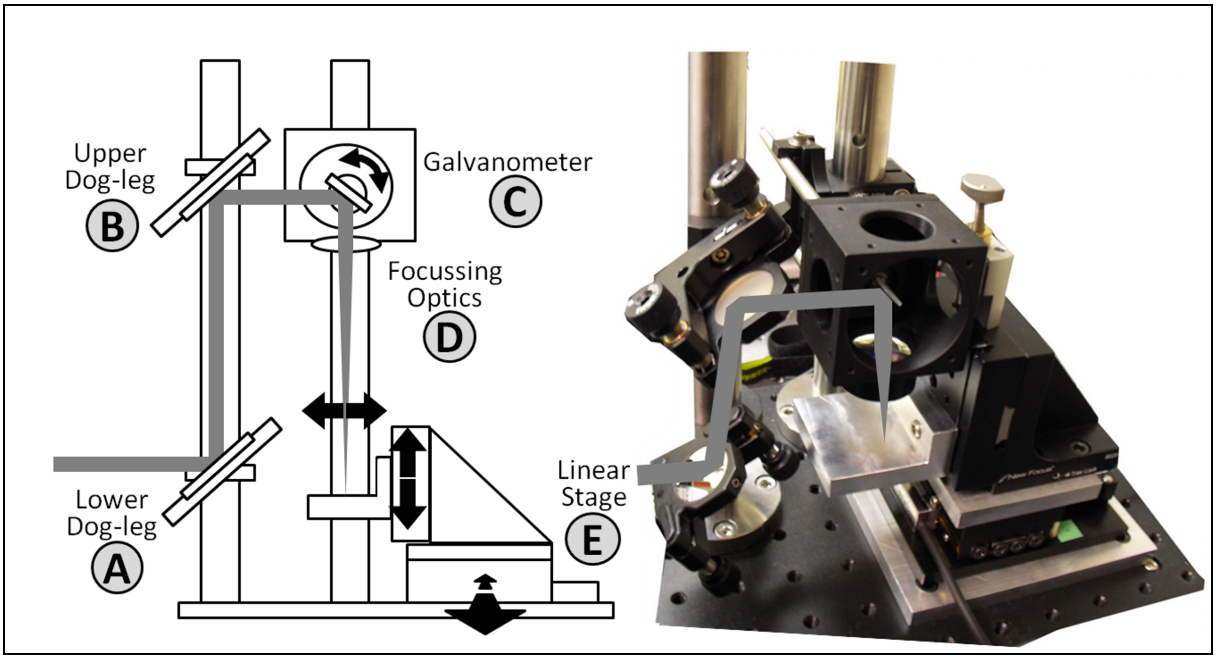

Figure 3.2: There are five major component sets in the Trapeze: the lower dog-leg (A), the upper dog-leg (B), the Galvanometer (C), focusing optics (D), and the linear stage (E).

as illustrated in Figure 3.2. Each of the major components: the lower dog-leg (A), the upper dog-leg (B), the Galvanometer (C), focusing optics (D), and the linear stage (E), are moveable and aligned independently from each other. This design allows for ample flexibility during the initial development and requirements finalisation phase of the OCT system.

The lower (A) and upper (B) dog-legs are mounted on the first post and use protected silver mirrors ($\phi = 25.4$ mm). The broadband light source is centred at 850 nm (100 nm bandpass) and protected silver mirrors provide reflectivity above 97% [40] over the near-infrared range of operation. C-Clamp mounts wrap around the post and are clamped into place with a set-screw. The C-Clamps couple a kinematic mirror mount to the post. Each of the dog-legs can be moved independently to accommodate any height entrance beam. The reference arm and sample arm path length must be equidistant to yield interference and ultimately a depth profile. To keep the system a manageable size, the sample arm path length is reduced to as small a size as possible. The inclusion of an adjustable height dog-leg allows for minimal space between the lower (A) and upper (B) mirrors. The distance

between the mirrors is governed by the position of the galvanometer, the focusing optics, and the entrance height of the beam. The distance between the focusing optics and the sample is the focal length of the lens and this sets the galvanometer to a known height. The mirrors are mounted in kinematic mounts for two reasons. First, achieving a reliable angle between the C-Clamp and the mirror mount is difficult due to the nature of the set-screw securing the system. Tightening the C-Clamp to the kinematic mount changes the angle between by a small degree and it is difficult to predict the tightened alignment. Additionally, kinematic mounts can mitigate any offset to beam straightness as the beam enters the trapeze.

The TLG (Thor Labs GVS001) is a 1-axis system that is compatible with the Thor Labs cage framework (using galvanometer mount GCM001), illustrated as component (C) in Figure 3.2. The cage framework mounts components using thin rods and so the galvanometer mount is secured to the cylindrical post using these rods. The cage system allows for rapid prototyping, but is not a preferred solution beyond the prototype stages due to increased complexity and number of components. The galvanometer cage mount is held by two 6 mm rods and couples to the main mounting posts using a cage clamp mount (Thor Labs C1026 Clamp). The Thor Labs galvanometer accommodates a 5 mm beam and features a silver coated mirror. The OCT interferometer and spectrometer were designed for beam sizes larger than 5 mm and so an iris is required to shutter the beam down to a size the galvanometer can handle.

The galvanometer is actuated by an analogue input voltage and the frequency and amplitude of the signal determine the behaviour of the mirror. There is a linear relationship between the voltage and the output angle of the galvanometer where +/- 10 V input produces +/- 20 ° optical (+/- 10 ° mechanical) movement. Due to the inertia of the scan mirror, there is a maximum frequency at which galvanometers can oscillate. The Thor Labs galvanometer may be sinusoidally driven over its full angular range at 350 Hz and over small angles at 1 kHz [40].

The galvanometer is driven by the analogue output of a National Instruments data acquisition (DAQ) unit (NI USB-6251). The analogue output can produce +/- 10 V and is discretised over 16 bits. The DAQ is synchronised to an internal hardware clock and is able to provide deterministic outputs at specified timing. Multiple outputs from the DAQ are able to use the same clock to ensure each output is precisely synchronised. The DAQ is the centrepiece of the Trapeze electronics and sends command pulses to all the other electronic elements. The DAQ can update at 2.86 MS/s (mega-samples/second), but this signal generation is split between all channels. The fewer channels used, the higher the signal update rates can be.

Beneath the galvanometer a lens tube is coupled to the galvanometer mount. An achromatic focusing lens ($\phi = 25.4$ mm, $F_L = 100$ mm) is mounted in the lens tube, as illustrated in Figure 3.2, component (D). The beam is collimated through the system until it hits the lens where the beam focusses to its minimum spot for interaction with the sample. In general, the smaller the spot size, the better the resolution capabilities of the system.

A Nanomotion linear stage (FB050, HR4 motor) provides position control over the sample and is illustrated as component (E) in Figure 3.2. The stage moves perpendicularly to the movements induced by the galvanometer and features a 5 cm stroke length. The stage uses an encoder (Renishaw RGH25F series, 10 nm resolution) and microcontroller (Galil DMC4010) to provide closed loop feedback over the position of the stage. The stage has a wide variety of speed controls and feedback parameters that may be manipulated in the microcontroller code. The system uses a proportional-integral-derivative (PID) control scheme and parameters may be tuned to achieve ideal position accuracy for the given type and scale of movement. The stage is controlled via a Galil microcontroller and the microcontroller uses the GalilTools language. The controller code for running an OCT scan is included Appendix A. Custom cabling was made to interface the Nanomotion stage with the Galil controller and the DAQ. The Nanomotion stage uses piezo-electric technology where a crystal is excited by a voltage and changes shape. By controlling this changing shape, the piezo crystal acts like a small finger pushing the stage along the motion path [14].

The Nanomotion stage is coupled to a manual Z-axis stage (Newport, 9064-X) using a 90 ° L-bracket (Newport 9029 adapter). The manual stage allows fine control over the vertical position of the sample. Moving the sample up and down changes where the sample is located with respect to the focal plane. The focus is typically placed just inside the surface of the sample in order to achieve the depth of focus within the upper portion of the sample. Additionally, at higher depths, more material has been penetrated and more reflections have occurred. There is a reduction in the number of usable single-scattered photons at higher depths and an increase in multiply scattered photons results in higher image noise. The depth penetration is limited by these multiply scattered photons.

An L-shaped platter is secured to the manual Z-axis stage to hold the sample, as illustrated in Figure 3.2 (E), and is designed to hold a variety of samples configurations. If a single type of sample were to be scanned, a more appropriate platter could be designed with mechanisms to better secure that sample during the scan.

Digital TTL outputs are used to synchronise image acquisition with galvanometer positions and stage movements. Each time the imaging sensor (Basler Sprint 2048spl) receives

a pulse, the sensor integrates for a period of time that is pre-specified in the control code. Each time the linear stage receives a pulse, it moves forward one increment; a distance that is also pre-specified in the control code at scan time.

The trapeze enables 3D imaging. Depth information, an A-Scan, is provided inherently by OCT technology. The 2nd dimension, a B-Scan, is provided by the galvanometer sweeping across track laterally. The 3rd dimension is provided by the linear stage moving along track, perpendicular to the galvanometer movements. A flow chart illustrating the integrated system architecture is in Figure 3.3.

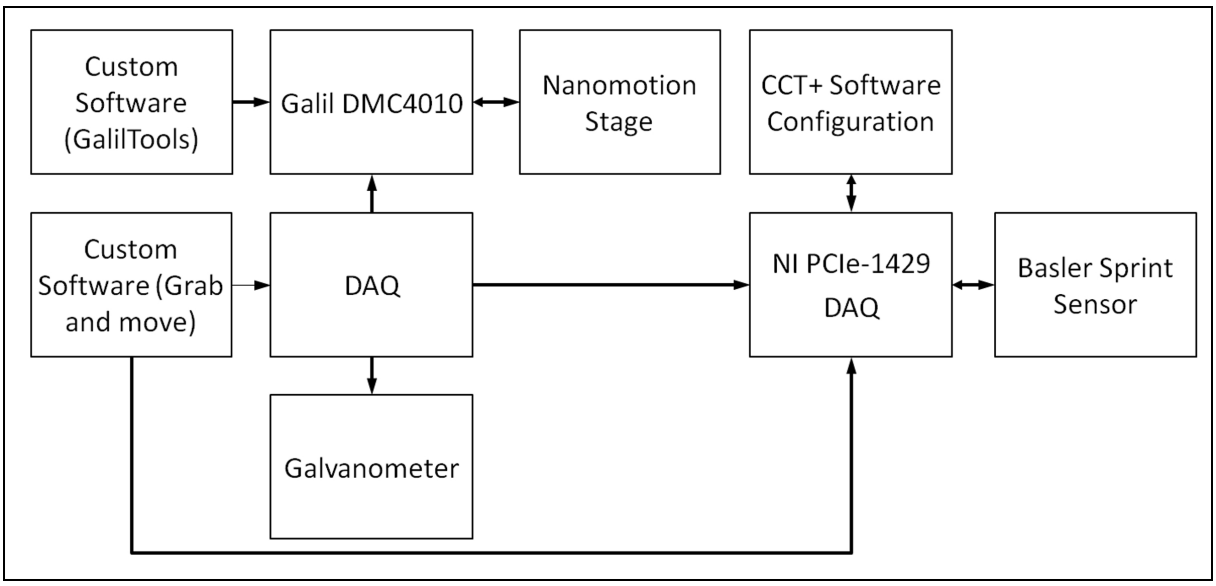

Figure 3.3: The DAQ is the central command point for controlling all of the hardware. The DAQ sends an analogue output to the galvanometer, TTL pulses to the Camera Capture DAQ to trigger an A-Scan, and TTL pulses to the stage when B-Scans are complete.

3.1.2 Second iteration

The second iteration of the trapeze alleviates some of the alignment considerations from the first design. Additionally, the incorporation of a larger galvanometer from Nutfield Technologies (Nutfield Technologies QuantumScan-30) enables the use of a larger beam throughout the system. The beam diameter is increased from 5 mm in the Thor Labs

system to more than 20 mm in the Nutfield based system. The larger beam benefits a test-bed system by enabling experiments that manipulate and slice the beam. A larger beam will provide better collimation (less divergence) over longer distances as the beam propagates through the system [24]. The Nutfield galvanometer is powered by a linear DC power supply (SLD-15-3030-15T) that gives both +15V and -15V. The power supply is stabilized and the differential voltages exhibits better noise suppression.

A custom set of mounts was designed for the Nutfield based trapeze in order to decrease the degrees of freedom and ease the alignment process. The lower mount holds the lower dog-leg mirror and can be moved independently of the other components. The upper mount holds the upper dog-leg mirror, the galvanometer, and the focusing lens. Both mirrors (Thor Labs PF20-03-P01) are protected silver type and retain reflectivity above 97% over the light source bandpass. The dog-leg mirrors are held by 45 ° kinematic mounts (Thor Labs KCB2). Minor misalignment during KCB2 mounting is easily corrected by small adjustments to the tip and tilt of the kinematic mounts.

The galvanometer mount was designed to place the centre of the galvanometer mirror on the same centreline as the beam exiting the upper dog-leg. The galvanometer must be mounted carefully to avoid any pressure points around the motor shaft that might cause additional friction between the galvanometer coil assembly and casing. Additionally, a galvanometer includes internal electronics and encoders to precisely measure the mirror location and must be handled accordingly. A round hole with a slot cut beneath, as illustrated in Figure 3.4 is used to mount the Nutfield galvanometer. A 1/4-20 screw tightens the mount around the galvanometer housing and is friction/pressure held. Galvanometers are typically manufactured with a cylindrical mounting surface so that the shaft and mirror may be rotated to an appropriate starting angle. The galvanometer is inserted into the mount with the mirror set to 45 ° in order to direct the beam directly downwards towards the sample. Beneath the galvanometer, a lens tube mount (Thor Labs LCP01) is fixed to the custom mount and allows for any 50.8 mm lens to be placed beneath the galvanometer. The centre axis of the lens tube matches the centre of the galvanometer mirror so there is automatic alignment. The lens tube was incorporated to allow for additional adjustment of the focal plane location, but the Z-axis manual stage has proven to provide easier adjustment.

The light reflects from the galvanometer mirror and is sent through an achromatic focusing lens (ϕ = 50.8 mm, F_L = 100 mm). The Nutfield based trapeze uses the same Nanomotion stage configuration as in the first trapeze iteration. Despite a beam size of only 20 mm, the trapeze includes 50.8 mm optics. The additional size is used to accommodate for the effective reduction in area that occurs when the optics are tilted at 45 °. The focusing lens needs to be large since the beam will be swept from side to side. The Nutfield based

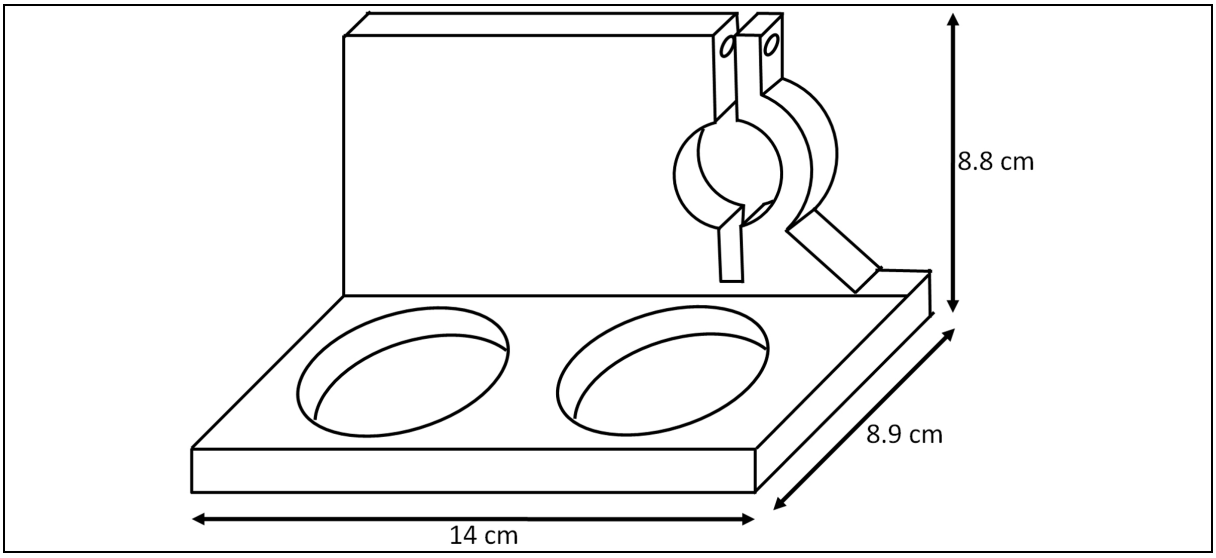

Figure 3.4: The custom galvanometer mount incorporates the upper dog leg for ease of alignment. The galvanometer is secured in place by a 1/4-20 bolt.

trapeze is illustrated in Figure 3.5.

3.1.3 Synchronisation

Trapeze synchronisation operates the same regardless of the galvanometer used. The system matches all movements to timed trigger pulses. For each trigger the galvanometer moves one position step, the camera takes an exposure, and the linear stage checks if the galvanometer has completed the B-scan. The DAQ provides the trigger pulses, as well as the analogue voltage controlling the galvanometer. If the B-scan is complete, the stage receives a trigger from the DAQ to indicate it must move one step forward. This continues until the stage has moved to the end of its desired motion. This is best illustrated by the simple timing diagram in Figure 3.6. The number of A-scans in each B-scan and the number of B scans to capture is customisable and determined a-priori. The trapeze scans across-track to produce a B-scan and during the the galvanometer scan-back to the starting position, the stage moves forward. Only one B-scan direction is used and stage movements are done in a stepwise fashion. There is evidence that using only one scan direction can increase the overall performance of the system since the current within the galvanometer is smaller and time is given for thermal build-up to dissipate [3]. Gener-

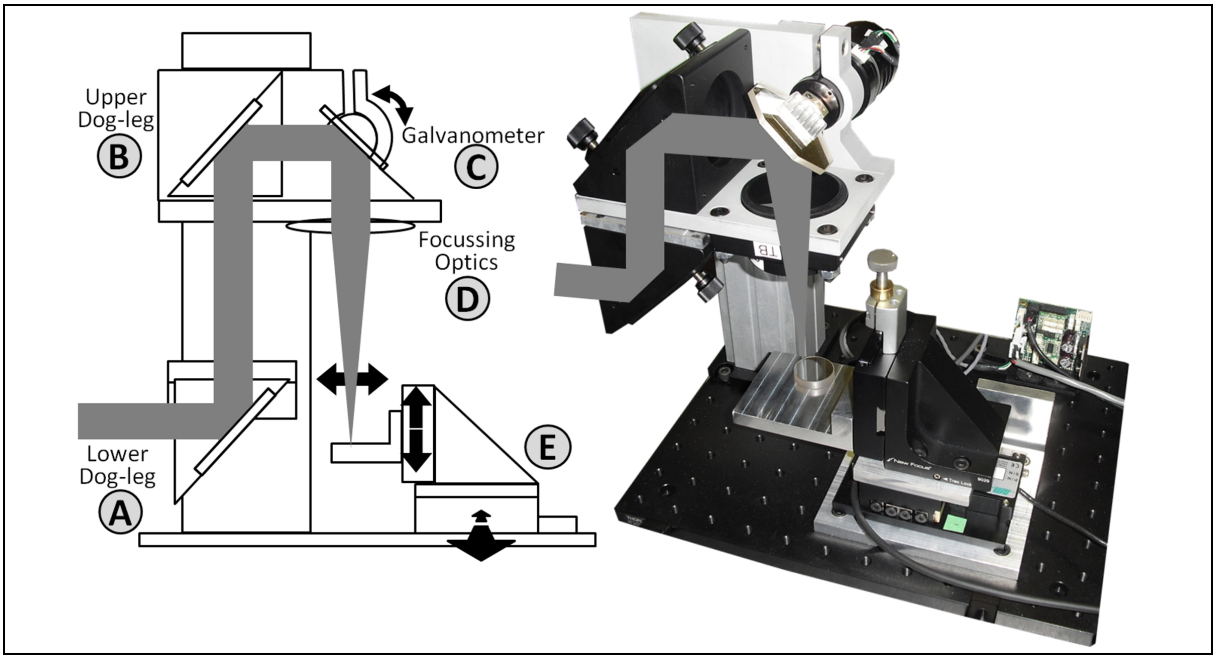

Figure 3.5: The Nutfield based trapeze accommodates a 20 mm beam size and includes fewer degrees of freedom than the first trapeze iteration.

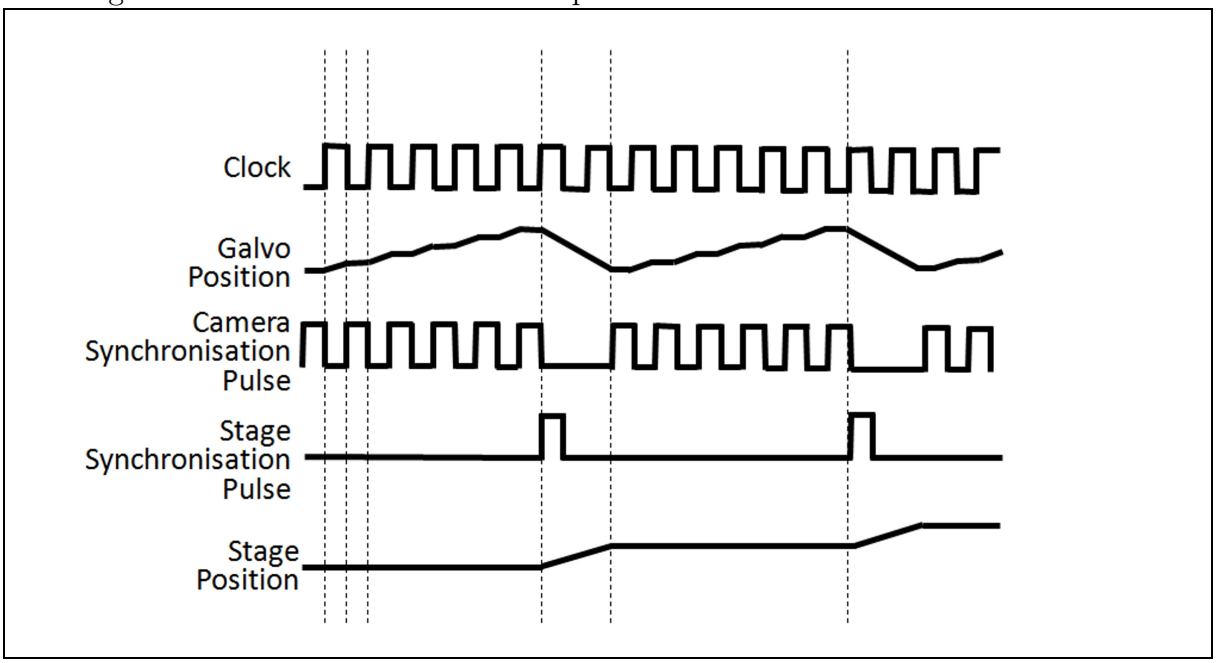

Figure 3.6: Timing diagram and synchronization scheme for operation of the galvanometer, linear stage, and camera exposures.

ally, concern over the amount of current that has built up is more important the higher the mirror oscillation frequency. The galvanometer actuation signal resembles a stepped sawtooth pattern. A step-and-hold architecture for both the galvanometer mirror and the linear stage is used to ensure the light spot is still during sensor exposure. Another potential scheme for galvanometer movement is to sweep continuously, but slow enough that an A-scan sees minimal displacement during exposure. For most A-scans, however, it is desirable to capture multiple exposures at a single imaging location. Averaging repeated exposures helps to reduce photon noise within images [20].

By using one galvanometer and a linear stage, the scan window is limited by the angular range of the galvanometer. The along track dimension is limited by the stroke of the linear stage. Linear stages are available in many stroke configurations and so this second dimension has potential to be very large. Galvanometers can operate at high oscillation frequencies that outpace linear stage speeds. However, the linear stage moves less frequently —only once per full galvanometer B-scan— and so is a less significant limiting factor on the speed of the system. There are three main characteristics that determine the OCT operation speed: the movement of the galvanometer, the integration time of the sensor, and the speed of the stage. Since this OCT system uses free space optics and a large diameter beam, a large galvanometer mirror must be used and the maximum scan frequency is proportionally smaller. The sensor integration time can be changed to accommodate varying reflectivity of sample surfaces, but increasing the sensor integration time is a major factor in the system speed. If multiple images are taken for each galvanometer position, the integration time directly increases scan time. Typical sensor integration times are on the order of a few hundred microseconds.

3.2 System analysis

3.2.1 Spatial resolution

The diffraction limited spatial resolution is determined by the Rayleigh Criterion. The spatial resolution for the Nutfield based trapeze is found using equation (2.4), and is 5.2 μm (for $\lambda = 850$ nm, F = 5). To determine how the galvanometer can be used to generate steps of a known size, paraxial ray tracing may be performed to find the relationship between the incident beam angle and lateral displacement of the beam in the focal plane. The paraxial ray tracing equations, equations (2.8) and (2.9), are used to characterise the behaviour of the trapeze. The trapeze is then described by equation (3.1),

$$x = F_L \theta_0 \tag{3.1}$$

where θ_0 is the angle between the optical axis and the beam reflected by the galvanometer (in radians), F_L is the focal length, and x is the distance from the optical axis to the location of the beam on the focal plane. The operational range for OCT is generally only a few degrees and so the requirement of paraxial ray tracing for use in the small angle approximation regime holds. One lens is used to focus the beam onto the sample and so only a single iteration of the ray tracing equations is required. To yield diffraction limited operation, the galvanometer angular movements must change the beam location less than the spatial resolution. A general rule of thumb for selecting the sampling frequency is to sample at half the Rayleigh Criterion [43]. If the spatial resolution is approximately 5 μm, 2.5 μm movements are necessary and smaller movements are desirable to give fine control over positioning. Using equation (3.1) with $F_L = 100$ mm the angular change necessary in the galvanometer to provide a 2.5 μm movement is $\theta_0 = 1.4$ mdeg (optical). A 1 ° mechanical change is equivalent to a 2 ° optical change in the galvanometer and 1 V induces a 1 ° mechanical movement. 1.4 mdeg optical is 0.72 mdeg mechanical and as such, 0.72 mV steps are necessary to provide the necessary movement. To provide a clear and easy reference, each mm spot movement across the sample, is generated by a 0.29 ° mechanical movement.

It is important to note that the values for Rayleigh Criterion are presented here for use in air, where the index of refraction is 1. When the light beam enters a sample with a different index of refraction, the Rayleigh Criterion is scaled by a factor of 1/n. Brooksby et al. use values between 1.3–1.6 for the index of refraction of tissue and so the Rayleigh Criterion will suggest slightly smaller step sizes.

The DAQ provides an analogue voltage signal to the galvanometer and discretises the voltage over 16 bits. The galvanometer is driven by +/-10 V (20 V total) and so the smallest voltage that can be generated is 20 V / 16 bits = 0.31 mV. Since we require 0.72 mV increments and the DAQ is able to generate 0.31 mV changes, the hardware is suitable. Nyquist rate imaging requires sampling at twice the spatial frequency of the object of interest in order to represent the feature digitally [35].

The trapeze can accommodate samples that are larger than can be actually be scanned. There is a physical space of 6 cm x 6 cm on the sample platter; however, the usable scan size is much smaller. The translation stage has a stroke of 5 cm and so the amount of sample in the along-track direction that can be scanned is 5 cm. The Nanomotion stage can generate step movements as small as 50 nm, but typical OCT uses steps that are a few μm's in size. Guidance for selecting a step size in the along-track direction can be found by matching to the galvanometer step size, thus providing even sampling. For Nyquist level sampling, the stage step size should be 2.5 μm, half of the Rayleigh Criterion.

3.3 Optical analysis

The use of a hybrid galvanometer-stage design versus a two-galvanometer or two-stage design allows the handling system the beneficial elements of each with few drawbacks. Galvanometers tend to be faster than stages, but perform best over small angular ranges. Both the Thor Labs and Nutfield galvanometers have angular excursions of +/- 10 ° (mechanical) which would allow for a beam deflection at the sample of 69.8 mm. However, spherical aberrations from using the periphery of a lens limit the system to a smaller scan range. To avoid aberrations, a much larger lens could be used such that the beam is always within the low-aberration zone of the lens. However, spatial resolution becomes a factor at that point. Spatial resolution is directly proportional to the effective aperture of the lens; that is, how much of the lens is illuminated. As such, lens selection becomes a trade-off: a smaller diameter lens allows for a smaller f-number and better resolution, while a larger lens allows for fewer aberrations during off-axis scanning and better depth of focus.

An analysis of the optical aberrations was performed using a simple model in ZEMAX. The model was built around data for the trapeze focusing lens, which was obtained from the manufacturer's website. The model starts with a collimated beam moving through the lens and coming to a focus. The incident angle of the beam is manipulated to simulate the effect of the galvanometer moving. The model is illustrated in Figure 3.7. The tilt is performed around a surface 5.9 cm away from the lens, where the galvanometer acts in the physical system to tilt the beam. The system is optimised using ZEMAX merit functions which specify that the smallest root mean squared (RMS) error from the spot centroid is desired. Data was collected for angles increasing from the optical axis by 0.25 °. The primary goal of performing the analysis is to determine what aberrations are present as the beam moves off-axis through the focusing lens. A performance envelope based on limiting the aberrations will ensure ideal imaging conditions.

The ZEMAX "Geometric Image Analysis" is presented in Figure 3.8 and shows focussed spot for a selection of angles ranging from 0–3 °. The images are plotted as a view of the image plane and black represents areas that the beam is present. The images are 0.1 mm in width. There is a clear trend that the spot broadens for off-axis transmissions.

The FWHM was calculated for a selection of transmission angles from 0–3 ° and is plotted in Figure 3.9. The FWHM was calculated by vertically binning the data from the Geometric Image Analysis and then calculating the width of the signal at half the maximum intensity. The plot shows a clear elbow where the FWHM grows exponentially and the quality of the spot degrades quickly. The FWHM spot size is doubled at +/- 2 °. Although there is no firm limit concerning when a spot has too much aberration to be

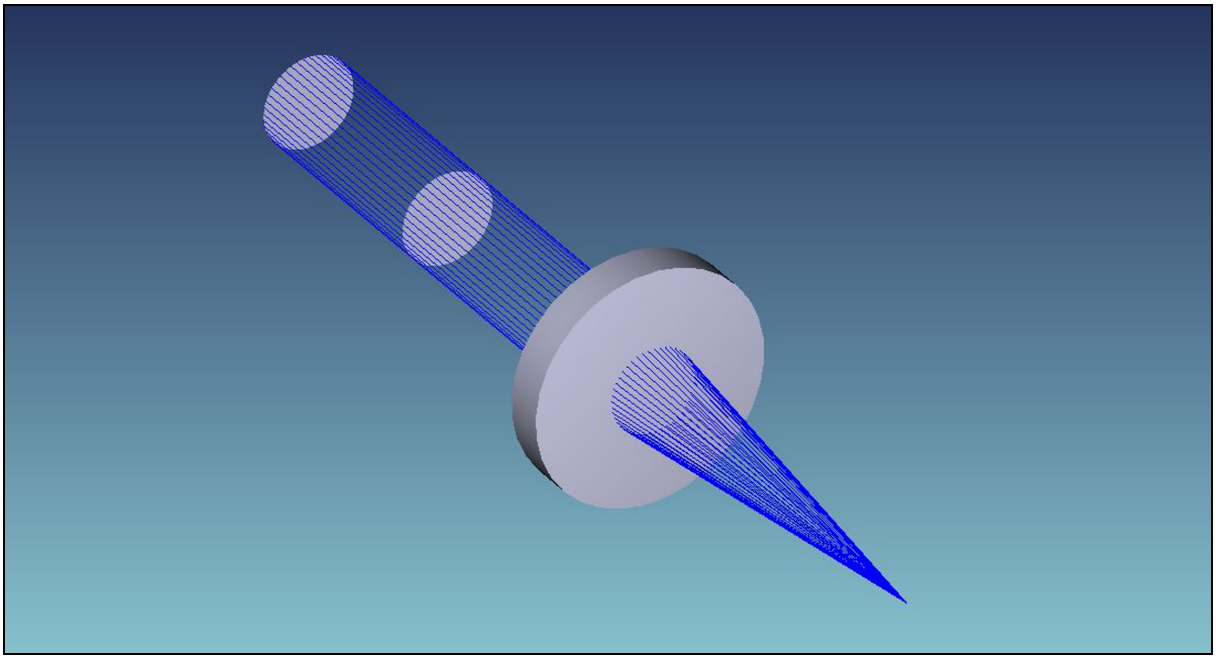

Figure 3.7: A collimated beam moves through a focusing lens in this ZEMAX model.

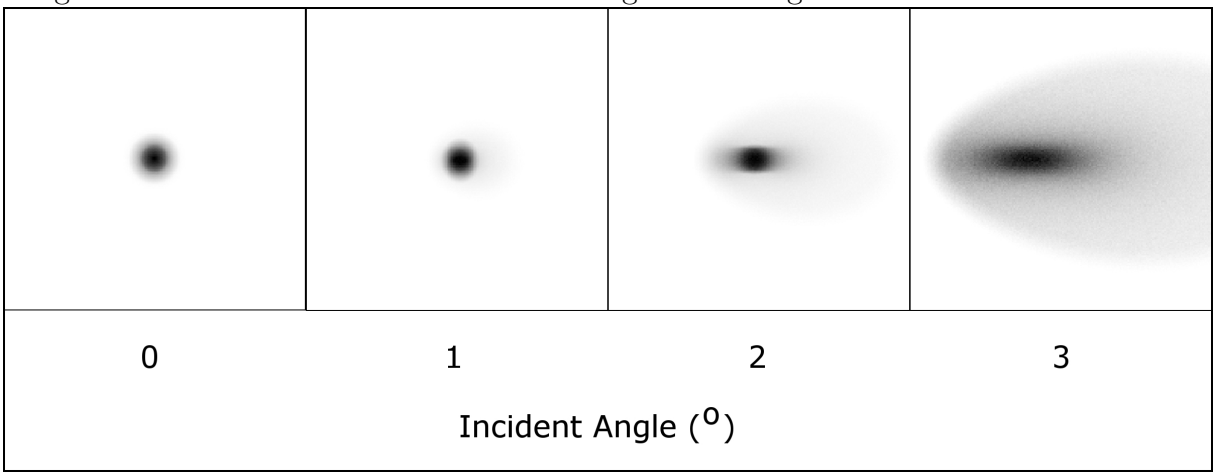

Figure 3.8: The ZEMAX Geometric Image Analysis tool allows the focal plane to be visualised and distortion of the optical spot to be seen.

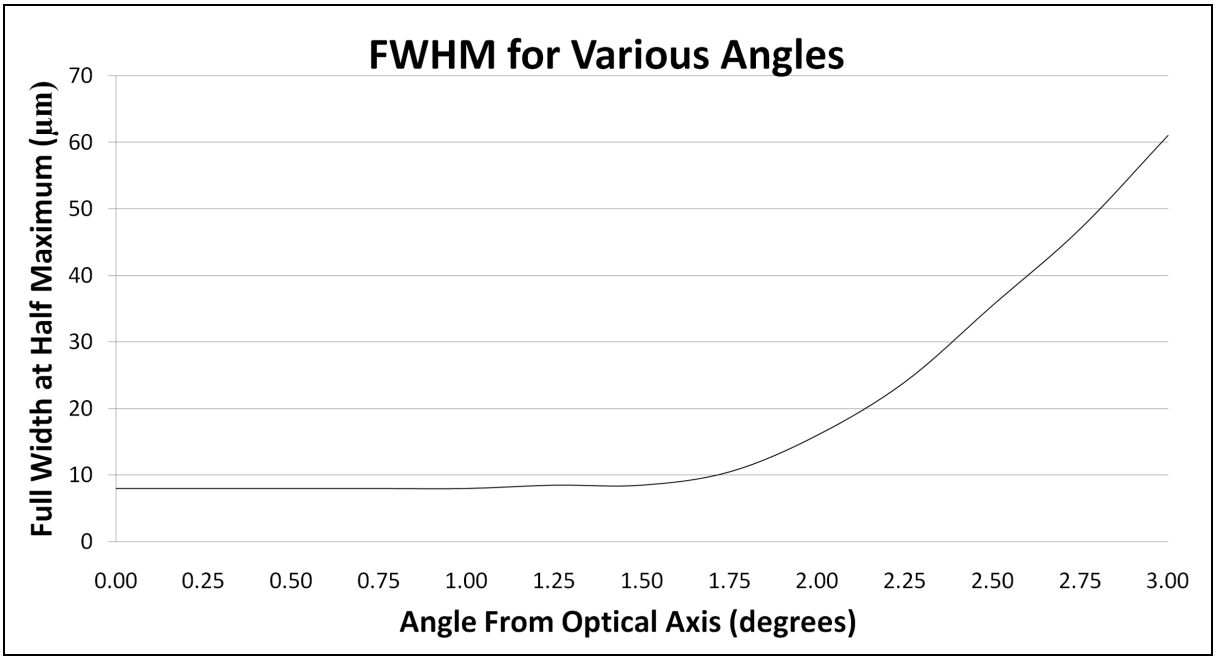

Figure 3.9: The FWHM increases dramatically above 2°. Imaging should be limited to less than this threshold.

useful, the plot shows that broadening can be limited if the beam is kept within +/-2° optical. This is +/-1° mechanical and translates to a transverse displacement of 3.49 mm. For tighter tolerances on spot size, below 1.5° yields almost no change to spot size.

Another consideration for lens selection is the depth of focus. In general, higher depth of focus is inversely proportional to the resultant spot size; that is, a high depth of focus gives a larger spot size, while a low depth of focus gives a smaller spot. If the imaging system is designed for better depth penetration, a higher depth of focus is necessary and poorer spot performance is expected. The depth of focus is calculated using equation (2.5) and is 40 μm (for λ = 850 nm, F = 5). The depth of focus can be further evaluated in ZEMAX. A simulation is able to provide a view of the effect on the spot if the focal plane were to move up or down, as illustrated in Figure 3.10. The simulation shows three wavelengths to give insight into the OCT bandpass. The three wavelengths shown are the minimum wavelength (800 nm) at top, centre wavelength (850 nm) in middle, and maximum wavelength (900 nm) at bottom. The data are shown for both the on axis case and for the +/- 2° limiting case. The plots in Figure 3.10 show the importance of placing

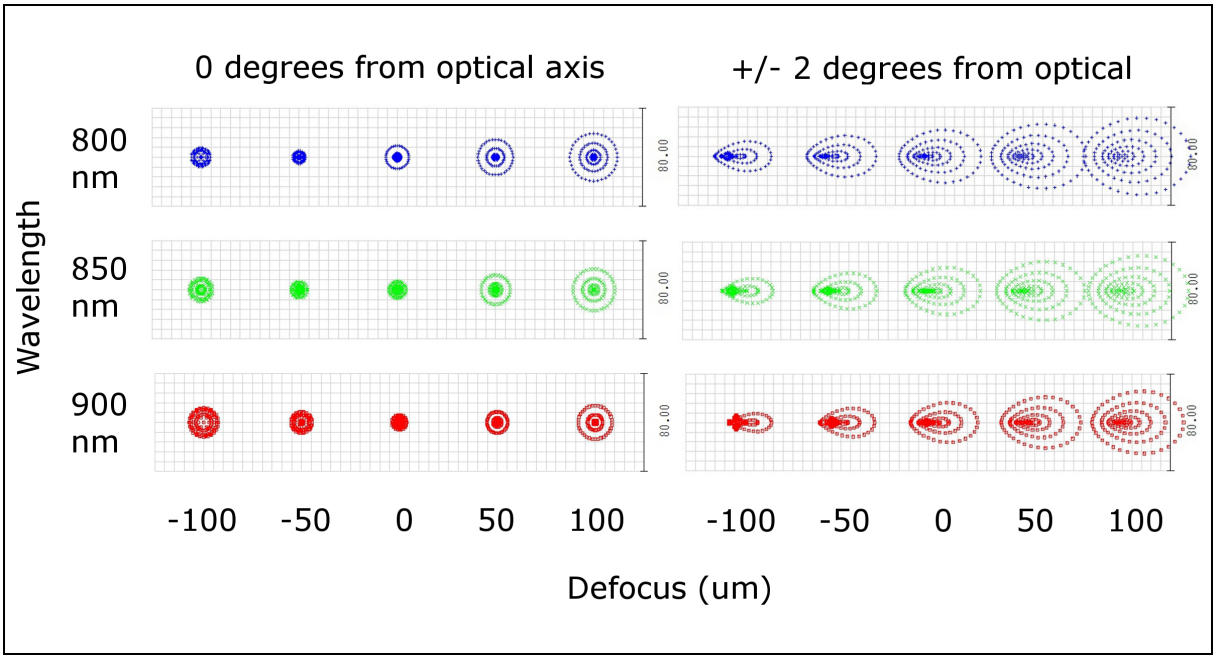

Figure 3.10: The spot changes considerably when the sample is not placed at the focus. The data are shown for three wavelengths: 800 nm at bottom, 850 nm in middle, and 900 nm at top. The spot scale line is 80 μm.

the sample at the focus. For the 0 ° case, the beam has not yet come to focus in the -100 μm case and has already started to diverge in the +100 μm case. This is contrary to the 2 ° case where the spot size is actually smaller and better contained at -100 μm.

3.3.1 Alignment and degree of freedom concerns

A key requirement of the trapeze design is flexibility. A system that offers ample adjustability allows for a range of beam inputs, but must be designed with great care to avoid too many degrees of freedom. Each additional degree of freedom adds to the complexity of alignment and makes it difficult to maximize the light coming through the system. This is best illustrated by analysis of the Thor Labs based trapeze versus the Nutfield based trapeze. The Nutfield based system reduces the degrees of freedom in order to ease alignment constraints. Although the degrees of freedom are reduced, the Nutfield trapeze still meets the requirements of a flexible system. Table 3.1 illustrates each adjustable

component and describes the concerns. The table references the drawing in Figure 3.11.

In addition to the degrees of freedom described in Table 3.1, there is some flexibility any time a screw is used. A standard through-hole allows for a small amount of "give" during tightening in order to allow adjustment if there is imprecision during machining. This aids in ensuring coupled components will fit, but allows small shifts in final position. Provided at least one kinematic mount is present in the dog-leg, these shifts are inconsequential. If tighter tolerances are required, there are several solutions to aid in coupling components. Flanges may be added so that the components fit in only one orientation and can be machined with tighter tolerances. Another possible solution is to use dowel pins. These are pins that are machined with higher tolerance than screw holes in one or more locations. Dowel pins are inserted into each of the coupled components and then the screws are tightened.

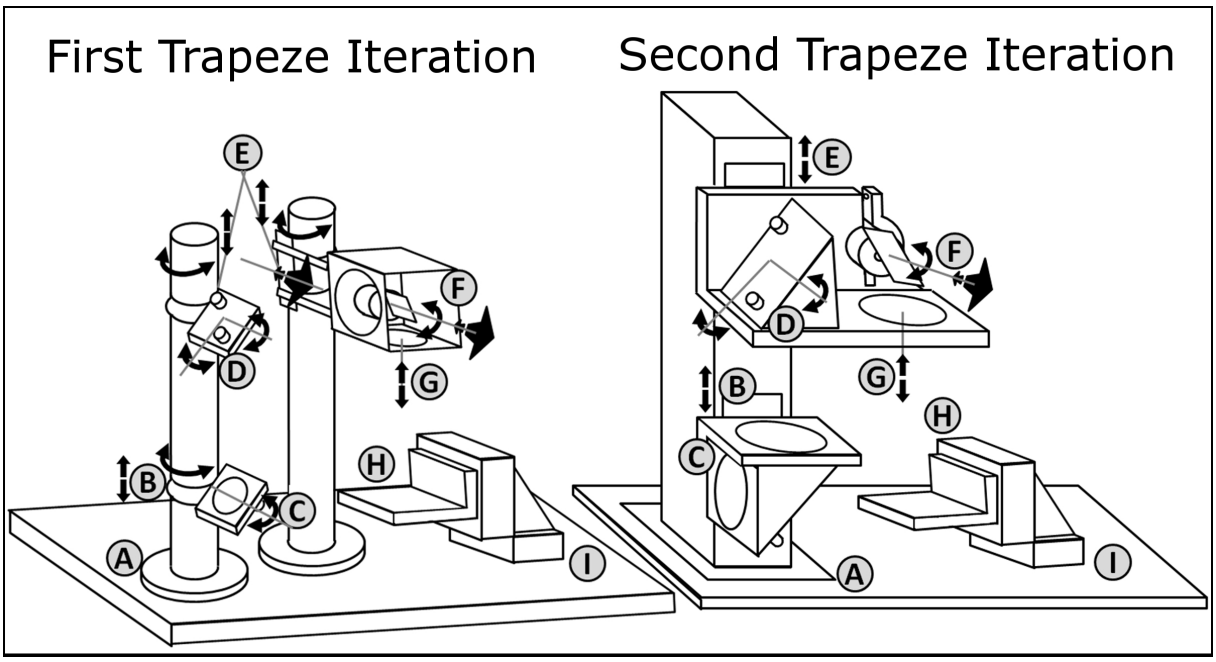

Figure 3.11: There are fewer degrees of freedom in the second trapeze iteration than the first trapeze iteration. The labelled parts refer to Table 3.1 where additional details can be found about adjustability of various components.

Table 3.1: The degrees of freedom are reduced from the first iteration to the second iteration of the trapeze.

Interface	**Cartoon item**	**TLG (# of deg. of freedom)**	**NTG (# of deg. of freedom)**	**Discussion**
Mounting post to table adapter	A	0	0	The post is fixed firmly to the table and is the first piece to mount. The post is mounted vertically and aside from this, there are no orientation concerns (no front and back differentiators) when nothing else is mounted.
Mounting posts to post adapter	B	2	1	Both systems allow up/down positioning, but the Thor Labs based system also allows rotation of each dog-leg and galvanometer mount. Rotation is constrained by using a square post in the Nutfield-based system.
Post adapter to kinematic mount	C	1	0	The kinematic mount is attached to the post adapter by only one screw in the Thor Labs system and allows rotation. The Nutfield system uses two screws which restricts that rotation.
Kinematic dog-leg mounts	D	2	2	Each kinematic mount allows adjustment for tip and tilt of the beam. This is necessary to adjust for slight offsets to the entrance angle of the input beam.

Upper dog-leg, galvanometer, and focusing lens mount(s)	E	5	0	The Thor Labs based trapeze includes independent adjustment of the upper dog-leg and the galvanometer (including the focusing lens). By coupling them together in a larger mount, the Nutfield system provides easier alignment of the galvanometer with the dog-leg. Once aligned, if the upper elements need adjustment, they move together. The Thor Labs galvanometer mount may be moved in/out, up/down, and around the post.
Galvanometer mount	F	2	2	The galvanometer may be rotated in its mount and pushed in or out of the cylindrical hole. The galvanometer should be mounted so that the mirror is 45 ° to the incoming beam and it will direct the beam down. By pushing the galvanometer in as far as possible, that adjustment can be restricted and the number of degrees of freedom in both cases can drop to 1.
focusing lens mount	G	1	1	Both systems mount the lens in a lens tube. As such, it can be rotated and moved in/out. The lens is axis-symmetric, so only the in/out matters. The distance between the galvanometer and lens does not matter since the beam is collimated. The distance between the lens and the sample determines where the sample will be with respect to the focus.

Manual focus stage	H	1	1	The manual focus stage provides up/down adjustment so that the sample may be placed at a desired position with respect to the focal plane. The manual focus stage is secured via an L-bracket to the Nanomotion linear stage with eight screws. The stage bearings are therefore fixed, allowing only up/down movement.
Nanomotion stage to table	I	0	0	The stage is secured to an adapter plate with four screws and the adapter plate is secured to the table with four screws. Positioning of the Nanomotion stage is restricted to the spacing of the holes on the optical table.

In the dog-leg, the use of two kinematic mounts allows for correction to both shear and tilt of an entrance beam and so the necessity of both is directly related to the nature of the entrance beam. If the entrance beam were provided with no tilt or no shear, one of the kinematic mounts could be removed. If another generation of trapeze were to be constructed, minor changes are possible to further simplify the system. A custom mount for the lens beneath the galvanometer would reduce some of the distance between the galvanometer and the lens, reducing the path length for both the sample and reference arms of the interferometer. A shorter path length means the system is more compact. Finally, once the incoming beam height and the focusing lens focal length are no longer in design flux, the platforms may be permanently secured to the mounting post. They are currently on sliders and each time they are adjusted, there is an associated adjustment necessary in the reference arm to keep the path length equidistant.

3.4 Performance Optimisation

In order to optimise the performance of the trapeze, the electronic components were analysed and compared with alternative technology. In the following analysis the Thor Labs

and Nutfield galvanometers are compared with an additional galvanometer from Cambridge technologies. In addition, the Nanomotion linear stage is compared to a stage from Nippon Pulse, both using the same generation of Galil controller. Finally, data were collected during operational scans using the current OCT system to determine if there are any optimisations possible in the scan algorithm. The linear stages are operated from the Galil-Tools software, which includes an internal oscilloscope suitable for measuring timing and performance values. The inputs, outputs, and operating values are collected in the Galil DMC4010 and can be exported to file. The galvanometer controllers include diagnostic panels for acquisition of position and noise information.

3.4.1 Galvanometer analysis

The Thor Labs GVS001, Nutfield QuantumScan-30, and Cambridge 6240HA galvanometers are analysed in the following section. Each galvanometer operates from an analogue +/- 10 V signal to generate +/- 10 ° mechanical movement. The diagnostics available from the galvanometer diagnostic panels are illustrated in Table 3.2.

The Cambridge galvanometer (CG) is driven by a Micromax 671 Series amplifier and uses two coupled power supplies (Mean Well, SP-200-24) to give differential outputs. The CG mirror is the same size as the NTG mirror and is able to accommodate beams of 25 mm. An external oscilloscope is used to collect the data from the galvanometer diagnostic ports and the rows in table 3.2 describe the type of data able to be collected and the port to use for the each of the three galvanometers. Additionally, some of the outputs are scaled or inverted with respect to the input command signal and so this information is included in table 3.3. The plots to follow are corrected for the inversions and have been scaled so that the data are directly comparable. The important diagnostic outputs to evaluate galvanometer suitability are the position output, slew rate command, and ground. The position output is a velocity signal that corresponds to the position read by the galvanometer position encoder. The slew rate command is a smoothing of the input command to prevent any large mirror position jumps that can potentially damage the system. The slew rated output is the actual command signal that the galvanometer mirror is driven with rather than direct drive from the analogue DAQ voltage. The slew rate command is not available for the CG system, so all plots to follow for the CG system use the DAQ input command rather than slew rate.

All of the following tests were performed after the electronic systems had been given a warm-up period and reached steady state operation. The galvanometers were all in factory-tuned state and no in-house modifications were performed.

Table 3.2: Each galvanometer drive amplifier includes a diagnostics panel

Pin	Thor Labs (panel J7)	Nutfield (panel J12)	Cambridge (panel J4)
1	Position Output	Position Output	Velocity Output
2	Slew Rate Command	Position Error	Position Output
3	Position Error	AGC Monitor	Ground
4	Current Monitor	Velocity Output	Error Output
5	Motor Mute	Ground	Current Monitor
6	Test Input	Slew Rate Command	90% Max Power Flag
7	Motor + Coil Voltage	Current Monitor	Fault Output
8	Ground	N/A	Remote Shutdown

Table 3.3: The scaling and orientation of the galvanometer diagnostic signals

	Nutfield		Thor Labs		Cambridge	
	Phase	**Scale**	**Phase**	**Scale**	**Phase**	**Scale**
Input	In-phase	1 x	In-phase	1 x	In-phase	1 x
Position output	Inverted	1/2 x	In-phase	1/2 x	In-phase	1 x
Slew rate	In-phase	1/2 x	inverted	1/2 x	not available	1 x

The National Instruments DAQ provides up to two analogue outputs in addition to many digital input/output ports. The DAQ provides analogue outputs for +/- 10 V, discretised over 16 bits. As such, the smallest voltage possible is 0.305 mV. The DAQ has specifications of less than 2 mV noise, but examination of output signals in a variety of lab settings shows that the room's ambient noise makes a significant difference. Figure 3.12 shows a stepped voltage moving at the smallest increment the specifications allow for, 0.305 mV. The calculated RMS error is 0.71 mV. There is a clear upward trend to the data, but for voltages as small as 0.305 mV, the noise dominates the signal. Placing the residuals in a histogram allows for further investigation into the nature of the noise, as illustrated in Figure 3.13.

The histogram is separated into bins 0.2 mV in size. For better visualisation, data were restricted to those points falling within +/- 3 mV and outliers above this are removed (0.2% of data). The spikes that occur every 50 μs are caused by a mechanism in the DAQ that resets charge as it sets the analogue output to the next value. The galvanometer driver boards feature filtering circuits to minimize galvanometer movements due to short timescale spikes and signal noise.

The rise time for the DAQ is generally under 1 μs and shall be treated as negligible

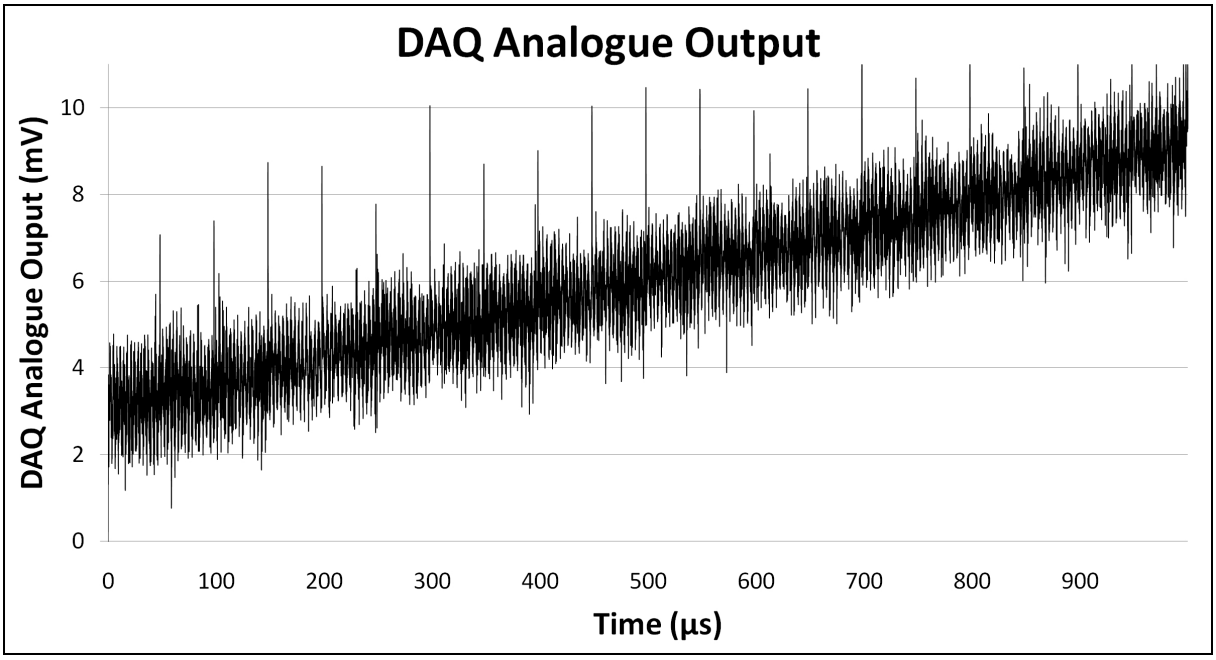

Figure 3.12: The DAQ is able to generate voltages as small as 0.3 mV, as seen in this stepped function.

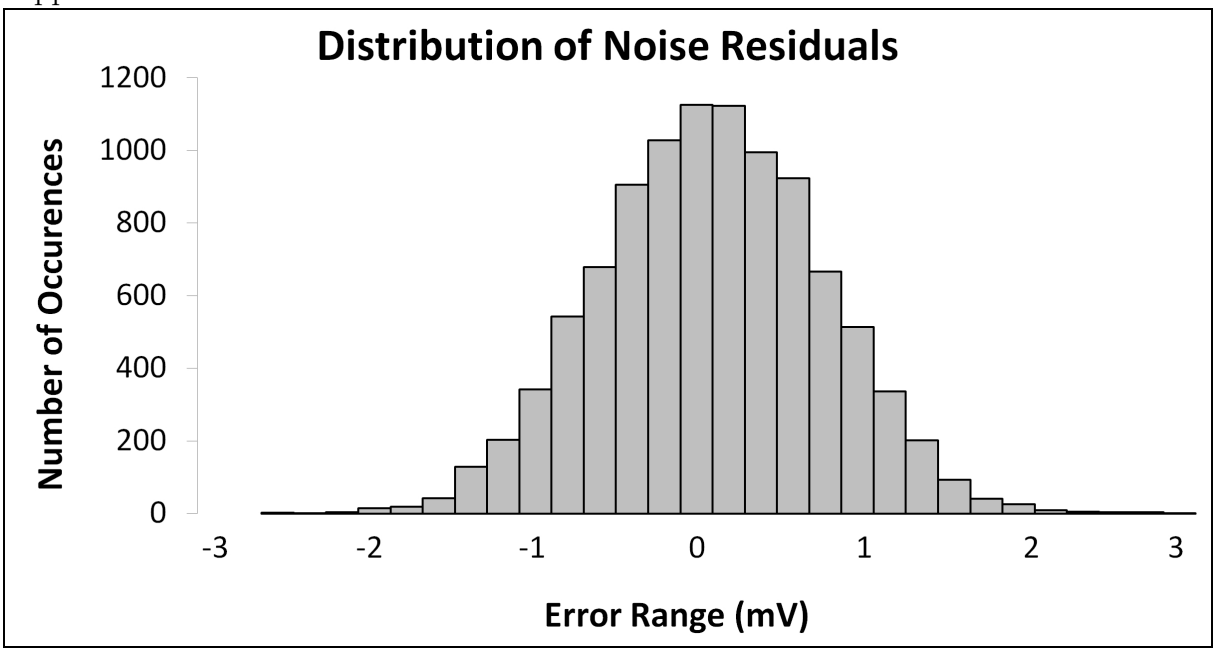

Figure 3.13: The noise in the DAQ analogue output is approximately Gaussian in shape.

in the analysis to follow. There is a slight delay between the DAQ analogue output and slew rated command signal. All three galvanometers are slew rated, but only the TLG and NTG systems allow for the slew rated command to be measured. For a 500 mV step movement, the NTG introduces a 20 μs delay and for a 10 mV step, a 10 μs delay. The TLG introduces less than 2 μs delay between the input command and the slew rated for both the 500 mV and 10 mV commands. As such, for the following measurements a delay factor should be introduced whenever the slew rate command for the NTG and TLG are compared with the CG since the Cambridge system does not include a slew rate command output.

A stepped triangle wave was input into each of the galvanometers. The wave was generated in 20 mV steps to examine the system response during decreasing timescales. Reliable galvanometer operation is illustrated in Figure 3.14(A)-(C). The limiting cases where the galvanometers are no longer able to respond to the stepped movements due to shortness of timescales are illustrated in Figure 3.15(D)-(F). The upper, grey lines in the plots are the slew rate commands (SR) (the DAQ input in the Cambridge case, IN) and the lower, black lines are the positions of the mirrors (PO), as output by the diagnostic panels. For a 20 mV step, the Nutfield system has a reliable step pattern until approximately 800 μs per step, the CG system approximately 800 us, and the TLG system approximately 250 us. The TLG system has better performance here because of the smaller mirror. With a smaller mirror, there is less inertia, and the mirror takes less time to move.

The step response for each galvanometer may also be examined. The plots are illustrated in Figure 3.16 for large (0.5 V), and Figure 3.17 medium size (10 mV) steps. The important characteristics investigated here are the shape of the step response and the time over which the responses occur. The magnitude of the voltage jumps are correct in the following plots, but they have been offset up or down for increased clarity.

A 500 mV step response means that the galvanometer was driven from zero to 500 mV (0.5 $^\circ$ mechanical) over a spacing of 1.7 mm across the sample. A 10 mV step drives the beam 0.035 mm across the sample. Analysis of the position output for each galvanometer is in Table 3.4. In order to fairly compare the CG system with the NTG system, 20 μs should be added to the 0.5 V values in Table 3.4 and 10 μs should be added to the NTG values for 10 mV. The TLG values for both 0.5 V and 10 mV should have 2 μs added for comparing to the CG. During a larger scan like 0.5 V, the TLG responds quicker than the CG and NTG systems. During small movement scans like 10 mV, the systems operate similarly with the TLG having slight benefit. The three galvanometers were also tested with a 1 mV step signal, as illustrated in Figure 3.18. For a 1 mV scan, the RMS error is a key factor in determining the galvanometer performance envelope. The lowest RMS error is found in the NTG, 0.36 mV. The TLG is next at 1.27 mV, followed by the CG at 2.3

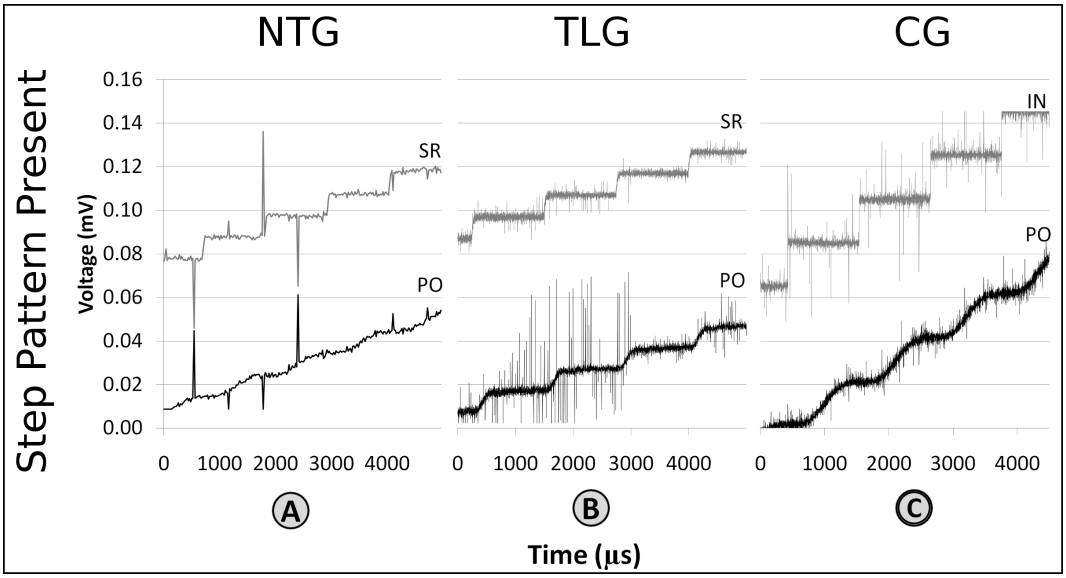

Figure 3.14: The step pattern is clearly visible in this step and hold pattern.

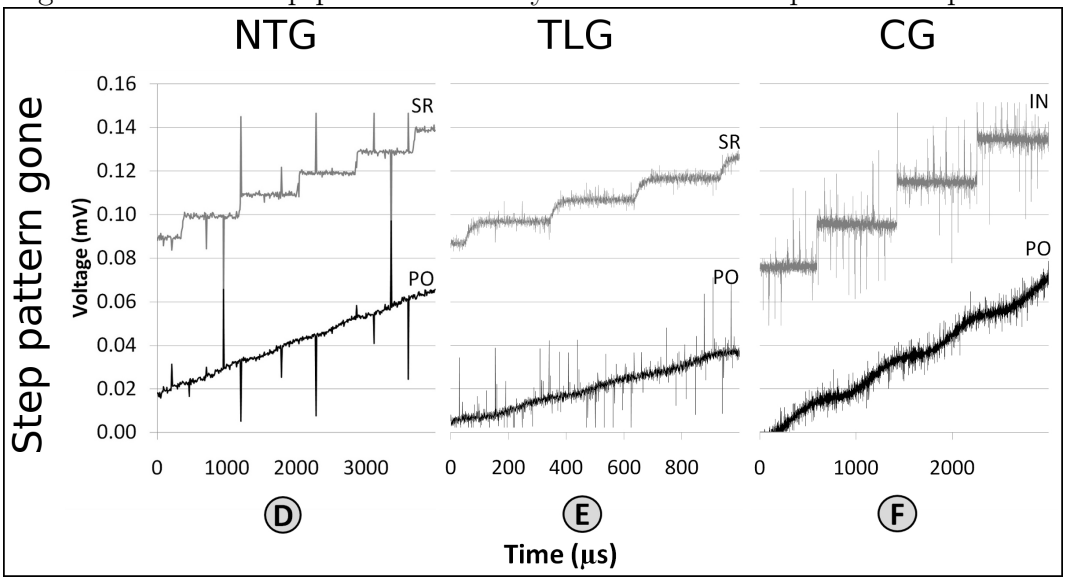

Figure 3.15: The step pattern has disappeared when the timescale decreases sufficiently.

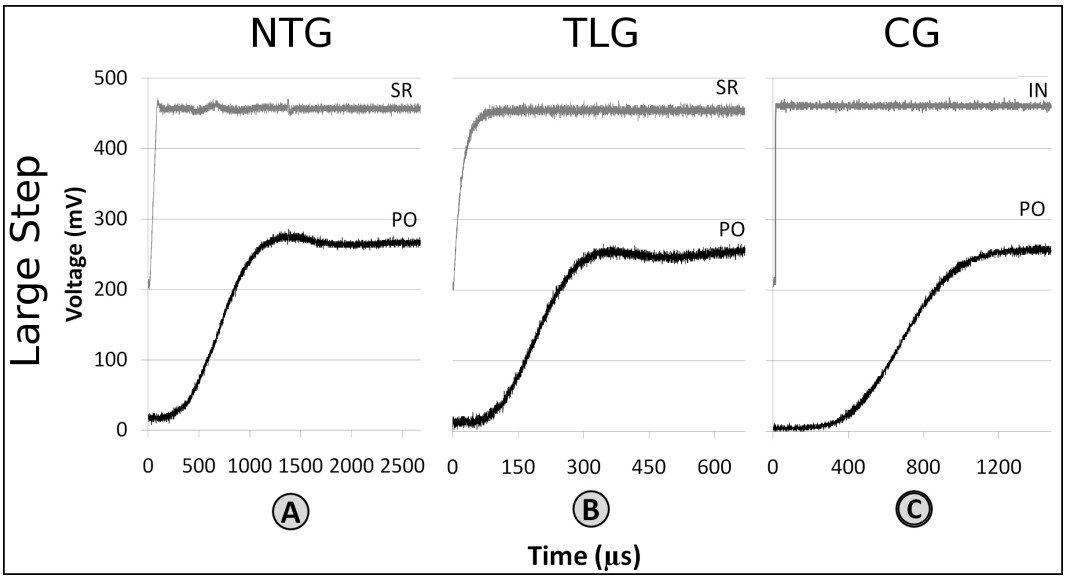

Figure 3.16: The (A) through (C) galvanometer plots show the step response for a 500 mV step size. The upper line represents the commanded position and the lower line in each plot represents the position of the mirror as reported by the diagnostic panel.

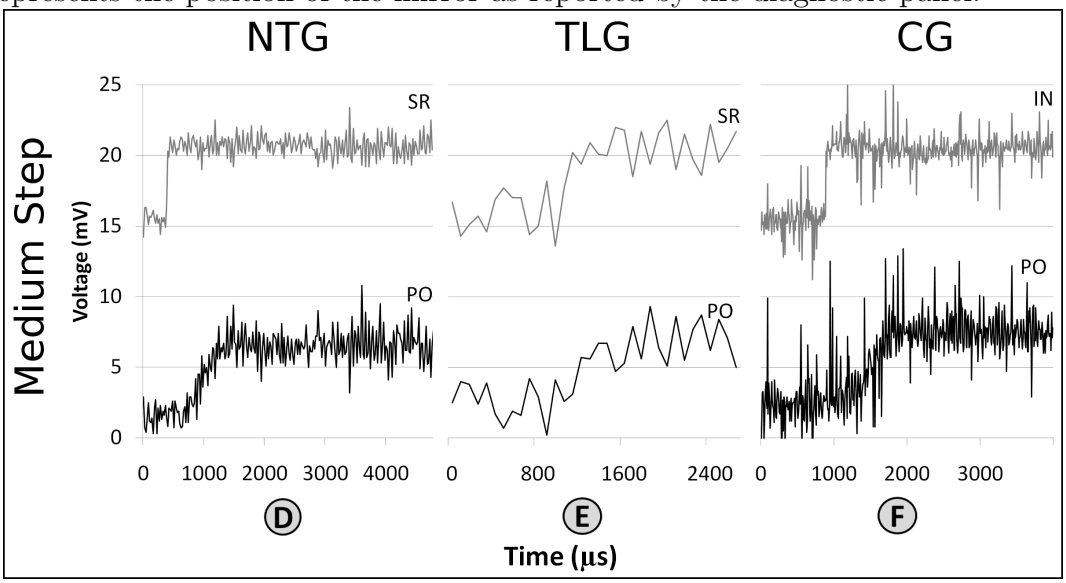

Figure 3.17: The (D) through (F) galvanometer plots show the step response for a 10 mV step size. The upper line represents the commanded position and the lower line in each plot represents the position of the mirror as reported by the diagnostic panel.

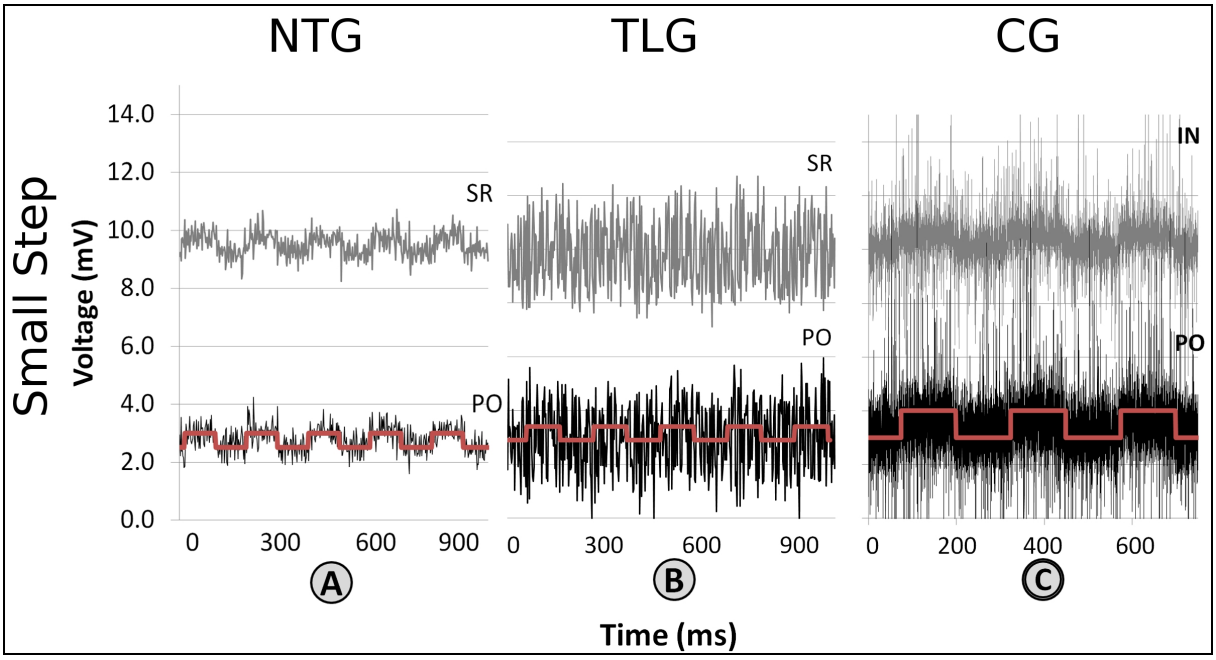

Figure 3.18: When the step size becomes very small, 1 mV, or less, it is difficult to differentiate the phases of the galvanometer position outputs. The top line is the commanded signal, the bottom is the position output and the over-plotted square wave shows the theoretical command signal that was sent to the system.

mV. When using these low voltage levels, typical of the size OCT requires, the low RMS error of the Nutfield galvanometer, makes it the preferred system.

3.5 Stage Analysis

A Nanomotion FB050 system with an HR4 motor and a Nippon Pulse SCR075-50 stage with a S080T motor were selected for testing. Both systems have 5 cm stroke and use 10 nm Renishaw encoders. The Nanomotion uses the RGH25F series encoder and the Nippon Pulse stage uses the Tonic series encoder. Linear stages tend to oscillate around a desired value, so a rating of resolution only tells part of the story. The use of a position noise rating is a clearer way to describe stage stability [22]. Any movement increment that is smaller than the position noise, will not be reliably performed, despite the stage tending

Table 3.4: timing for each galvanometer for a step size of 500 mV and 10 mV

	NTG	**TLG**	**CG**	**NTG**	**TLG**	**CG**
Size of step [mV]	500			10		
Actuation delay [μs]	140	55	255	360	160	304
Peak Time [μs]	1232	288	1095	760	800	968
Rise Time [μs]	964	246	917	520	320	896
Settling Time [μs]	1399	475	1095	1040	1040	1032
% Overshoot [%]	8	6	4	76	56	80

towards that location. The RMS error will give an initial sense of the stage position noise and the peak to peak error will tell the remainder of the story, by illustrating the maximum position offset that may be present.

The Nanomotion motor is a piezo based system that uses high frequency vibration to move the stage. The contact point acts like a finger pushing the stage along the desired direction. The Nippon Pulse system uses a linear shaft motor that is non-contact between a permanent magnet and the forcer coils. Both stages operate on a closed loop PID feedback system and use the same Galil DMC4010 controller. The GalilTools language and software package includes an eight axis oscilloscope that tracks controller data in real time. The data for all controller variables is available for post-experiment analysis as well. The GalilTools oscilloscope samples every 8 ms and so features must occur over a larger timescale than this to be captured reliably.

The tests were performed under the assumption that the sample would be secured in place with a clip or pin. Since this system is a general purpose test bed for scanning many different types of samples and phantoms, the current design is merely a platter that the

sample is placed upon. During high acceleration or deceleration, the sample may slide on the platter if there is enough abrupt behaviour to overcome the static friction. It is important to minimize any sample movement for cases where the operator scans across an object and needs to return to a given area for an additional scan. During many scans, it is appropriate to move the stage back to a zero position after the scan. The zero point may be defined anywhere and for many imaging applications it is useful to define zero as the midsection in order to be able to move both forward (positive increment) and backward (negative increment).

The stage feedback values (K_I, K_D, K_P) were tuned for optimal performance for each of the movement types and loadings in the following tests. Tuning must be done for each application independently. Tuning is load dependent and if different weight samples are used, more or less aggressive tuning values may be necessary. All tuning was completed with a set of three 6.35 mm optical post spacers (New Focus model 9950) to simulate a sample. A system may be tuned for smoothness and stability during either still or moving sections. Often, tuning for better smoothness in one yields a slight increase to noise in the other. The trapeze takes images in a step-and-hold fashion, so stability during stillness is of highest importance.

There are some general trends that emerge that should be noted for future stage tuning. The stage should be retuned if the loading or desired performance characteristics change. There are six primary tuning values to be manipulated: FA (Feed forward acceleration), FV (feed forward velocity), K_I, K_D, K_P, and TM. FA tends to reduce error in accelerating and deceleration sections, while FV can be used to reduce the oscillation in that error. K_P helps to reduce the overall error and shorten the settling time of the system. K_D values are adjusted to provide smoother motion profiles. A higher K_D values give smoother motion, but can cause wobble or overshoot during still sections. K_I reduces overshoot during the transition between motion and stillness and also reduces settling time. K_I values are typically small compared to K_D and K_P, and K_I should be adjusted last to provide fine tuning over the performance. If the gain values are too low or too high, instability may be introduced and the system will vibrate or fail to reach the desired position in a timely manner. Tuning should be performed without an important payload mounted due to the potential for aggressive vibration and potential for the payload to fall. Speeds should match desired application speeds as close as possible because slower moving systems are easier to tune than faster systems. Faster moving systems exhibit more overshoot and require a greater degree of fine tuning the gain values.

The Nippon Pulse Linear Shaft Motor requires a setup routine to be run prior to each use. The shaft includes two poles and at least one must be found by the drive head in order for correct commutation of the motor. A pulse is sent to drive the stage to a pole and if

the stage is able to find the pole, commutation is complete. If the pole cannot be found, a higher current pulse is sent. Note, pairing the Galil DMC4010 and the Linear Shaft Motor is a new combination and standard code does not exist for this commutation. As a result, there are some situations that do not function properly during the setup phase. If the drive head is located at particular locations on the magnetic shaft, the pole cannot be found and instability occurs when movements are attempted. The ensuing instability can be avoided if the stage is centred before power-up. The Nippon Pulse stage is free moving when not in the "servo-hold" mode and so care must be taken to ensure the stage is in an ideal position before the commutation code is run. The Nanomotion stage is driven in full contact with the piezo actuators and is held in position whether the "servo-hold" is engaged or not.

3.5.1 Tuning

The following tuning routine was used to identify feedback parameters during initial setup and when changes were made to the movement routine, if necessary. A plot of the stage output (position output, PO) and the difference between the commanded position and actual position (position noise, PN) is illustrated in Figure 3.19 for both the Nanomotion and the Nippon Pulse stages after proper tuning. In addition, untuned stage plots are shown in Figure 3.20. The tuning routine moves the stage 1 mm forward and then 1 mm backward, where 1 encoder count is 10 nm distance. The movement repeats as the tuning parameters are adjusted until an optimal stability is found. The sloped sections of the plots in Figures 3.19 and 3.20 indicate movements and the flat sections indicate stillness. The final tuning values are detailed in Table 3.5.

Table 3.5: The tuning parameters for the Nanomotion and Nippon Pulse stages

Parameter	**Nanomotion**	**Nippon Pulse**
$\mathbf{K_P}$	2	130
$\mathbf{K_D}$	40	400
$\mathbf{K_I}$	0.04	14
TM	100	100
FV	0	0
FA	0	0
IL	2	2

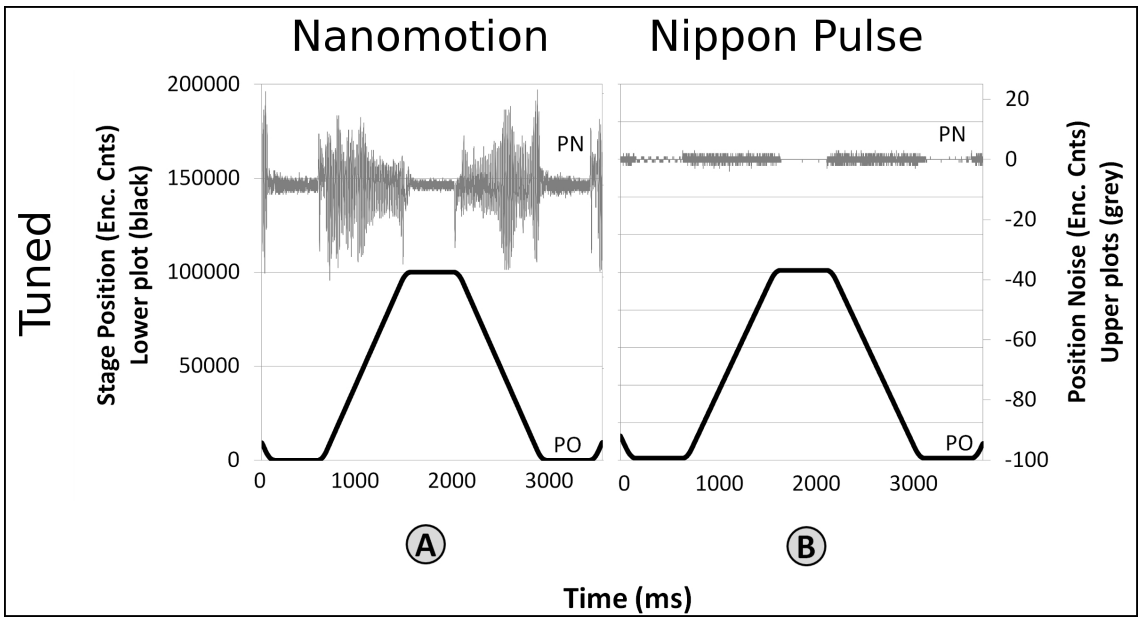

Figure 3.19: Tuning diagrams for the Nanomotion and Nippon Pulse stages. The tuned Nanomotion is shown in (A), and the tuned Nippon Pulse is shown in (B).

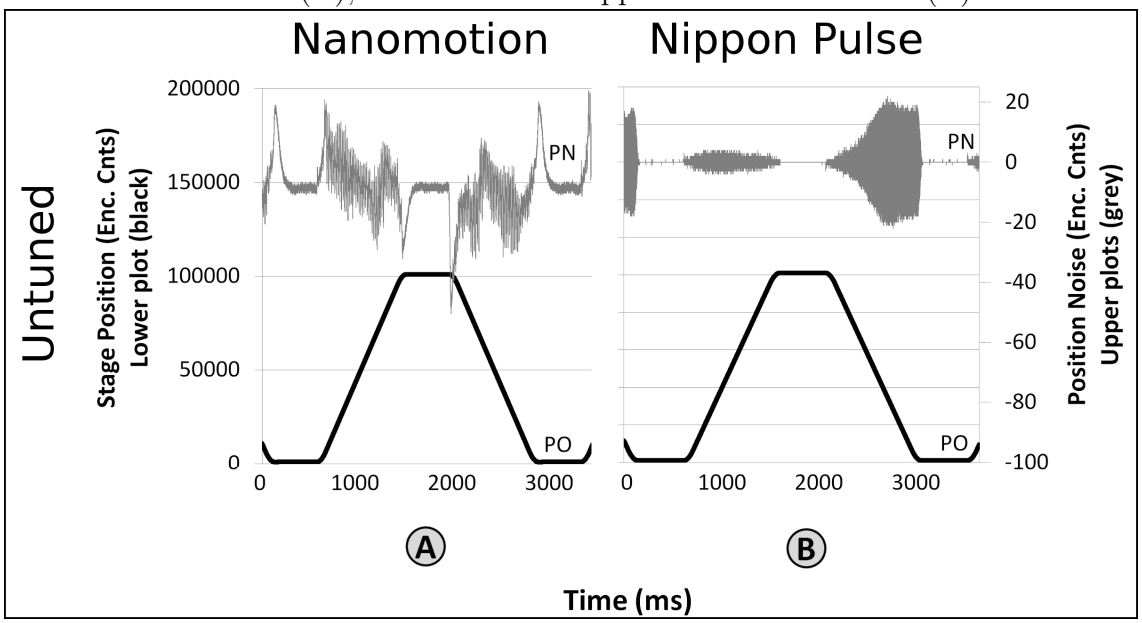

Figure 3.20: Tuning diagrams for the Nanomotion and Nippon Pulse stages. The untuned Nanomotion is shown in (A), and the untuned Nippon Pulse is shown in (B).

3.5.2 Step response

The step response for stage increments of 10 μm, 1 μm, and 0.01 μm steps are illustrated in Figures 3.21. 3.22. 3.23 respectively. The stage position (PO), and position noise (PN) are shown in the plots.

The stages are able to move as small a step size as 1 encoder count (0.01 μm). During small movements, the stages do not gain as much inertia and therefore have smaller settling times. This can clearly be seen by examining the noise plots in the above figures. In Figure 3.23 (E) and (F), the 0.01 μm step response is shown and there is limited noise compared to the plots in Figure 3.21, (A), (B) and Figure 3.22 (C), (D) which perform larger steps. It should also be noted that there is a drastic difference between the Nanomotion and Nippon Pulse stage in terms of position stability. The Nippon Pulse holds its position much better during still sections and also displays a smoother motion profile.

During the larger movements in Figure 3.21 there are small overshoots in position and the stages take longer to reach the desired positions. Scans should not be taken until the stages reach the desired positions and have stopped oscillation. The position noise (RMS and peak to peak) for each of the step responses in Figures 3.21–3.23are described in Table 3.6. The data for position noise in Table 3.6 are taken from only the still sections of the

Table 3.6: The RMS error for various step sizes, as reported by encoders

	Position Noise					
Step Size	**0.01 μm**		**1 μm**		**10 μm**	
Error	RMS (μm)	Peak to Peak (μm)	RMS (μm)	Peak to Peak (μm)	RMS (μm)	Peak to Peak (μm)
Nano-motion	0.012	0.07	0.022	0.2	0.020	0.1
Nippon Pulse	0.0014	0.02	0.0012	0.02	0.0017	0.02

motion profile since this is when images are to be taken. A typical OCT step size is a couple of μm's and so both the Nanomotion and the Nippon Pulse stages are suitable in this regard. The Nippon Pulse stage however, features much higher stability than the Nanomotion stage and does not show changes in peak to peak error for any of the three step sizes.

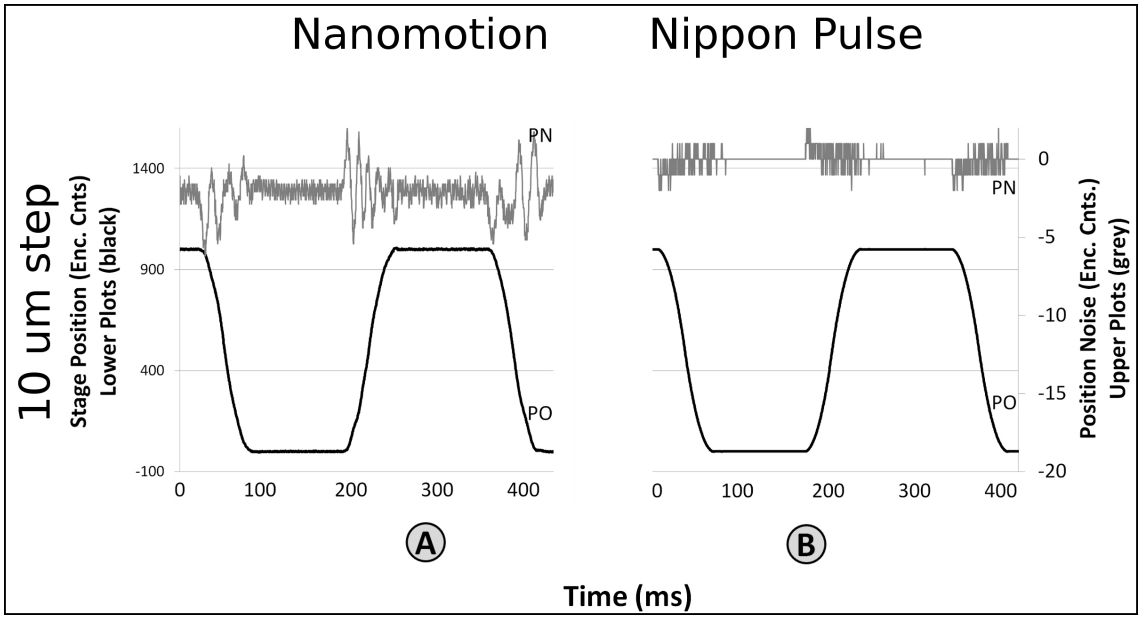

Figure 3.21: The Nanomotion and Nippon Pulse stages are able to handle a 10 μm step well.

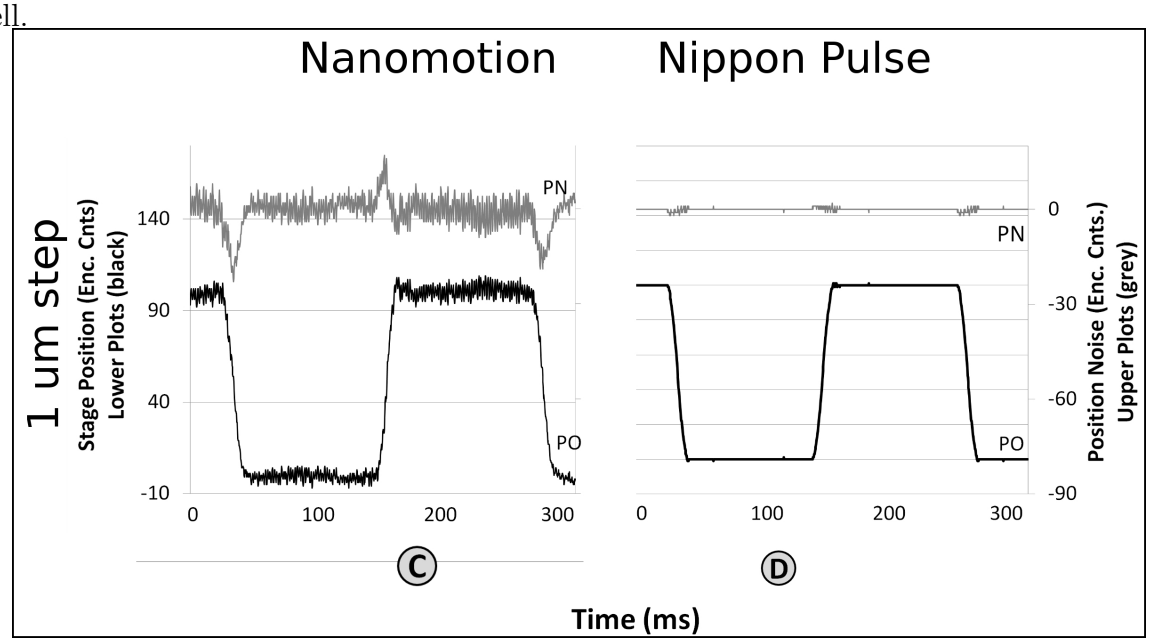

Figure 3.22: Both the Nanomotion (C) and Nippon Pulse (D) stages perform well for step sizes around 1 μm, but the Nippon Pulse begins to show its superior stability at this level.

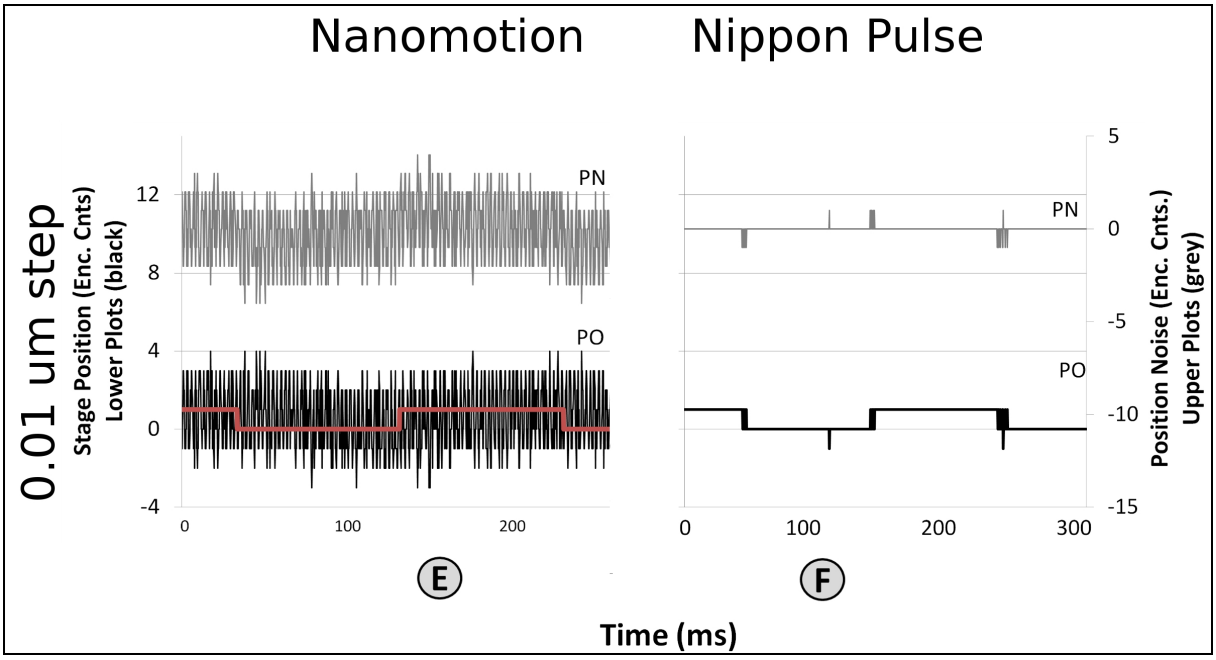

Figure 3.23: The Nippon Pulse (F) notably outperforms the Nanomotion (E) stage for small step sizes; this is a 0.01 μm step.

3.5.3 Repeatability

Repeatability of the translation stages may be measured by commanding the stages to and from a known position. Repeatability was tested for a 1 μm movement. The Nanomotion stage is specified to fall within +/- 0.05 μm, as described in Table 3.7, white the Nippon Pulse stage is specified to fall within +/- 0.01 μm. The Nippon Pulse performed better

Table 3.7: Stage repeatability measurements and specifications

Stage	**By specification [μm]**	**1 μm movement, as measured [μm]**
Nanomotion	+/- 0.05	+/- 0.07
Nippon Pulse	+/- 0.02	+/- 0.01

than specification during the test and settled to +/- 0.01 μm of a repeated value. The Nanomotion stage performed slightly outside of specification and was found to repeat within +/-7 μm of the repeated value. However, repeatability is strongly connected to

position noise. Both stages are able to move 0.01 μm increments, but suffer some oscillatory position noise. The Nanomotion repeatability rating above takes into account a settling time, while the Nippon Pulse stage does not require this adjustment.

3.6 Actual scan

Investigation of the current implementation of an OCT scan allows for identification of areas that are inefficient. There are several main components of a scan, as described in the preceding synchronisation sections. The current OCT scan system incorporates the NTG and the Nanomotion stage. The analysis is split into two figures, Figure 3.24 and Figure 3.25, due to the timescale over which a scan takes place. Figure 3.24 illustrates the behaviour of the galvanometer, the stage synchronisation pulse, and the camera exposure pulse; all the hardware commanded by the DAQ. Figure 3.25 illustrates the behaviour of the stage and the stage synchronisation pulse that commands the stage to move. The scan was performed with typical parameters: 0.3 ms exposure time, 1024 locations per B scan, a +/-0.43 V mechanical galvanometer scan range, and 100 stage movements with 3 μm per movement. The galvanometer scan range yields an across track displacement of 3 mm. These tests were performed under ideal conditions where the electronics had sufficient warm up time and no other delays were present. Occasionally, the camera capture equipment introduces additional delays as the images are stored to disk; this test neglected image storage and so these delays are not present in Figure 3.24. Here, the galvanometer position is illustrated by voltage as the mirror travels across-track to obtain a B-Scan. The sensor was set to receive one A-scan per galvanometer position and each of the 1024 B-scan locations occur over approximately 310 ms.

The sawtooth waveform illustrates that the galvanometer sweeps from one side of the sample to the other and then quickly jumps back to the initial scan location. The Camera Synch waveform illustrates that images are taken only during the forward scan across the sample. If zoomed in, the camera pulse in Figure 3.24 would reveal a square wave. One image is taken for each high logic state of the square wave. The square wave stays high during the camera exposure and then returns to a low state indicating to the galvanometer that it may increment position. When the B-scan is complete (at the end of the each saw tooth in Figure 3.24), the stage synchronisation pulse fires. The stage synchronisation pulse is kept in a high state during scans and then moves low to indicate the stage may increment forward. The high versus low logic state is only important inasmuch as the receiving device must recognise the change; the devices may be set to receive a high or low trigger. The stage synchronisation pulse is seen in both Figures 3.24 and 3.25 images

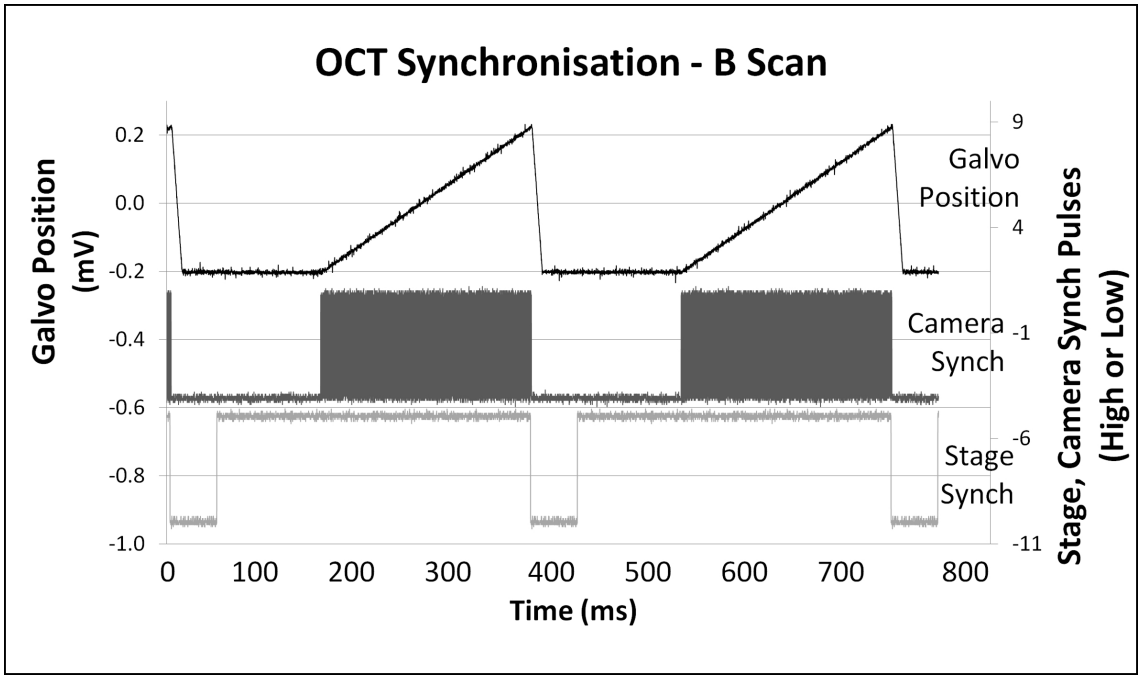

Figure 3.24: The synchronisation of an operational OCT scan.

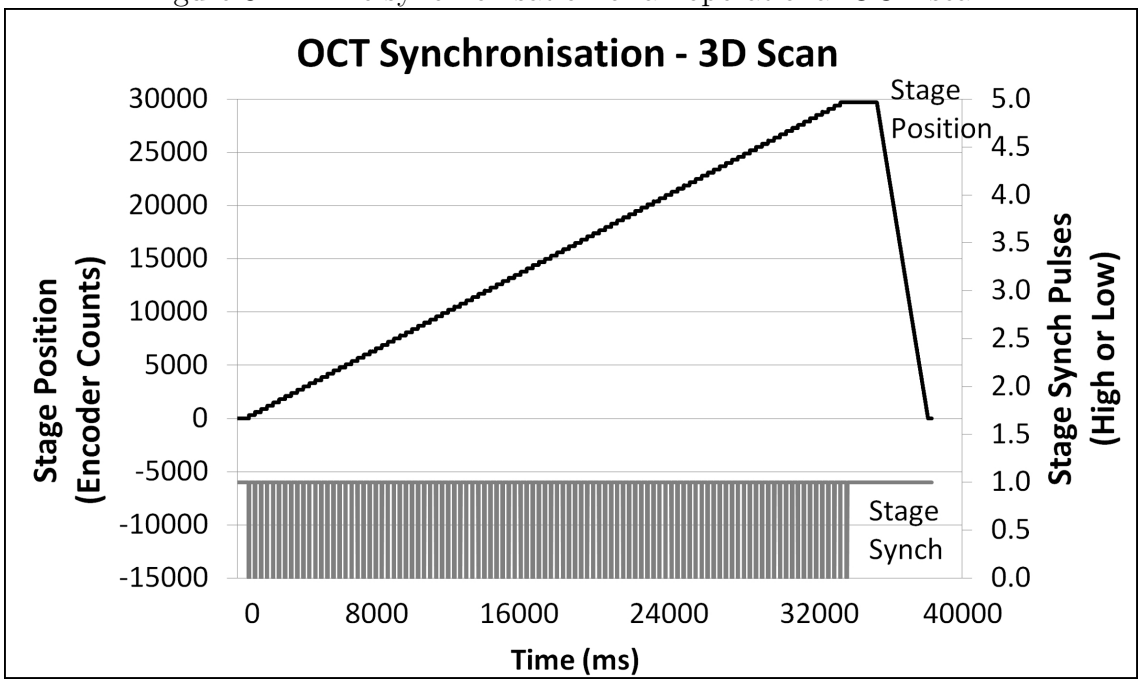

Figure 3.25: An OCT Scan captures many B-scans, each time moving the stage so that the B-scans lie parallel to each other.

to relate the two images. In Figure 3.24 two B-scans are shown and in Figure 3.25 100 B-scans are shown. The complete scan time for 100 B-scans was measured to be 39.5 s.

3.6.1 Maximum oscillation

One final test was performed using the operational OCT system. A potential limiting factor of the Nutfield galvanometer is the maximum oscillation speed of the mirror. The maximum oscillation is limited by the amount of heat that can be dissipated in the controller's heat sink. The manufacturer recommends not exceeding 1 A current draw through the system and the associated heat generated. Current may be measured via the diagnostic panel and this cut-off value is found to be reached at 57 Hz. A typical scan with an integration time of 0.3 ms and 1024 scan locations operates around 3 Hz, well below the current limitations of the galvanometer.

3.7 Results and recommendations

During initial design and development phase it is important to keep particular elements of an OCT system flexible. The ability for the trapeze to intake a beam of up to 25.4 mm in diameter and at a variable height is required, while at the same time a simple alignment procedure is needed. An iterative design process was used to allow for a prototype trapeze to mature into a more effective system. The TLG based trapeze was limited in beam size to only 5 mm and featured a cumbersome alignment routine. By coupling the upper dog-leg mirror to the galvanometer mount, alignment is much simplified. Moving from a round to square profile mounting post provides an additional reduction in degrees of freedom and an associated decrease in alignment complexity. Using the NTG allows for a 25.4 mm diameter beam, but also proves to be a more stable galvanometer over small step sizes. While many OCT systems use a two-axis galvanometer, the trapeze uses a galvanometer-stage hybrid design. Galvanometers have the capability to oscillate faster, but are limited in travel size. By using a stage instead of a second galvanometer, the travel limitations are significantly suppressed for one dimension.

The DAQ is the command centre for the OCT system. The National Instruments USB-6251 provides ample TTL outputs for synchronising other hardware elements, like the camera and stage, however, the analogue output driving the galvanometer begins to become a limiting factor during small step movements. With a 5 μm Rayleigh Criterion size, increments of half that are desired and in order to accomplish this, voltages changes on

the order of 0.715 mV are required. The DAQ is specified to be able to provide 0.305 mV increments, but the oscillatory noise begins to dominate the signal at these low levels. An analogue source with less noise and a higher bit depth would allow for more flexibility in fine control of the galvanometers. In fact, the DAQ is not a wholly necessary component. The Galil microcontroller is a required component in order to manipulate the linear translation stages, but with an added analogue output board, it would be able to command the galvanometer as well. The Galil microcontroller already includes TTL outputs that are sufficient for synchronising with external hardware. Rolling the analogue output into the microcontroller is a more cost effective solution.

Of the three galvanometers tested, the NTG system proved to perform best for low step size applications like OCT. While the TLG system tends to have lower response times, especially for larger movements, the NTG has superior noise performance. For OCT applications, galvanometer stability is a significant concern and strong performance during small step sizes is the nature of the game. The current trapeze system is broaching the minimal reliable step sizes for the package and moving to the other galvanometers would hurt performance.

Of the two linear translation stages tested, the Nippon Pulse stage is a clear winner over the Nanomotion stage. The Nippon Pulse exhibits strong position stability to within a few encoder counts during most situations while the Nanomotion stage exhibits noise in the tens of encoder counts. The trapeze uses a step-and-hold architecture for scans and so low position noise during still sections of the motion profile are most important. The RMS noise during these still sections is significantly lower, 0.0014 μm following a 0.01 μm step, for the Nippon Pulse stage than the Nanomotion stage, 0.0122 μm. It should be noted, however, that with a 5 μm Rayleigh Criterion, a good choice for stage step size is 2.5 μm. Both the Nanomotion and the Nippon Pulse stages are able to perform with low position noise for a step size of this magnitude. At a similar price point, the Nippon Pulse is a better system. The main benefit of the Nanomotion stage is that the carriage is held still, even when unpowered. If the system needs to be portable and will have samples mounted during system movement from room to room, the Nanomotion is uniquely suited to this.

To identify the trapeze performance envelope, both the optical and electronic systems need to be fully evaluated. The above comments refer largely to mechanical and electrical specifications and how they impact the trapeze. One of the most significant limitations is indeed driven by the trapeze optics. The FWHM of the optical spot increases exponentially during off-axis transmission through the focusing lens. At +/- 2 $^\circ$ optical from the optical axis, the spot size has already doubled due to spherical lens aberrations. If kept within +/- 1.52 $^\circ$ optical, aberrations are limited and have negligible effect.

An evaluation of the current scan implementation is able to help identify any areas of inefficiency. One area of considerable inefficiency during an OCT scan is the time allotted for the stage increment and mirror scan-back. The actual scan time is 37 ms, while the current algorithm leaves 146.5 ms for the movement. Initial time estimates were too conservative and the delay may be shortened to perhaps 50 ms. 50 ms allows for the scan back to occur and a short period of settling for both the galvanometer and the stage.

Finally, it is important to summarise that the trapeze provides successful 3D scanning for OCT use. The step sizes are input a-priori and the system can accommodate a large range of values. OCT inherently gives a depth profile: dimension one. The galvanometer provides across track movements: dimension two, while the stage provides along track movement: dimension three. Full 3D capability allows for better OCT imagery to be acquired and ultimately, better prognosis during clinical use.

Chapter 4

Application: Assessing Margins

When a malignant tumour has been identified and excised, it is important to determine if the full tumour has been removed. One approach in doing this is to determine if a margin of healthy tissue surrounds the excised tumour. If there is a thin layer of tissue surrounding the tumour, then it can be inferred that the tumour has wholly been removed. Additionally, limiting the amount of healthy tissue removed is important in procedures like breast conserving surgery (BCS) because it will have a direct affect on the healing time and resulting aesthetics of the excision site.

Currently, the predominant method for margin assessment during BCS is pathological examination of the tissue. The tissue is cut into thin layers, often frozen, and examined with a microscope to identify the boundary between the healthy tissue and the tumour. If a layer is found with a positive margin then the physician must take another excision from the patient. There is some debate concerning what constitutes a positive margin; some pathologists define a positive margin as a tumour broaching the surface [2, 26], while others identify positivity as the tumour coming within 2 mm of the surface [6]. It is a time consuming process to examine the excised tissue and as a result, the layers are examined post-operatively or the number of examined layers is low during intraoperative assessment, and re-excision is required in as many as 54% of BCS surgeries [2]. An automated solution that can examine a higher percentage of the tissue would allow for stronger confirmation that the growth has been removed. If the margin assessment can be done during the initial excision, the ordeal of performing multiple surgeries can be reduced.

There is a stated clinical need for real-time, non-destructive methods to assess margins; surgeons do not currently have adequate tools at their disposal [26, 6]. OCT is a modality that has potential for intraoperative use in margin assessment. OCT has lateral resolution

of a few μm and can penetrate as much as 2 mm depth. Depth is predominantly limited by absorption and scattering of the light beam. Beyond 2 mm, it is difficult to capture enough photons and the signal to noise ratio of the return beam is limited. In determining whether a margin is present, the larger the depth penetration, the better. With larger depth capabilities, the boundary between the tumour and healthy tissue can be monitored better since there is a larger window over which the boundary may be seen. All is not lost, however, if the boundary goes deeper than the imaging window; the scanner must continue monitoring until the boundary comes closer to the surface once again. If the boundary reaches the top surface of tissue, the entire tumour has not been removed and the surgeon must perform re-excision.

In order to scan the entirety of a tumour, the sample must be manipulated to allow for all positions on the surface to be probed. This presents some difficult challenges for a sample handling system. Typically, OCT uses dual galvanometers or a galvanometer-stage combination to raster scan a rectangular piece of reasonably flat tissue. Generally, the surface position does not vary significantly and only a small area is scanned. For margin assessment, as much as possible of a three-dimensional surface should be imaged.

There are clear capability requirements for a device to assess tumour margins. Brown et al. states that the sampling system for a device for assessing margins should be able to

1. take less than 20 minutes to display a result
2. provide 1–2 mm depth penetration
3. Survey as much of the surface as possible

These three requirements are the lead design considerations for the light delivery and sample handling system presented here. The prototype described here is an OCT system in which the sample arm includes a surface scan device. The surface scan mechanism is positioned after the interferometer, as illustrated in Figure 4.1.

4.1 Hardware configuration

There are unique challenges to scanning a three-dimensional surface. Accommodating complete flexibility in sample shape is difficult. For proof of concept validation, relaxations were made to this requirement and preset configurations were targeted. The system design calls for cylindrical shaped samples of a size large enough to be fixed to a rotational shaft

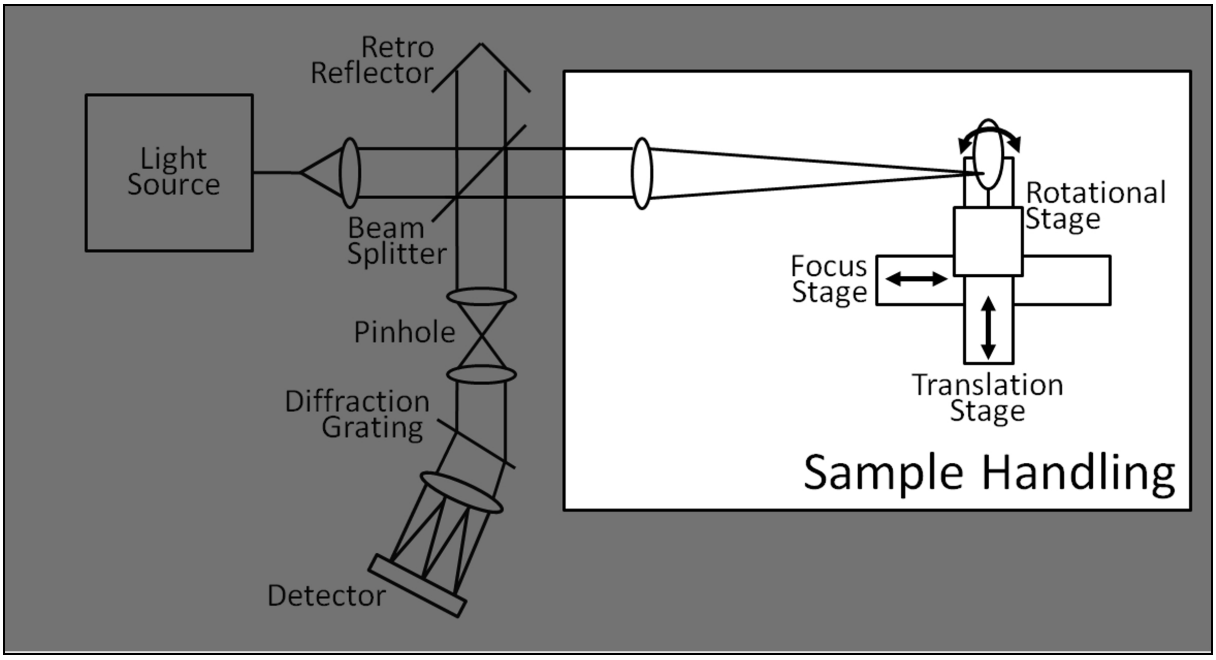

Figure 4.1: The sample handler follows the beam splitter in the OCT interferometer. Light penetrates the excised tissue and detects the presence of healthy margin of tissue surrounding the tumorous tissue.

using a skewer. Many sizes of skewer can be made, so ultimately the system is scalable. An Applied Motion rotational stage is used to provide the ability to scan around the circumference of the sample. More precisely, the sample is fixed to the rotational stage and rotated as an incident beam hits the surface. A Thompson linear stage driven by a stepper motor is used to move the sample rotation location. After each rotation, the stage moves to the next position thereby allow an entire cylindrical sample to be scanned. An achromatic lens (F_L = 250 mm, ϕ = 50.4 mm) focusses the beam onto the sample. The scan pattern is illustrated in the drawing of Figure 4.2. An additional stage is used to accommodate a variety of cylindrical sample sizes. Before the scan, the surface of the sample is moved into the focal plane of the focusing lens. OCT has the capability to probe depths of up to 2 mm [9]. Detecting a margin between healthy tissue and tumorous tissue must have as large as possible depth scan inside the tissue. Using an ideal cylindrical sample, the system can be positioned with the focus at the surface of the tissue and as a perfect cylinder, the margin will remain in the scan window at all times. However, if the

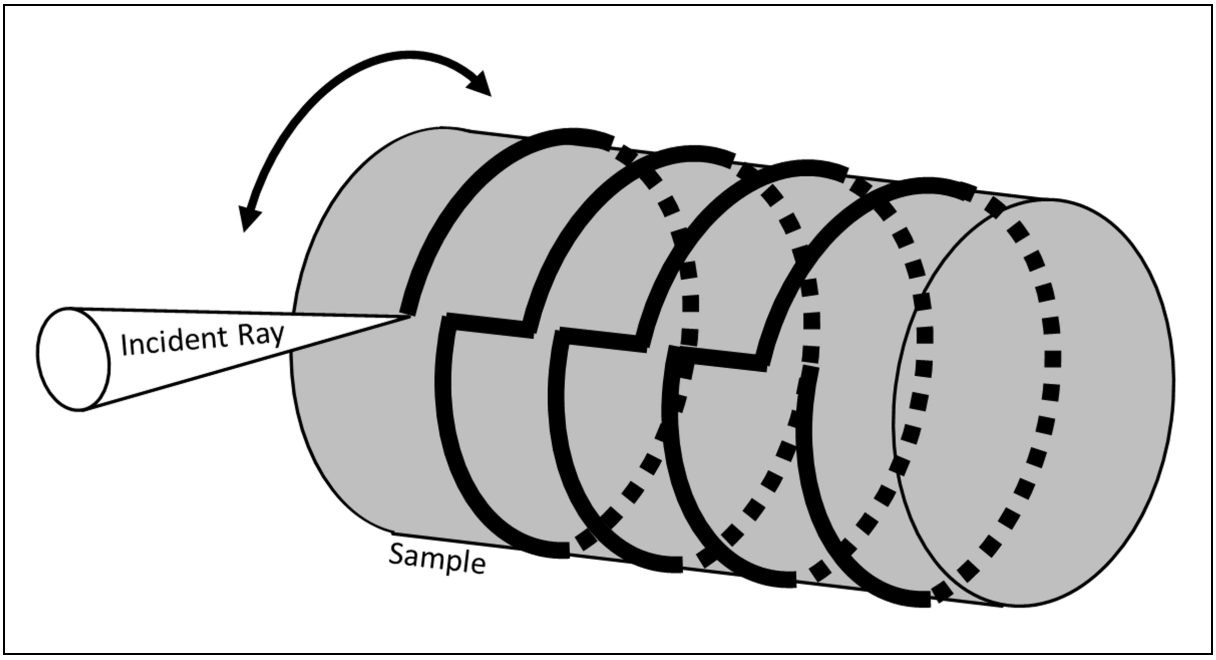

Figure 4.2: The Applied Motion motor rotates the sample and after each rotation the stage moves the incident location one step along the cylinder.

sample is skewered off-centre or if there is variation in the surface structure, the sample surface will oscillate around the focus. If there is enough variation, the scan window will not be inside the tissue at all and the system will lose track of the margin. Even if the margin reappears later in the rotation, there is no way to know if the margin moved in and out of the sample during the time when the scan window was not within the sample. If a margin of healthy tissue does not surround the entire excised tumour there will be tumorous tissue left in the patient. If tumorous tissue is left in the patient, the surgeon must remove more tissue or risk the remaining tumour spreading further. The sample handling system now has three degrees of freedom: translation, rotation, and focus. A three-dimensional scan is achieved by rotating the sample, translating the sample, and probing the depth. The depth scan produces a standard OCT A-Scan and the rotation movement produces a scan analogous to an OCT B-Scan. The resulting image is a coiled scan of the surface that can be unwrapped for display on a 2D computer screen. The three stages are coupled together as illustrated in Figure 4.3. The rotational stage is attached to the focus stage and these are attached to the translation stage. The stages are controlled

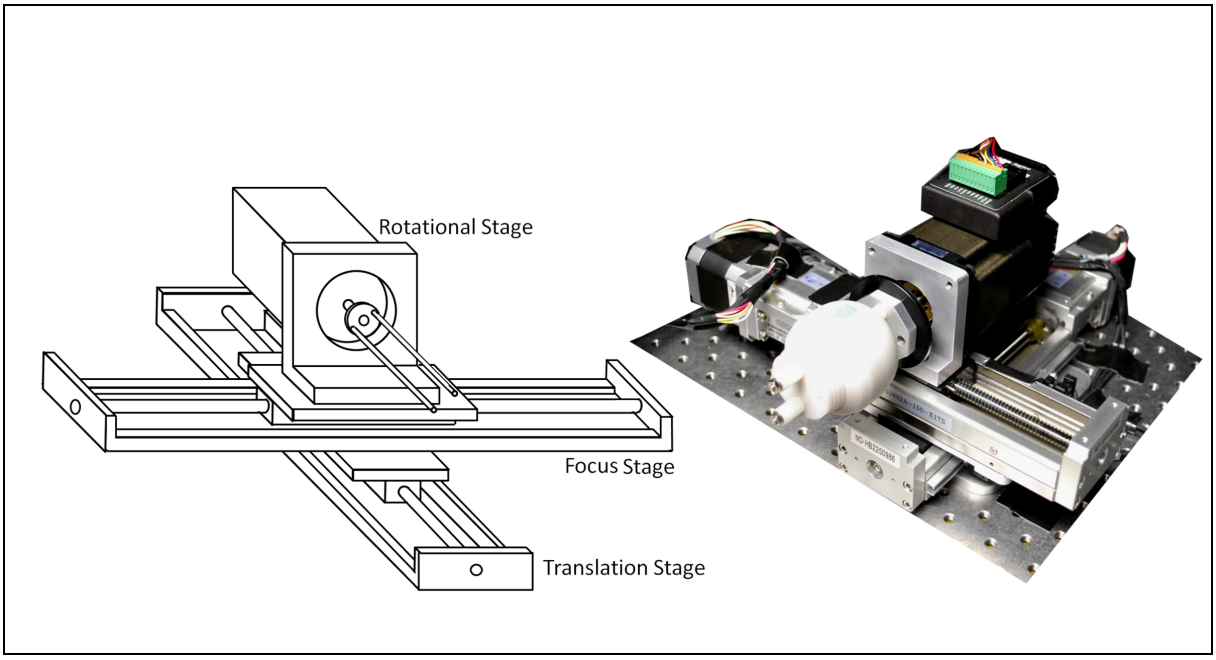

Figure 4.3: The system has three degrees of control: translation, focus, and rotation.

by a Galil microcontroller which includes an onboard amplifier to drive the stepper motors. The translation stage and focus stage are driven by the onboard Galil amplifier and the rotational stage features an integrated amplifier. The entire system is powered by a 24 V, 12 A Galil power supply. The translation stages each include a set of limit sensors to prevent damage to the system by running into bearing hard stops. The controller also includes digital I/O for synchronising with a camera. The system uses a Basler Sprint sensor and is triggered by a TTL pulse via a National Instruments camera capture DAQ. GalilTools code is written to control the flow of operation and movements of the system. A block diagram of the component integration and control is illustrated in Figure 4.4. The Galil microcontroller is the centrepiece of the electronics in the surface scan system. Controlling all the electro-mechanical components within one microcontroller allows for simple integration and synchronisation of the elements. Using stepper motors is less costly than servo motors, but also less accurate. A standard stepper motor increment is 1.8° rotation, but this can be reduced by microstepping. The translation and focus stages may use microstepping as low as 1/16th step, and the Applied Motion rotational stage may be microstepped at 1/256th step. To enable microstepping, the rotational stage must be

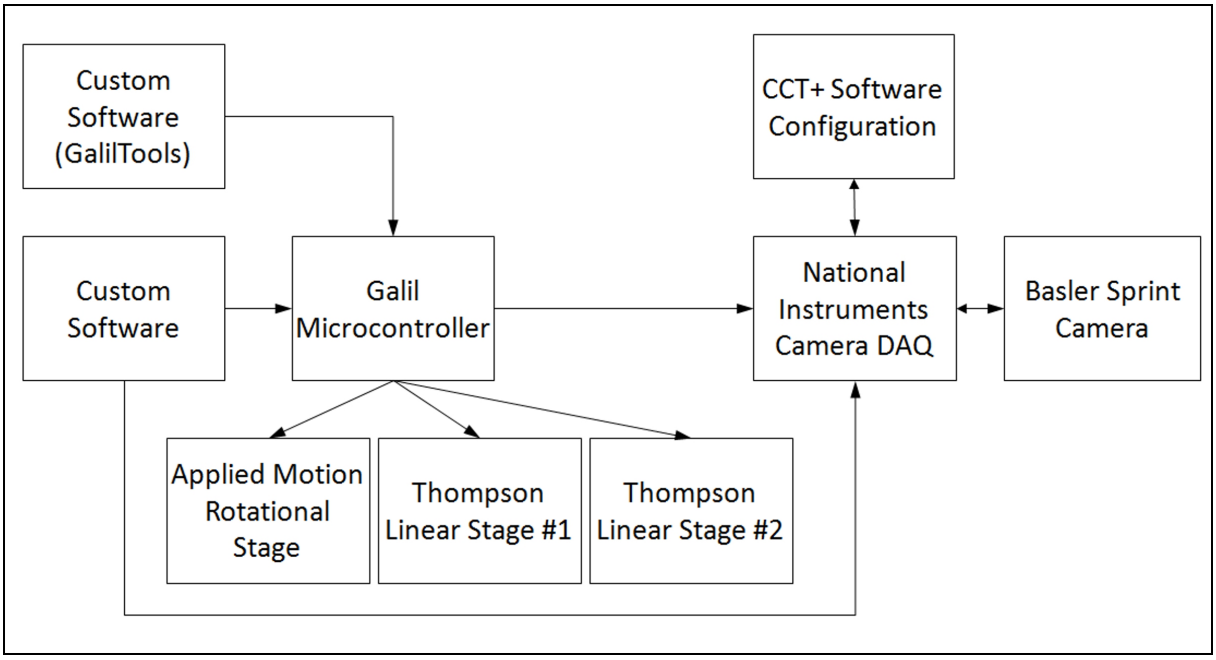

Figure 4.4: The Galil microcontroller is the command centre for controlling each of the motors and camera.

configured using STM Configurator software. The controller code for running a margin assessment scan is included Appendix B

The translation stage is coupled to the focus stage by a simple adapter plate and the stages are centred atop each other. The focus stage is coupled to the rotational stage by an L-bracket adapter plate. The L-bracket has a hole to allow the rotational stage axis to operate within and the bottom is fixed to the carriage of the focus stage, as illustrated in Figure 4.5. To secure the sample for rotation a skewer is used. Two prongs are pressed through the sample to ensure minimal position slipping as it rotates. This is a deviation from the ideal requirements for a margin assessment system. Ideally, the assessment would be non-damaging to preserve the integrity of the sample. There is a minor chance that the skewer locations may include negative margins that are now undetectable. Future additions to the sample handling system may also include an additional stage to account for angled surfaces. The current system will work with cylindrical samples and small angles, but will have difficulty assessing the margin if the angle between the optical axis and the surface tangent is too large, as illustrated in Figure 4.6. The effective penetration depth from the

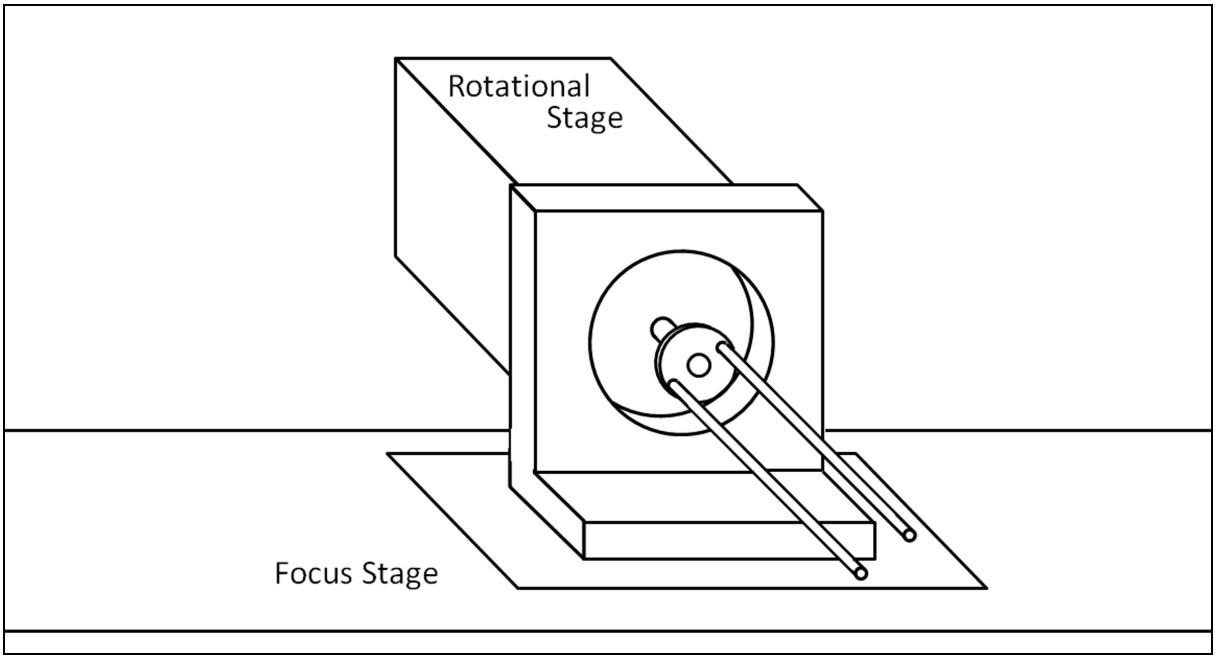

Figure 4.5: The Applied Motion rotational stage and the Thompson focus stage are coupled using an L-bracket mount.

surface follows the sinusoidal relationship,

$$d_{eff} = dsin\theta, \tag{4.1}$$

where d_{eff} is the effective depth into the sample (the depth that should be used for margin assessment), d is the penetration depth for on-axis scanning, and θ is the angle between the optical axis and a line tangent to the surface. At an incident angle of 30 °, the effective penetration is half that of the on-axis depth.

4.1.1 Synchronisation

The synchronisation of a margin assessment scan is illustrated in Figure 4.7. The system operates on a step-and-hold scheme where the sample is held still during camera exposure. All motion occurs according to sequential operation of the Galil control code and synchronised according to an internal clock. Clock synchronisation occurs invisibly to the user since all code occurs within the one microcontroller. This simplified scan diagram

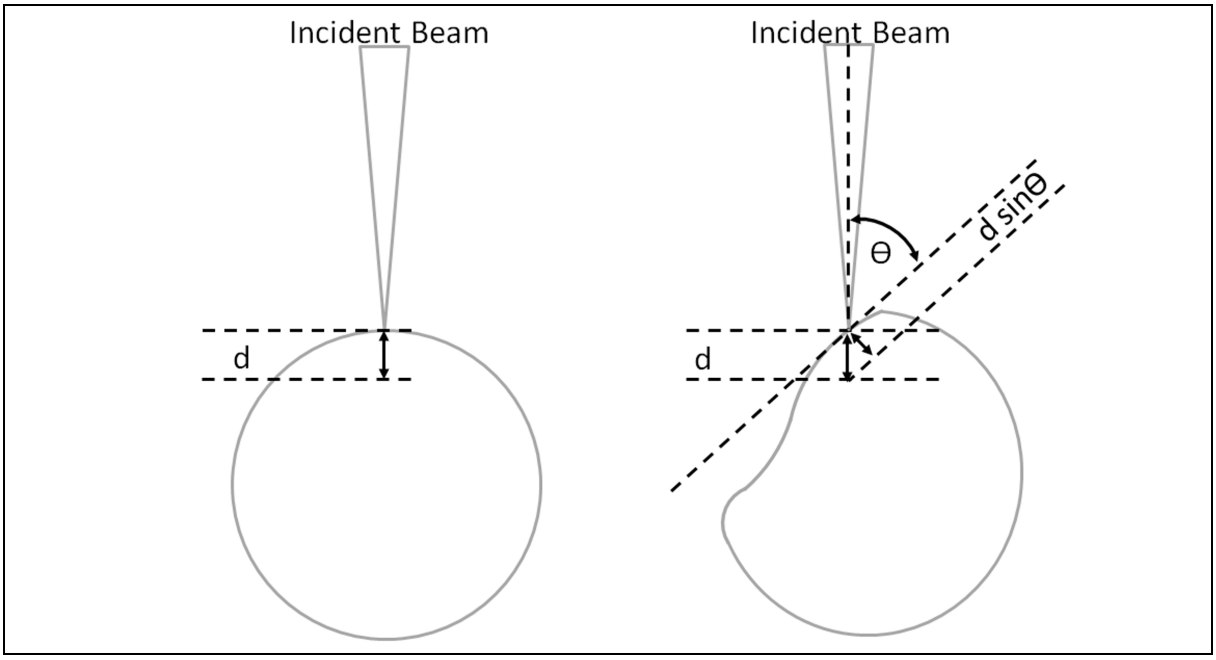

Figure 4.6: The penetration depth from the surface decreases for non perpendicular penetration.

shows images taken at regularly spaced rotation intervals along the surface of the sample. For each location around the sample a TTL pulse triggers the sensor to take an exposure and the rotational stage holds still for the pre-set exposure time. Initial experiments yield a sensor integration time of <1 ms to be ideal for collecting images. When a rotation is complete, the translation stage moves forward one step and the next rotation begins. The focus stage adjusts at the start of the scan to bring the sample surface to the focus. The spacing for each translation step and the number of scan locations around the circumference of the sample are determined a-priori. The number of locations around the sample is analogous to the number of A-scans in a B-scan in traditional OCT parlance. To ensure the rotational stage will always end up at a known starting position for each B-scan, there is a correction at the end of each rotation where the stage rotates to a given starting position. This correction is necessary when the division of the step-size into a full rotation yields a remainder.

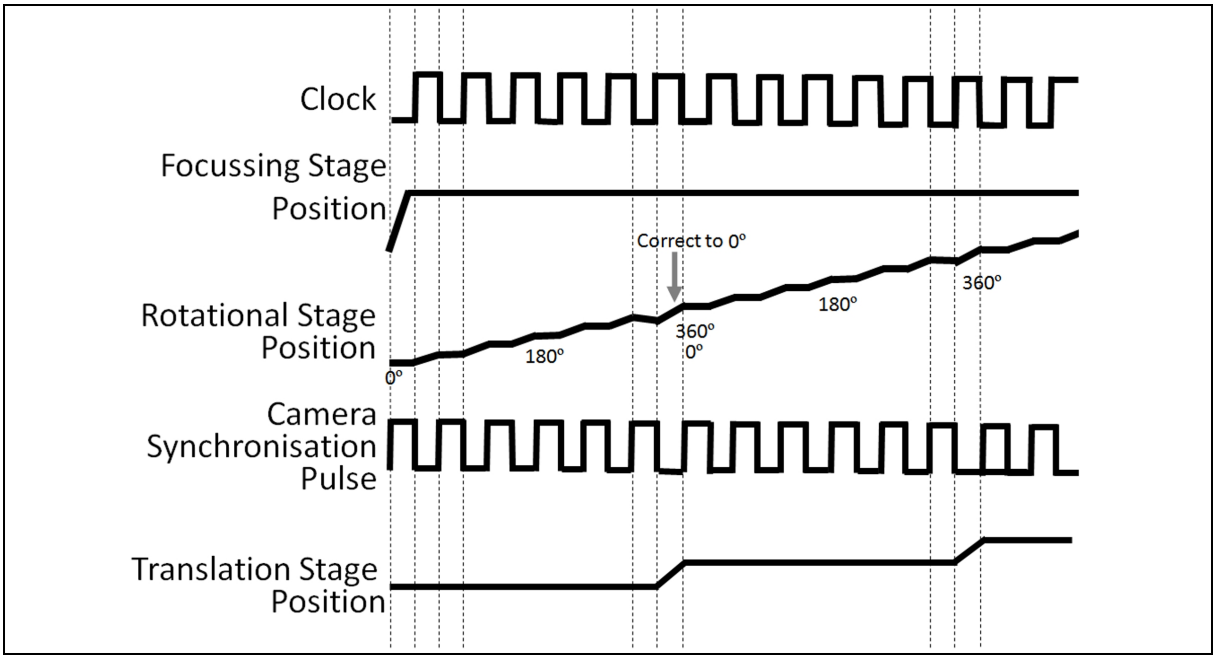

Figure 4.7: The synchronisation scheme of the sample handling system operates on pulses to identify when movements should be made. Two B-scans are shown.

4.2 System analysis

The rotational stage operates based on the input of the desired angular change and so a relationship between angular rotation and the surface distance should be used. For this to yield operational specifications, a standard phantom size must be identified. A sample cylinder 50 mm long and 50 mm diameter is used for the following calculations. The arc length of a circle will help to determine the surface spacing and is given,

$$A_L = r\theta, \tag{4.2}$$

where A_L is the arc length, r is the radius, and θ is the angle (in radians) the rotational scan will move. The smallest feature size prominent during margin analysis is 0.15 mm, but is generally larger —as large as several cm [29]. Three surface length sizes were identified for study: 0.25 mm, 0.5 mm, and 1 mm. Although these sampling rates may miss the smallest of tumour features, they balance the requirement for fast operation with resolution. Some studies suggest surface spacing on the order of mm's is sufficient [7].

Typical pathologic analysis is performed post-operation where the tumour is sliced into sections 3 mm thick. From each 3 mm block, a 5 μm thick section is further removed for analysis under microscope.

A surface spacing of 0.25 mm on a sample 50 mm in diameter requires a rotation of 0.57 °; 0.5 mm requires 1.14 °, and 1 mm spacing requires 2.29 ° rotation. The rotational stage is able to use microstepping with as many as 51200 steps per 360 ° rotation (256 microsteps per standard stepper motor increment). The microcontroller specifies the rotation by the number of microsteps to move. The translation stage also uses a stepper motor, but is only capable of 1600 steps per 360 degree rotation. The stepper motor is coupled to a ball screw to generate linear motion and each full rotation generates 2 mm linear translation. Table 4.1 illustrates the spacing parameters and the relation to rotational stepper movement. If the rotational stage were moved 1 microstep, this would translate

Table 4.1: the surface spacing needs to be related to angular rotation and in turn, the number of microsteps to perform the operation.

	Rotational Stage [51200 microsteps per rotation]		**Linear Stage [1600 microsteps per rotation]**	
Surface spacing [mm]	**Rotation required [°]**	**Microsteps required [microsteps]**	**Rotation required [°]**	**Microsteps required [microsteps]**
0.25	0.57	81	45	400
0.5	1.14	162	90	800
1	2.29	325	180	1600

to 3 μm movement and if the linear stage were moved 1 microstep, this would translate to 0.6 μm movement. In practice, however, it tends to be better to move multiple microstep increments. Due to the small currents present in microstepping, a single microstep may not be enough to overcome the static friction in the motor and the inertia of the sample.

4.2.1 Spatial resolution

There are two considerations in determining the resolution of the system. Both the Raleigh Criterion and the sampling frequency must be considered. For a beam that 18 mm in diameter, an achromatic focusing lens ($F_L = 250$ mm, $\phi = 50.8$ mm), and a centre wavelength of 840.7 nm, the Rayleigh Criterion is 14.1 μm. The tumours being analysed are much

larger than 14 μm, so optically, there is no issue imaging the features of interest. Here, the sampling rate is the limiting factor.

4.2.2 Operation time

The operation time is a primary consideration for margin assessment since the ideal case is for intraoperative assessment as the patient waits. By assessing the margins intraoperatively, there will be fewer re-excision surgeries required. There are several key factors in estimating the system operation time. The total scan time may approximated by,

$$Time = L_L(L_R T_R) + (L_L T_L) + T_{SB}, \tag{4.3}$$

where L_R is the number of locations scanned in one rotation, T_R is the time for each rotational increment to be performed, L_L is the number of linear locations to be scanned, L_T is the time for each linear increment to be performed, and S_B is the scan-back time for the translation stage to return to the initial position. There is no associated scan-back for the rotational stage since it will already be at or very close to the zero rotation position after each scan. L_R is the time from one rotational increment to the next, and thus incorporates the integration time for capturing the image. Measurements from the GalilTools integrated oscilloscope yield values for L_R, L_L, and $T_S B$ for each of the test scenarios, as described in Table. The time for a rotational scan movement is nearly constant for increasing step sizes,

Table 4.2: the time parameters for each movement help to estimate the total scan time required.

Rotational Step size [mm]	**Translation Step size [mm]**	**LR [# of locations]**	**TR [s)**	**LL [# of locations]**	**TL [s]**	**SB [s]**	**Calculated Scan Time [s]**	**Measured Scan Time** [s]
0.25	0.25	628	0.080	201	0.128	20.023	10006	9461
0.5	0.5	314	0.088	101	0.192	13.375	2819	2651
1	1	157	0.088	51	0.240	8.930	726	726

while the translation stage movement time increases considerably. This can be attributed to the fact that the rotational stage is moving small amounts on a directly driven rotational stage; the sample is attached directly to the rotational shaft. The translation movement, however, is driven linearly via ball screw assembly. Increasing step sizes requires increasing rotation and there is a multiplicative factor to the time increase.

4.3 Optical analysis

A model of the light delivery was developed in ZEMAX. A diagram of the model is in Figure 4.8. This simple model includes an achromatic lens ($F_L = 250$ mm, $\phi = 50.8$ mm) with a beam diameter of 18 mm and a centre wavelength of 840.7 nm. The model is optimised with a ZEMAX merit function that minimises the RMS error of the optical spot centroid. The spot diagram from the ZEMAX Geometric Image Analysis is illustrated in Figure 4.9.

The ZEMAX Geometric Image Analysis shows that the focussed spot is well contained and shows little spherical aberration. The data for the achromatic lens were taken from a ZEMAX file provided from the manufacturer. Lens spherical aberrations have little effect on the spot here since the beam moves on-axis through the lens. Adding an additional ZEMAX layer beneath the lens focus, but before the image plane, allows for slight improvement to the spot RMS. Spherical aberration is a zonal aberration and traced rays come to a focus at slightly different lengths along the optical axis [15]. The optimised model suggests the minimal spot size to occur 243.187 mm from the front of the lens, along the optical axis. This is 0.4 mm greater than the manufacturer's identified focal plane. The FWHM of the spot, as calculated by vertically binning the Geometric Image Analysis plot, is 19 μm.

Depth of focus is an important consideration for margin assessment since the primary goal is to find the boundary, at whatever depth it is present, not to resolve cellular histology. The depth of focus for this system is 108 μm. Performing a through focus analysis allows for investigation into what happens when the sample surface moves in and out of the focal plane, as illustrated in Figure 4.10. As defocus occurs, the spot size increases dramatically. If the margin falls outside of the DOF or after the spot size has enlarged, it may not be as clearly resolved, but should still be visible over the penetration depth. Additionally, a higher f-number lens will give a better depth of focus than a lower f-number lens, but the spatial resolution will decrease. It is recommended to stay with as high an f-number lens as possible.

4.3.1 Alignment and degree of freedom concerns

The system includes three moving axis: rotation, translation, and focus. As such, it is important to minimise any other degrees of freedom that may affect performance as the sample is manipulated. The lens is housed in a fixed mount and the only degree of adjustment is rotation as the mount is secured. The mount must be secured perpendicular

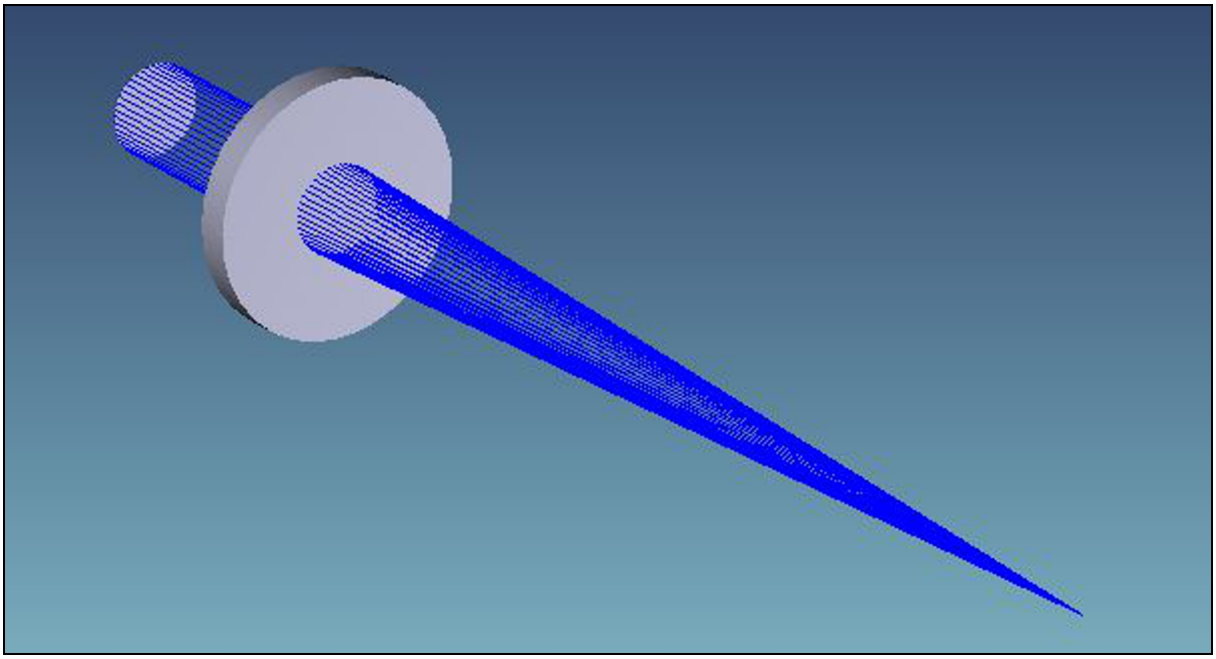

Figure 4.8: The ZEMAX model of the focusing system includes one lens.

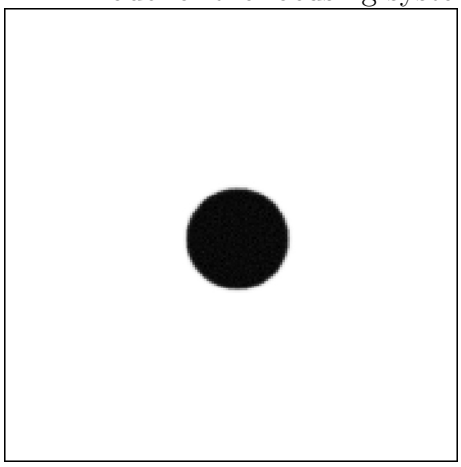

Figure 4.9: The focussed spot can be obtained within the ZEMAX Geometric Image Analysis.

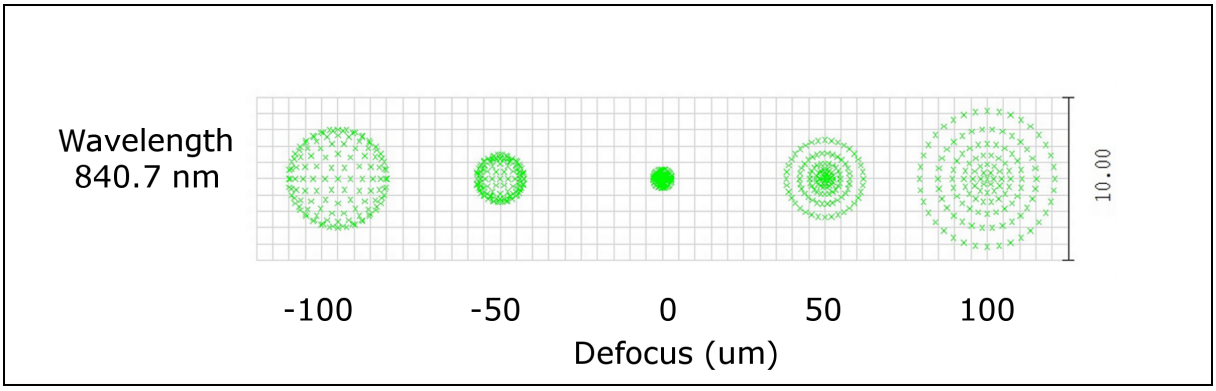

Figure 4.10: A ZEMAX Through Focus Analysis shows the effect of the sample moving in and out of the focal plane during imaging. The scale line is 10 μm.

to the beam propagation direction and if secured well, should not move, nor cause any problems over time. Each of the stages couples to the table or another stage with a metal adapter plate. The adapter plates allow only one orientation of mounting. Since the focus stage frame is secured to the moving platter of the translation stage, and the rotational stage is secured to the moving platter of the focus stage, stiff mounts are required. The mounts are made from aluminum and are 15.875 mm thickness. During operation, only the three desired degrees of freedom: rotation, translation, focusing, are enabled and able to be manipulated.

4.4 Performance optimisation

Tests were performed for three step sizes: 0.25 mm, 0.5 mm, and 1 mm steps. A key parameter that affects stepper performance is the smoothing factor, K_S, available in the Galil microcontroller. The smoothing factor adjusts the timing of the stepper pulses to allow for smoother movements. K_S adds a first-order low-pass filter to the pulse generation circuitry to slow the frequency of pulses. The magnitude of the smoothing factor is proportional to the degree of smoothing, but inversely proportional to the overall movement time. As K_S increases, there is more smoothing, but the movements take longer. The rotational stage was examined for a range of smoothing factors from 2 through 50. The default smoothing is 2 and may be adjusted between 1 and 64. Another parameter affecting the timescale over which smoothing occurs is TM, the update time for control functions. TM was set

to 1000 μs for all of the tests and provides a reasonable update rate. Setting TM lower decreases the time between updates and increases the effect of the smoothing factor since it may smooth on a more frequent basis. Tests were completed by moving the shaft forward and backward each of the three step sizes. The data for the 1 mm step are shown here and are illustrative of the data seen for 0.25 mm and 0.5 mm steps. The movement profiles are the commanded movements rather than the actual movements since there are no encoders on the stepper motors and no way to illustrate the actual physical effects. Similar tests were performed with the linear stage. 1 mm linear movements are again representative of the movement profiles for 0.25 mm and 0.5 mm movements and so the 1 mm is displayed here. The rotational and linear smoothing test profiles are shown in Figure 4.11.

For the rotational stage, low values like K_S=2, provide limited smoothing and the sample may be seen visually oscillating as it moves from position to position. K_S=50 shows a situation where too much smoothing is present, and K_S=10 shows a moderate level of smoothing with limited time increase. The high K_S values do not add significant stability, but take much longer to come to a final position. K_S=5 is a good balance between a jerky and smooth movement and occurs over a reasonable timescale. For a 1 mm rotational step size, there are 157 movements per rotation; even small timescale changes are important to the overall system operation time since there are so many movements affected.

There is also an important difference between the rotational axis and the translation axis; the images are not set to be captured during the linear movements. The linear increments occur only once per full rotation and so affect few or no image locations. Setting K_S=1 is appropriate for the linear movements because it minimises the time taken to move and the sharper command pulses do not add significant oscillation to the signal. The translation stage can accommodate a lower smoothing parameter because the payload is not directly driven by the stepper motor. There is additional mechanical rigidity in the transfer of rotation through the ball cap screw into the linear motion. A low smoothing parameter has a more noticeable physical effect on the rotational stage where the payload is attached directly to the stepper shaft. Using a higher K_S value introduces some delay in the stepper command pulses. These delays can be significant, as illustrated in 4.12. While the frequency of pulses stays approximately the same, the time taken to reach the commanded position varies considerably, reducing the dwell time at that final position. For situations like the rotational stage, where the held (flat) section of the pulse is important, these delays can have large consequences like introducing movement during imaging.

Testing was also performed to determine the maximum speed values for the linear and rotational axis. Full rotations were performed and iterative adjustment was made to the acceleration, deceleration, and speed parameters. There are some interesting effects that occur if the accelerations and decelerations are set too high. Looking only at the

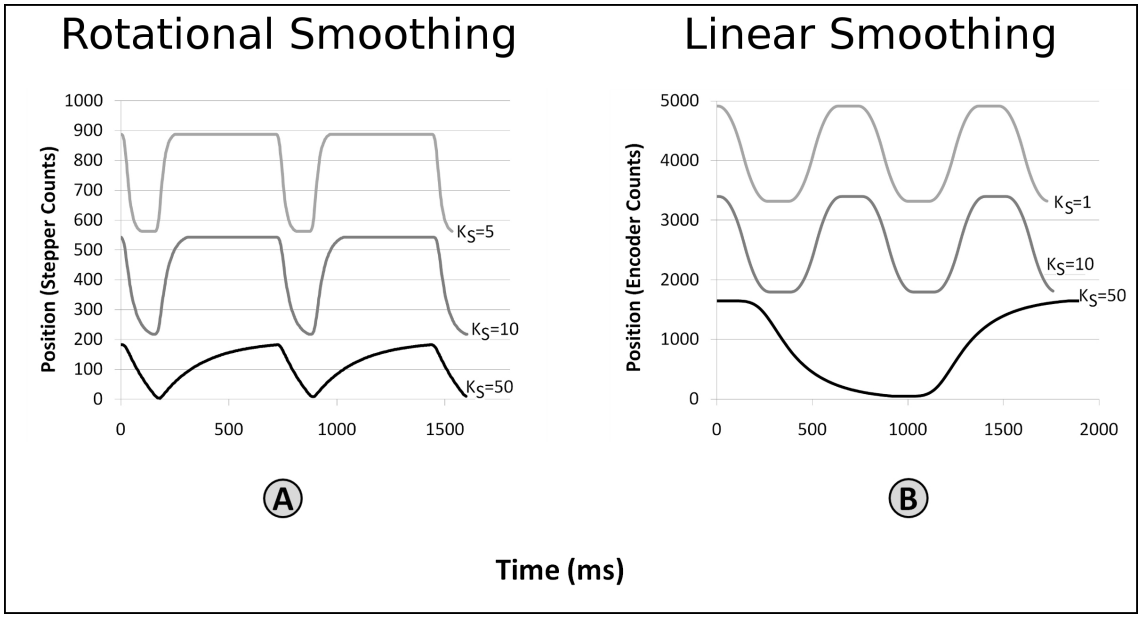

Figure 4.11: The rotational stage movement profile shows that as the K_S factor increases, sharp movement edges are removed. Sharp edges correspond to strong velocity or direction changes.

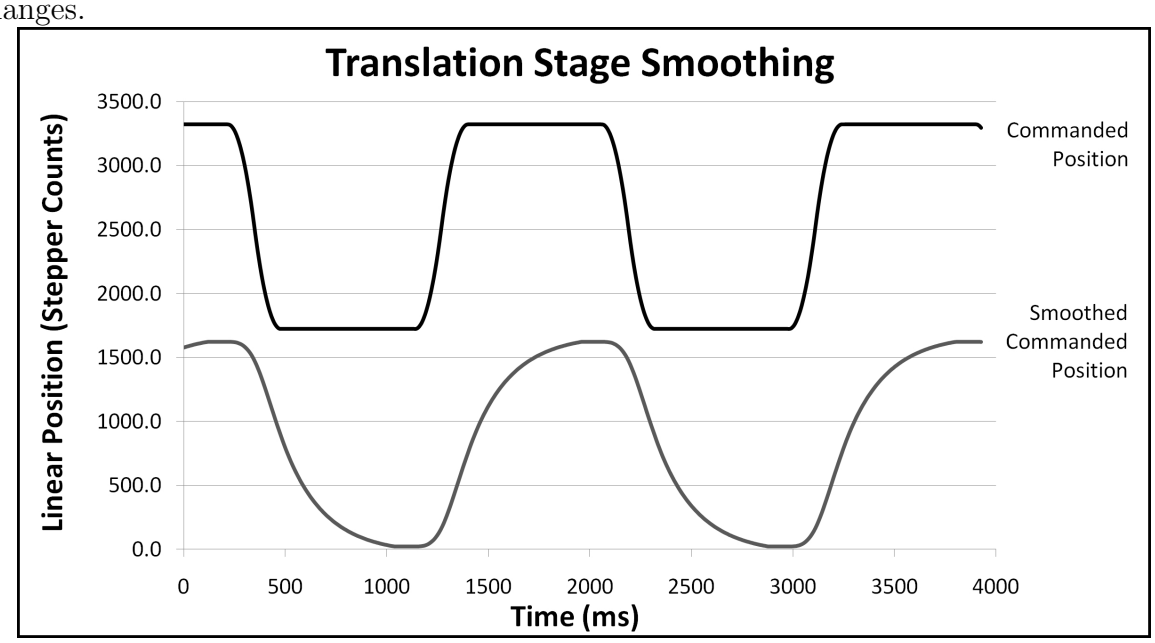

Figure 4.12: There is a motion profile difference between the commanded input and the stepper pulses output when the K_S value is introduced.

total scan time, values higher than those tabulated in Table 4.2 actually increase the total scan time. Once the values hit a maximum they can be increased, but will not have any physical effect other than this slight increasing zone. The most appropriate method of setting speeds is to find the maximum value before the time increase takes place. Table 4.3 illustrates the ideal performance parameters for minimum time operation. For the linear stage, provided the movement sizes are small —less than a few mm— the ideal accelerations and decelerations are the same for each of 0.25 mm, 0.5 mm, and 1 mm step sizes. The linear speeds, however, should be customised for the required movements. The accelerations and decelerations occur over approximately the same time scale and so for all tests, the acceleration and deceleration values were coupled to decrease the number of variables in the tests. It should also be noted that the physical relation for the speed,

Table 4.3: Speed, acceleration, and deceleration allow for the overall time of scan to be optimised.

Parameter	**Rotational (0.25 mm step)**	**Rotational (0.5 mm step)**	**Rotational (1 mm step)**	**Linear (all)**
Speed (counts/s)	6000	10 000	15 000	4000
Acceleration (counts/s^2)	1 500 000	1 500 000	2 500 000	100 000
Deceleration (counts/s^2)	1 500 000	1 500 000	2 500 000	100 000

acceleration, and deceleration values above are not the same for the rotational and the translation stages. Since the rotational stage has 51 200 encoder counts per rotation and the linear stage has only 1600 per rotation, the magnitudes of the rotational movements will be larger to accomplish the same number of revolutions. This is confused further by the translation stage operating upon rotational movement being converted to linear motion via a ball cap screw assembly. The translation stage moves at a rate of 2 revolutions (3200 encoder counts) per 1 mm linear motion.

One final note about coding for stepper motors is the use of wait commands. For closed loop systems, AM — after motion, is used. For stepper motors, MC — motion complete, is used. The use of AM is not advisable and produces anomalous results for open loop stepper motors. MC waits until all step signals have been sent and takes into account delays due to smoothing with the K_S parameter.

4.5 Actual scan

A full system test of the sampling handling system was performed to evaluate the total speed of operation. The optimised values for smoothness and speed described in the proceeding sections were incorporated into the scans to provide a balance of low scan time and smooth operation. The system is fully adjustable to provide step increments as low as perhaps 0.1 mm steps, which is the practical limit for accurate stepper based linear stages without encoders. Full tests were performed for 0.25 mm, 0.5 mm, and 1 mm step sizes in both the linear and rotational directions. Typical exposure times are less than 1 ms, so a 1 ms delay was incorporated for these tests. The spacing of the rotational steps and the linear steps are not required to be the same, but were kept equal during these experiments to ensure even spacing of resultant images. The motion profiles for a full margin assessment scan are illustrated in Figure 4.13. The full scan in Figure 4.13 occurred over 726 seconds

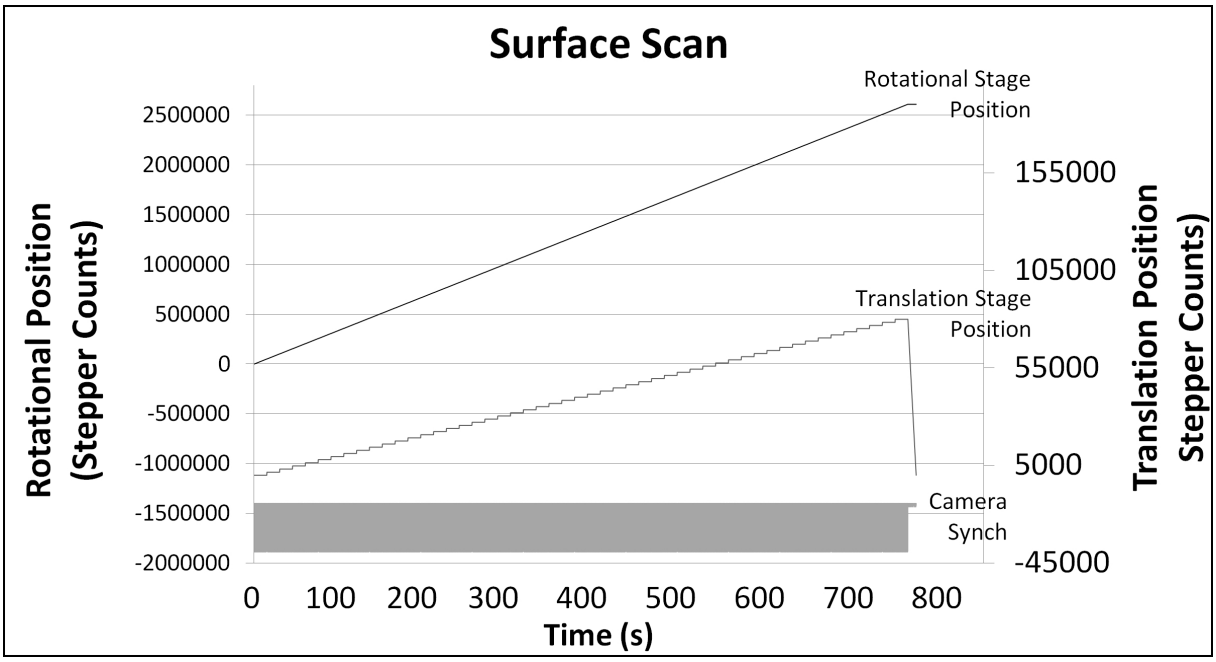

Figure 4.13: The rotational stage position, translation stage position, and camera synchronisation must be timed to occur during specified intervals.

(12 minutes, 6 seconds). For each linear translation position, 157 images are taken over regular spaced rotational locations. For each of those 157 locations, a TTL camera pulse

is sent to command the image to be taken. The camera pulse is sent after the stepper has stopped receiving movement pulses and should be still. A step and hold architecture is used to keep the sample as still as possible over the integration time. The rotational stage position count increases every revolution and does not reset to zero when it has reached the initial position.

4.6 Conclusions

A system for performing margin assessment was developed using OCT technology. The sample handling and light delivery system uses a rotational stage, a translation stage, and a focus stage to enable full three-dimensional surface scanning. A skewer is attached to a rotational stage to hold the sample in place, but this does forgo the analysis of the punctured sections.

A key requirement for assessment of OCT suitability intraoperatively is the total scan time and it is desirable to have a scan performed in less than 20 minutes. Scans were performed over various surface spacing intervals to test total scan time. Sampling every 1 mm along the circumference and taking a rotational measurement every 1 mm longitudinally down the sample allows for a scan to be performed in approximately 12 minutes. This spacing and speed meets the 20 minute requirement, although additional time may be necessary for image reconstruction and segmentation.

Some estimates place the features size for margin assessment to be as low as 0.15 mm [29]. Scanning at this spacing would require a different solution than that presented here. To increase accuracy of stepper motors, an encoder may be added to each stepper, but this adds cost to the system and does not solve time constraint issues. Servo solutions have the ability to further increase the accuracy of the stages and operate within tighter time constraints. However, servo solutions further increase the cost of components. The current system has the capability to reach speeds in excess of those required for quick and low spaced scans, but only if operated continuously. The system should be tested under conditions where the sample is continuously rotated in a raster scan to see what impact this has on the resultant images. Since the imaging system is not intended for resolving cellular details, but rather resolving the broad margin location, imaging during movement is likely to yield acceptable results.

The gold standard for margin assessment is the pathological examination of samples under a microscope. This is a time consuming process and cannot be performed at a rapid enough pace to influence the initial excision if the sample excised is large, like in BCS.

Additionally, the process is sample limited where due to the large evaluation time, one slice per 3 mm is examined. This process may yield false negative results since such a large spacing is used. The need for specialised imaging technicians to evaluate the imagery makes this a highly trained profession and places a cap on the number of images that can be evaluated. Having digitised images, like those generated in OCT, that are able to be segmented and potentially evaluated by non-experts means less time from imaging to excision decision. With proper testing, intraoperative OCT margin assessment can become an indispensible tool. OCT margin assessment can have a real impact on the workflow during tumour excisions and ultimately, on the quality of patient life by limiting the need for multiple surgeries. There is a stated clinical need for a sample handling system that enables quick, thorough margin assessment. The surface scan system described here fills that need and can help bring intraoperative OCT margin assessment to realisation.

Chapter 5

Conclusions

OCT is well-suited to imaging in turbid media like tissue. The ability of OCT to penetrate a surface and provide a depth profile means that three-dimensional imaging is possible with this modality. Controlling the light beam and sample position during the process of generating a plane of depth profiles becomes challenging when the surface is an unusual shape or the spacing is small. Two devices for controlling light delivery were presented in this thesis and analysed to show how they enhance obtaining imagery for their target applications.

5.1 Trapeze

The trapeze was presented as a system that is more flexible than traditional two-galvanometer scan systems. Integrated into a test-bed OCT system, the trapeze accommodates flexibility in sample size and type, provides three-dimensional imaging, intakes a variety of beam sizes and heights, and provides easy initial alignment. The trapeze performs manipulation of the light beam with a galvanometer while moving a sample beneath after each galvanometer B-scan. The galvanometer's rapid scan capabilities, combined with the relatively large linear stage stroke allow for a wide variety of samples to be scanned. Over time, iterative trapeze designs improved ease of alignment and the spatial resolution from the first to the second system. Modelling of light propagation in ZEMAX identified key restrictions in the scan range of the trapeze in order to limit aberrations caused by off-axis scanning.

Three galvanometers, two linear stages, and one DAQ were tested to determine the suitability of each for use in the trapeze. By testing the hardware to the limiting cases,

clear differences in the hardware emerged. Finally, the trapeze was run through a full three-dimensional scan routine to determine areas that could be optimised and lead to more efficient operation. The following primary results were found:

- The mounts for light delivery components should restrict the degrees of freedom and adjustability to only those necessary for fixing slight tip or tilt of the entrance beam and for changing the entrance beam intake height. This will help to limit complex alignment.

- A galvanometer-stage combination allows larger sample sizes than typical two-galvanometer OCT systems, but retains the high speed galvanometer operation during B-scans when it is most important.

- Using a Z-stage beneath the focusing lens allows for fine focal control by changing the distance between the focusing lens and the sample surface. This is a less cumbersome adjustment than moving the focusing lens to produce the same result.

- The trapeze operates near the limits of position noise for the DAQ and galvanometer. It is in this limiting case that the Nutfield galvanometer proves to be a stronger choice than the Cambridge and Thor Labs galvanometers.

- Both the Nanomotion and Nippon Pulse linear stages are suitable for use in the trapeze. However, the Nippon Pulse offers superior stability during both movement and holding routines.

- The position noise of a linear stage, which governs repeatability and minimum step size, depends on more than just the encoder resolution. Despite both the Nanomotion and Nippon Pulse stages having 10 nm encoder resolutions, the Nanomotion exhibited more than three times the peak-to-peak position noise of the Nippon Pulse and more than eight times the RMS error.

- Optical spot size analysis should be performed to determine scan operation parameters. The step size for the galvanometer should be matched with the step size of the linear stage to provide even spacing and will meet Nyquist sampling when they are set to half the Rayleigh Criterion.

- There are inefficiencies in the trapeze scan algorithm resulting in wasted time during the scan-back phase of the galvanometer, during which time the stage also moves. Reducing the delay between scans from 145 ms to 50 ms would still provide sufficient time for the stage and galvanometer movements to occur, but would save 95 ms per

B-scan. If there are special requirements for slow stage movements, like a sample sensitive to motion for example, the stage speed may need to be reduced and the delay increased accordingly.

5.2 Assessing Margins

For assessing the margin of healthy tissue surrounding a tumour, the entire surface must be imaged. Efficiently scanning the entirety of a sample's surface is a challenging procedure. To accomplish this, a rotational stage coupled to a focus stage and a translation stage was assembled. By fixing an excised tumour to the rotational stage full circumference scans are possible. By translating the rotational stage, the circumference scans will move through the extent of the shaft, allowing a large percentage of the sample to be scanned. The surface scanner has the potential to be an intraoperative tool for margin assessment because it is able to scan within 20 minutes and provide a survey of much of the surface. Pathologic analysis under a microscope is the gold standard for assessing margins, but does not sample provide high sampling density of the surface. The solution presented here solves the sampling issue by providing ample configuration abilities for the scan spacing for both the rotation arc length and translation step size.

Testing of open loop stepper motors is limited because there is no motion profile available without a position sensor. Instead, the microstep pulses and the commanded position were tested to determine the effects of changing parameters like K_S (smoothing), speed, and acceleration. Full scan routines were executed to determine total system operation time in order to evaluate against the surgeon stated requirements. Full scans were performed for step sizes, equal in both rotational and linear directions, of 0.250 mm, 0.5 mm, and 1 mm. The following primary results were found:

- The use of a stepper based design reduces cost, but also accuracy. By specification, the Applied Motion rotational stage and the Thompson based linear stages meet the step size requirements of margin assessment. If possible, position sensors should be added for confirmation of this.
- Microstepping is essential for high precision use of stepper motors. However, small microstep counts should be avoided since low current levels may not provide the torque to overcome stiction.
- If the sampling step size is larger than the Rayleigh Criterion, the step size may be arbitrarily set and will govern the resolution of the system. Literature suggests

margin assessment will be exposed to features as small as 0.150 mm, but a larger step size is likely sufficient.

- Using a skewer to hold the sample to the rotational stage will limit the amount of the surface that can be scanned, but the coverage still has the capability to be more thorough than the gold standard, one 5 μm slice every 3 mm.
- If the sample shape includes a varying profile, the incident beam may not be perpendicular and depth penetration will be limited. Moving to realistic shaped phantoms will help to determine if additional angular flexibility is necessary during scans.
- Use of a moderate stepper smoothing factor (K_S=5) for the rotational stage is recommended. Although this increases total scan time, the difference in smoothness of the step pattern is significant and can be seen visually.
- To reduce scan times, tests should be performed during continuous raster imaging for rotational motion rather than a step and hold scheme. If this yields adequate margin detection imagery, speeds will improve substantially and smaller step sizes may then fall into the limited time threshold.

Although still in early phases, intraoperative OCT margin assessment has the potential to become an indispensible tool. OCT margin assessment can have a real impact on the workflow during tumour excisions and ultimately, on the quality of patient life by limiting the need for multiple surgeries. There is a stated clinical need for a sample handling system that enables quick, thorough margin assessment, and the solution presented here fills that need.

5.3 Final thoughts

The test-bed OCT system presented in Chapter 3 and the margin assessment OCT system presented in Chapter 4 have very different application areas, but it can be seen that there is a similar structure to the design and evaluation of the light delivery and sample handling components for these systems. In both systems, integration and synchronisation is key for obtaining precisely timed imagery. The components must be tested in the limiting case to determine performance differences and deficiencies. Both systems were implemented with step and hold architectures, which places limitations on the system operation speeds. In order to obtain low optical noise levels in the test-bed OCT system, multiple exposures are taken for each location and as a result, the step and hold architecture

is appropriate. For margin assessment, however, the goal is not histology, but rather detection of a single margin and this may be possible with a continuous raster scan and a single exposure per location. Additionally, it can be difficult to determine the performance of off the shelf components prior to integration into the system. Considerations like mount rigidity, ambient electronic noise, and motion step response are difficult to evaluate before a prototype is in hand and operating in the target setting. Multiple prototyping phases may be necessary to increase ease of alignment or to determine if better components exist. Finally, resolution requirements should guide selection of many of the components for light delivery. OCT is limited to μm resolution and so having stages that overperform as much as the Nanomotion and Nippon Pulse stages is not necessary, but does provide a high degree of stability.

Controlling the light delivery and sample positioning of an imaging device adds important functionality to a scan system. This is important in industries ranging from biomedical imaging to remote sensing. The careful design of an imaging system to meet the unique requirements of the application enables better information and better resulting decision making. The goal of high performance imagery is to provide new insight and perspective to everyday scenes. It is these new perspectives that allow for re-evaluation and examined of problems with a fresh eye. As medical imaging becomes more pervasive in society, it is important to understand system limitations, but just as important is understanding how the technology can be used to improve quality of life.

APPENDICES

Appendix A

GalilTools Code for an OCT Scan

```
'************************************************************************
'OCT SYSTEM STAGE SYNCH CODE
'************************************************************************
'DESCRIPTION:
'SYNCHRONISES MOTION WITH AN DAQ INPUT
'************************************************************************
#START
'==================USER INPUT PARAMETERS HERE============
step=300 ;'DISTANCE BETWEEN STEPS, UNITS [10 NM]
loop=100 ;'NUMBER OF STEPS, SAME AS IN GRABANDMOVE OCT "REPEAT"
'THE NUMBER FOR LOOP REPRESENTS THE NUMBER OF B-SCANS.
'THE STAGE WILL MOVE (LOOP-1) TIMES.

'==================DO NOT CHANGE BELOW CODE=============
TM100   ;'SERVO LOOP TIME
IL1.5   ;'INTEGRATOR LIMIT
KP3     ;'PROPORTIONAL GAIN
KD40    ;'DERIVATIVE GAIN
KI0.065 ;'INTEGRAL GAIN
IL1.5   ;'INTEGRAL GAIN USED ABOVE THIS LIMIT
FA0     ;'FEED ACCELERATION
FV0     ;'FEED FORWARD VELOCITY
AC1000000
DC1000000
```

```
SP1000000

SH
DP0     ;'RESET ZERO POSITION POINT

n=1
MG"STARTING AT POS:",_TPA
AI+22 ;'INPUT 22 SET TO HIGH AT START
#REPEAT
  AI-22   ;'WAIT FOR INPUT 22 TO GO LOW
  PA (n*step)
  BGA     ;'START MOTION
  AMA     ;'WAIT FOR MOVEMENT TO COMPLETE
  n=n+1
  TPA
  AI+22   ;'WAIT FOR INPUT 22 TO GO HIGH
JP #REPEAT, n<loop

'RETURN TO INITIAL SCAN LOCATION
WT2000
SP10000
PA0
BGA
AMA  ;'WAIT UNTIL HOMING FINISHES
MO

MG"DONE, ENDED AT:", _TPA
EN      ;'END OF PROGRAM
```

Appendix B

GalilTools Code for a Margin Assessment Scan

```
'************************************************************************
'MARGIN ASSESSMENT CONTROL CODE
'************************************************************************
'DESCRIPTION:
'ROTATES STM MOTOR, TRANSLATES URS LINEAR STAGE WHILE SYNCHING WITH A SENSOR
'************************************************************************
#START
'AXIS A=ROTATIONAL
'AXIS B=LINEAR
'AXIS C=FOCUS

'==================USER INPUT PARAMETERS HERE============
A=2.291;'ROTATIONAL SPACING (DEGREES)
B=1 ;'LINEAR SPACING (MM)
INTTM=1 ;'CAMERA INTEGRATION TIME(MSEC)
SP15000,9000,9000 ;'SPEEDS
'==================DO NOT CHANGE BELOW CODE==============
'SETUP PARAMETERS
CN-1 ;'CONFIGURING INPUTS
MT-2,-2,-2  ;'STEPPER MODE
YA256,16,16 ;'MICROSTEPS PER STEP
YB200,200,200 ;'STEPS PER ROTATION
```

```
YC0,0,0,0 ;'NEEDED ONLY IF ENCODER ADDED
YS0,0,0,0 ;'NEEDED ONLY IF ENCODER ADDED
KS5,1,1 ;'SMOOTHS THE STEP
AC2500000,200000,200000 ;'ACCELERATIONS
DC2500000,200000,200000 ;'DECELERATIONS
SHABC;'ENABLE MOTORS
TM1000

'=======================================
'A AXIS: 51200 COUNTS FULL ROTATION
'B, AXIS: 1600 COUNTS 1MM MOVEMENT

'===========CALCULATIONS===============
TOTA=360/A;'TOTAL MOVEMENTS AROUND
TOTB=50/B;'TOTAL LINEAR FOR 50MM SAMPLE LENGTH
STEPA=@INT[51200/TOTA] ;'COUNTS PER ROTATION MOVE
STEPB=@INT[1600*B] ;'COUNTS PER MOVEMENT LINEAR
STEPC=100 ;'SIMULATE FOCUS ADJUST

MG"TOTALA:",TOTA,", STEPA:",STEPA
MG"TOTALB:",TOTB,", STEPB:",STEPB

I=0 ;'COUNTER
DP 0,0,0 ;'SET START POSITION AS ZERO

#LOOP
  PA,(I*STEPB)
  REZERO=(I*51200) ;'CALC OFFSET TO GET BACK TO 0
  PAREZERO ;'REALIGNS ROTATIONAL AXIS TO 0
  BGAB  ;'BEGIN LIN AND RE-ZEROING MOVEMENTS
  MCAB ;'WAIT FOR MOTION COMPLETE
  J=0
  #ROTATE
    MG"J",J," ",(J*STEPA+(I*51200))
    PA(J*STEPA+(I*51200))
    J=J+1
    BGA ;'PERFORM ROTATION
    MCA ;'WAIT FOR ROTATION TO END
```

```
    SB1 ;'PULSE TO TAKE PICTURE (INPUT
    WTINTTM ;'INTEGRATION TIME
    CB1 ;'CLEAR CAMERA PULSE
  JP#ROTATE, J<=TOTA
  I=I+1
JP#LOOP, I<=TOTB
MG"MOVING BACK TO ZERO"
PA (I*51200),0,0
BGBC
MCBC ;'WAIT FOR RETURN TO ZERO
MO ;'DISABLE MOTORS
MG"DONE"
EN
```

References

[1] J. Alda and J. Arasa. Paraxial ray tracing. In *Encyclopedia of Optical Engineering*, pages 1920–1931. Marcel-Dekker, 2004. 12

[2] T.M. Allweis, Z. Kaufman, S. Lelcuk, I. Pappo, T. Karni, S. Schneebaum, R. Spector, A. Schindel, D. Hershko, M. Zilberman, J. Sayfan, A. Hadary Y. Berlin, O. Olsha, H. Paran, M. Gutman, and M. Carmon. A prospective, randomized, controlled, multicenter study of a real-time, intraoperative probe for positive margin detection in breast-conserving surgery. *The American Journal of Survery*, 196:483–489, 2008. 21, 64

[3] R. Aylward. Advanced galvanometer-based optical scanner design. *Sensor Review*, 23(3):216–222, 2003. 18, 33

[4] J.A. Bernstein, E.C. Hodgin, H.W. Holloway, C.S. Hedlund, E.S. Storey, and J.D. Hubert. Mohs micrographic surgery: a technique for total margin assessment in veterinary cutaneous oncologic surgery. *Veterinary and Comparative Oncology*, 4(3):151–160, 2006. 22

[5] B. Brooksby, H. Dehghani, K. Vishwanath, B.W. Pogue, and K.D. Paulsen. Internal refractive index changes affect light transport in tissue. In *Proceedings of SPIE, Optical Tomography and Spectroscopy of Tissue V*, volume 4955, pages 296–304, 29 July 2003.

[6] J.Q. Brown, T.M. Bydlon, L.M. Richards, B.Yu, S.A. Kennedy, J. Geradts, L.G. Wilke, M.K. Junker, J.Gallagher, W.T. Barry, and N. Ramanujam. Optical assesssment of tumor resection margins in the breast. *IEEE Journal of Selected Topics in Quantum Electronics*, 16(3):530–544, 2010. 21, 22, 64

[7] T.M. Bydlon, S.A. Kennedy, L.M. Richards, J.Q. Brown, B. Yu, M.K. Junker, J. Gallagher, J. Geradts, L.G. Wilke, and N. Ramanujam. Performance metrics of an optical

spectral imaging system for intra-operative assessment of breast tumor margins. *OSA: Optics Express*, 18(8):8058–8076, 2010. 22, 72

[8] Cambridge Technology Inc. *Technical Report: Choosing the Right Galvanometer and Servo for the Job*. Cambridge Technology Inc., 2007. 15

[9] A.T. Cenko. *Automatic Interferometric Alignment of a Free-Space Optical Coherence Tomography System*. PhD thesis, University of Waterloo, 2007. 20, 66

[10] S. Chang, Y. Mao, C. Flueraru, and S. Sherif. Optical coherence tomography: Technology and applications. In *Proceedings of SPIE, Conference on Optical Instruments and Technology: Optical Systems and Optoelectronic Instruments*, volume 7156, Ottawa, ON, Canada, 16-19 Nov 2008. 3

[11] G.L. Cote, L.V. Wang, and S.R. Rastegar. Biomedical optics and lasers. In *Introduction to Biomedical Engineering*, page 990. Elsevier Academic Press, Massachusetts, USA, 2005. 7

[12] R.C Dorf and R.H. Bishop. *Modern Control Systems*. Prentice Hall, 11th edition, 2008. 16, 17

[13] W. Drexler and J. Fujimoto. Introduction to optical coherence tomography. In *Optical Coherence Tomography: Technology and Applications*, pages 1–45. Springer, New York, USA, 2008. 3, 7, 20

[14] Galil Motion Control. Application note 5475. Galil Application Notes, available www.galilmc.com/support/appnotes/miscellaneous/note5475.pdf, 2009. 30

[15] J.M. Geary. *Introduction to Lens Design*. William Bell Publishers, Virginia, USA, 2002. 75

[16] A.S. Haka, Z. Volynskaya, J.A. Gardecki, J. Nazemi, J. Lyons, D. Hicks, M. Fitzmaurice, R.R. Dasari, J.P. Crowe, and M.S. Feld. Orientation of satellite and airborne imagery from multi-line pushbroom sensors with a rigorous sensor model. *Cancer Research*, 66:3317–3322, 2006. 3, 22

[17] T.M. Haylock, A.T. Cenko, J.T. Meade, F. Kazemzadeh, and A.R. Hajian. Unification of satellite and medical scan methods. In *Proceedings of the IEEE: International Symposium on Optomechatronic Technologies (ISOT)*, pages 1–5, Toronto, Canada, 25-27 Oct 2010. IEEE. 18, 22

[18] D. Huang, E.A. Swanson, J.S. Schuman C.P. Lin, W.G. Stinson, W. Chang, M.R. Hee, T. Flotte, K. Gregory, C.A. Puliafito, and J.G. Fujimoto. Optical coherence tomography. *Science*, 254:1178–1181, 1991. 3

[19] A. Laupacis and W. Evans. Diagnostic imaging in canada. *Healthcare Papers*, 6(1):8–15, 2005. 3

[20] F. Li, J. Barabas, A. Mohan, and R. Raskar. Analysis on errors due to photon noise and quantization process with multiple images. In *44th Annual Conference on Information Sciences and Systems (CISS)*, pages 1–6, Princeton, USA, 17-19 March 2010. 8, 35

[21] Logicon Geodynamics Inc. *Multispectral Imagery Reference Guide*. Logicon Geodynamics Inc, Virginia, USA, 1997. 24

[22] J.F. Mackay. Understanding noise at the nanometer scale. *Laser Focus World*, March, 2007. 51

[23] V.N. Mahajan. *Optical Imaging and Aberrations, Part 1 - Ray Geometrical Optics*. SPIE Publications, USA, 1998. 12

[24] Melles Griot. *All Thing Photonic - The CVI Melles Griot Technical Guide*, volume 2. CVI Melles Griot, 2009. 6, 10, 14, 15, 16, 32

[25] Newport Corporation. *Linear Translation Stage Selection Guide*. Newport Corporation, Irvine, California, USA, 2011. 16

[26] F.T. Nguyen, A.M. Zysk, E.J. Chaney, J.G. Kotynek, U.J. Oliphant, K.M. Rowland F.J. Bellafiore, P.A. Johnson, and S.A. Boppart. Intraoperative evaluation of breast tumor margins with optical coherence tomography. *Cancer Research*, 69(22):8790–8796, 2009. 21, 22, 64

[27] W. O'Brien. Long-range motion with nanometer precision. *Photonics Spectra*, June, 2005. 16

[28] T. P. Olson, J. Harter, A. Munoz, D.M. Mahvi, and T.M. Breslin. Frozen section analysis for intraoperative margin assessment during breast-conserving surgery results in low rates of re-excision and local recurrence. *Annals of Surgical Oncology*, 14(10):2953–2960, 2007. 22

[29] I. Pappo, R. Spector, A. Schindel, S. Morgenstern, J. Sandbank, L.T. Leider, S. Schneebaum, S. Lelcuk, and T. Karni. Diagnostic performance of a novel device for real-time margin assessment in lumpectomy specimens. *Journal of Surgical Research*, 160:277–281, 2010. 3, 72, 82

[30] A.G. Podoleanu, G.M. Dobre, R.G. Cucu, R. Rosen, P. Garcia, J. Nieto, D. Will, R. Gentile, T. Muldoon, J. Walsh, L.A. Yannuzzi, Y. Fisher, D. Orlock, R. Weitz, J.A. Rogers, S. Dunne, and A. Boxer. Combined multiplanar optical coherence tomography and confocal scanning ophthalmoscopy. *Journal of Biomedical Optics*, 9(1):86–93, 2004. 24

[31] D. Poli. Orientation of satellite and airborne imagery from multi-line pushbroom sensors with a rigorous sensor model. *International Archives of Photogrammetry Remote Sensing and Spatial Information Sciences*, 35(1):130–135, 2004. 24

[32] F.F. Sabins. *Remote Sensing: Principles and Interpretations*. W. H. Freeman, USA, 3rd edition, 1996. 19, 23

[33] A. Samberg. What laser scanning can do today: Current techniques. In *3rd EARSeL Workshop on Lidar Remote Sensing of Land and Sea*, Tallinn, Estonia, 17-19 July 1997. 24

[34] J. Schott. *Remote Sensing, The Image Chain Approach*. Oxford Publishing, New York, USA, 2nd edition, 2007. 19, 23, 24

[35] S. Smith. *The Scientist and Engineer's Guide to Digital Signal Processing*. California Technical Publishing, 1st edition, 1997. 10, 36

[36] B.A. Standish, K.C.L. Kenneth, A. Mariampillai, N. Munce, M.K.K. Leung, V.X.D. Yang, and A. Vitkin. In vivo endoscopic multi-beam optical coherence tomography physics in medicine and biology. *Physics in Medicine and Biology*, 55:615–622, 2009. 25

[37] K. Strohbehn, T. Chooa, J. Hayesa, G. Heylera, J. Leesa, and D. Lohra. Crism scan system, 2010.

[38] N. Suehira, H. Yoshida, T. Yuasa, M. Sato, and K. Yamada. In-vivo retinal imaging by multi-beam spectral-domain optical coherence tomography with a novel spectrometer. In J.G. Fujimoto, editor, *Proc. of SPIE 7889 - Optical Coherence Tomography and Coherence Domain Optical Methods in Biomedicine XV*, 2011. 25

[39] J. Tal. Stepper motor control. Galil Tutorials, available http://www.galilmc.com/learning/tutorial-display.php?tutorial=stepper-motor-control, 2001. 14

[40] ThorLabs. Single and dual axis scanning galvanometer system. Model Number GVS001, 2009. 28, 29

[41] L. Thrane, T.Y. Harold, and P.E. Andersen. Calculation of the maximum obtainable probing depth of optical coherence tomography in tissue. In *Coherence Domain Optical Methods in Biomedical Science and Clinical Applications*, volume 3915, pages 2–11, Bellingham, WA, USA, 2000. Society of Photo-Optical Instrumentation Engineers. 7

[42] J. Zara, J. Izatt, K. Rao, S. Yazdanfar, and S. Smith. Scanning mirror for optical coherence tomography using an electrostatic mems actuator. In *IEEE International Symposium on Biomedical Imaging*, volume 7441 of *Proc. of IEEE International Symposium on Biomedical Imaging*, pages 297–300, Washington, DC, USA, 2002. IEEE. 19, 25

[43] T. Zhao and R.F. Murphy. Automated intepretation of subcellular location patterns from three dimensional confocal microscopy. In *Handbook of biological confocal microscopy*, page 822. Springer, New York, USA., 3rd edition, 2006. 36